LANTHANIDE NANOCRYSTALS: A PLATFORM FOR THE STUDY OF OPTICS AND MAGNETISM IN NANOMATERIALS

By

Suseela Somarajan

Dissertation

Submitted to the Faculty of the

Graduate School of Vanderbilt University

in partial fulfillment of the requirements

for the degree of

DOCTOR OF PHILOSOPHY

in

Physics

December 2010

Nashville, Tennessee

Approved:

Professor James H. Dickerson

Professor Eva M Harth

Professor Bridget R Rogers

Professor Norman H Tolk

Professor Kalman Varga

Dedicated

to

My parents, Mr. M. Somarajan and Mrs. G. Udayamma,

and to my family members

who has been a source of encouragement and inspiration to me throughout my life.

ACKNOWLEDGEMENT

First, I express my utmost gratitude towards Prof. James H. Dickerson, my advisor and the Chair of my Ph.D. committee, for providing me the opportunity to work in the area of nanoscience. His sage advice, insightful criticisms, and patient encouragement inspire and enrich my growth as a student, a researcher and a scientist.

I also would thank to other members of my Ph.D. committee: Professor Eva M Harth, Professor Bridget R Rogers, Professor Norman H Tolk and Professor Kalman Varga for their guidance and advice during the development of this dissertation.

I would like to thank Dr. Dmitry S. Koktysh for getting me inputs on nanocrystal synthesis work in the VINSE laboratory. Thanks to my friend Melissa Harrison for unfailing support during my research. Special thanks go to my collegues: Dr.Sameer Mahajan, Dr.Saad Hasan, Weidong He and Alex Krejci who were closely associated to my research work.

Thanks to Dr.Tony Hmelo for the technical traning on various equipments in VINSE, Dr. Dennis Brown and Dr. Charles Johnson for their assistance on Mössbauer experiments, Dr. Ju-Hyun Park, Dr. Stephen A.McGill, and Ryan L.Stillwell for their assistance in conducting experiments at NHMFL.

I thank my friends and collaborators: John Rigueur, Dr.Marcela Redigolo, Dr. Dustin Kavich, Dr.Chinessa T.Adkins, Jed Zigler, Joyeeta Nag, Robert Harl, Dr.Ben Schmidt, Dr.Maria Gonzalo de Juan, Howard Titzel, Maria Verde Lozano, Benjamin Spears, and Arithra Das Gupta for their encouragement and support.

Special mention to Mr. Donald Pickert, Administrative Assistant, Physics & Astronomy for timely help on administrative and academic matters.

I would like to thank U.S. Department of Energy, Basic Sciences, Division of Materials Science and Engineering, Award DE-FG02-07ER46447; the National Science Foundation (NSF), Award DMR-0757380; Vanderbilt Institute for Nanoscale Science and Engineering (VINSE); the National High Magnetic Field Laboratory, the State of Florida and the Center for Nanophase Materials Sciences, which is sponsored at Oak Ridge National Laboratory by the Division of Scientific User Facilities, U.S. Department of Energy.

I am grateful to my family members: My mother, G Udayamma, though no longer with me is the most significant source of encouragement and support, my Dad M.Somarajan, Uncle Adv. Vijay Sekhar and my in-laws for their never ending encouragement.

Words fail to express my appreciation to my husband Ashokan Vattakkattil, my daughters Akhila Ashokan and Anagha Ashokan whose dedication, love, and persistent confidence in me, has eased the load on my shoulder. I owe them for unselfishly supporting me in balancing family and my research work.

TABLE OF CONTENTS

LIST OF FIGURES

LIST OF TABLES

CHAPTER 1

INTRODUCTION

1.1 Overview

Europium chalcogenides (EuX: X = O, S, Se, Te) are one of the most prominent classes of magnetic lanthanide compounds. These materials are called f-block compounds because of the dominant 4f electron orbital in the rare earth ion. For a number of years, EuX have been studied for their optical properties, their attractive magneto-optical response, and their robust ferromagnetic and antiferromagnetic properties.[1-7] Study of these materials was motivated due to their wide range of potential applications as ferromagnetic semiconductors, magnetoresistance, optomagnetic and luminescent materials.[8, 9] EuX display a very rich spectrum of magnetic properties, associated with the uncompensated spin moments of Eu atoms.[10, 11] The magnetic moment is caused by the half-filled 4f shell of the Eu^{2+} ions with a magnetic ground state $^8S_{7/2}$ (L=0, S=7/2 and J=7/2). The Eu^{2+} ions carry well-localized spin only magnetic moments of 7 Bohr magnetons (7μB), which order in antiferromagnetic (EuTe, EuSe), ferrimagnetic (EuSe) or ferromagnetic (EuS,EuO) structures (see section1.4). Since these materials exhibit pure spin magnetism due to strongly localized electrons, and almost negligible anisotropy, EuX are considered to be models for Heisenberg magnets.[12]

Of all the europium chalcogenides, europium sulfide has been investigated most thoroughly due to its intriguing ferromagnetic, optical and magneto-optical properties.[13]

EuS is a narrow band gap ferromagnetic semiconductor (E_g=1.65 eV) with a Curie temperature (T_c) of 16.6 K. The 4f levels in EuS are situated between the p-valence band of the S^{2-} and the 5d conduction band of Eu^{2+}. The 4f-5d electronic transition and spin configuration of EuS lead to large Faraday rotation and Kerr effect, which make EuS as a promising candidate for an active material in magneto-optical devices.[14]

It is known that a decrease of the crystal size can affect the physical properties of a magnetic semiconducting material.[8] The change in the properties of nanocrystals is mainly driven by two factors: one is the increase in the surface to volume ratio; the other is the change in electronic structure of the material due to quantum confinement effects. In the mid 1990s, researchers began investigating nanocrystalline forms of EuS, motivated by the possibility of their use in nanotechnology employing their enhanced magnetic, optical and magneto-optical properties.[15-17] Such novel properties provide a wide range of potential applications for these materials as bioimaging reagents, magneto-optic and luminescent materials.[8, 13, 18, 19] Exploring EuS nanomaterials, whose bulk form can be described by a classic Heisenberg ferromagnetic model, can also allow us to understand the influence of particle size on the magnetic exchange mechanisms and magneto-optical coupling mechanisms.[20] Several groups have studied EuS nanoparticles in a variety of nanoscale size regimes and embedded in various media.[9, 21, 22] Enhancements in the physical properties of EuS nanomaterials have been observed as a function of the size of the nanocrystals.[8, 9, 13, 14, 21-25] For an insight into this field, a few relevant findings are outlined here in chronological order.

Chen W. et al. [22] (2000): Luminescence enhancement of EuS nanoclusters in zeolite

- Compared to bulk EuS powder, large luminescence enhancement was observed in EuS clusters formed in ultrastable zeolite-Y.
- Emission of EuS clusters shifts to higher energies relative to that of bulk EuS powder.

Thongchant S.et al. [18] (2003): Liquid-phase synthesis of EuS nanocrystals and their physical properties.

- First report on the colloidal synthesis of EuS nanocrystals.

Thongchant S.et al. [24] (2003): First observation of Faraday effect of EuS nanocrystals in polymer thin films.

- Semi-transparent EuS nanocrystal - embedded plastic films showed large Faraday effect at room temperatures.
- Faraday rotation peaks of the films shifted towards longer wavelength with an increase of the crystal size of EuS.

Redigolo M. L. et al. [13] (2006) : Magnetization reversal in europium sulfide nanocrystals

- Observation of reversal in the magnetization hysteresis curve of europium sulfide nanocrystals.

Zhao F.et al. [9] (2006): Synthesis and size-dependent magnetic properties of monodisperse EuS nanocrystals.

- A blue shift of the maximum absorption peak position of the UV/Vis spectra with decreasing particle size of EuS.

- The Curie temperature T_c and coercivity H_c were observed to be strongly dependent on the size of EuS nanocrystals.

Regulacio M. D. et al. [23] (2008): Size-dependent magnetism of EuS nanoparticles.

- A decrease in ferromagnetic ordering temperature occurs with decreasing particle size (7.2 nm-4.9 nm)

Redigolo M. L. et al. [25] (2009): Europium sulfide nanoparticles in the sub-2 nm size regime.

- First report on the synthesis of sub-2 nm size EuS crystals.

The majority of work has been focused on developing EuS nanocrystals using different synthesis techniques and studying their physical properties. A blue shift in the optical absorption spectrum enhanced Verdet constant and decreased ferromagnetic ordering temperatures have been observed with decreasing particle size.[8, 9, 23, 24] However, literature on the preparation of single domain EuS nanocrystals and a systematic study on magnetism in EuS nanocrystals, so far are limited.

Further investigation into the size-dependent effects observed in EuS nanocrystals will be helpful to describe the magnetizing mechanisms and to facilitate the design of novel magnetic materials. In order to study systematically the size dependent effects, we must synthesize size controlled, surface protected EuS nanocrystals. Hence, a new synthesis technique was required by our research group to produce stable, highly crystalline, monodisperse EuS nanocrystals. The technique must have the versatility to produce a wide range of particle sizes so that we can study size dependent physical

properties including: ferromagnetic ordering temperature, saturation magnetization, superparamagnetic relaxation phenomena, and quantum confinement effect on the absorption and luminescence spectrum. Thus, the first part of the dissertation research (chapter II, III and IV) explores the development of nanocrystals, and optical and size-dependent magnetic properties of EuS nanocrystals.

Potential room-temperature, device applications of EuS nanocrystals are limited due to the relatively low ordering temperatures and the poor semiconducting transport properties. One of the approaches to achieve a ferromagnetic semiconductor, with improved physical properties compared to EuS, is to introduce magnetic ions into a non-magnetic semiconducting matrix, replacing the extant cation in the lattice.[26] This substitution gives rise to localized magnetic moments in the semiconducting material. These materials are called dilute magnetic semiconductors (DMS). A significant amount of research has focused on finding DMS that are ferromagnetic at room temperature with the goal of realizing spintronics devices (see section 1.3).[27]

Lead-based DMS materials alloyed with europium have been investigated for a variety of optical, magnetic, and electronic applications.[28, 29] For example, increased europium content in lead based DMS alloys changes the energy band gap of the material and produces variations in the lattice constant and refractive index of the material. Such characteristics make these materials suitable for use in thin film Bragg mirrors, lasers, wavelength converters, and photodiodes for the IR range.[30-33] Magnetic properties of lead-based DMS materials containing europium ions have been investigated over the past two decades (see section 5.1).[34, 35] Among the lead–based DMS materials, lead europium

sulfide ($Pb_{1-x}Eu_xS$) has been shown to form a completely miscible alloy system.[36] Lead sulfide (PbS) and europium sulfide (EuS) both crystallize in the rock-salt crystal structure with only a 0.5% lattice mismatch between the two materials. Further, $Pb_{1-x}Eu_xS$ has exhibited energy band gaps tunable over a wide range. Important scientific accomplishments in bulk $Pb_{1-x}Eu_xS$ are outlined here.

Ishida A. et al. [36] (1988): $Pb_{1-x}Eu_xS$ films prepared by hot wall epitaxy.

- $Pb_{1-x}Eu_xS$ films were prepared for the first time using hot wall epitaxy technique.
- Lattice constants of the films were very close to that of PbS as expected from the small lattice mismatch between PbS and EuS.
- Energy gap increases very rapidly with EuS content up to x=0.05.

Bindilatti V. et al. [35] (1998): Magnetization steps in $Pb_{1-x}Eu_xS$: Exchange and anisotropic interactions.

- Magnetization measurements were performed on Bridgman grown $Pb_{1-x}Eu_xS$ single crystals ($x < 0.06$) at mK temperatures and found a value of $\frac{J}{k_B} = -0.228 \pm 0.007$ K for the dominant antiferromagnetic exchange constant.

Researchers focused their attention primarily on developing bulk $Pb_{1-x}Eu_xS$ films and studying their optical and magnetic properties. Synthesizing $Pb_{1-x}Eu_xS$ materials in nanocrystalline forms will likely exhibit improved magnetic and optical responses. We expect to observe quantum confinement effects on physical properties of $Pb_{1-x}Eu_xS$ materials as researchers have seen previously in other alloyed semiconducting,

nanocrystalline materials.[37-39] To the best of our knowledge, there are no other reports on nanoscale lead europium chalcogenide DMS systems. Chapter V explores the development, structural and magnetic studies of nanocrystalline lead europium sulfide, a dilute magnetic semiconductor.

Chapter I introduces europium chalcogenides - a classical Heisenberg magnet, its technological importance and its potential device applications. An overview of the past research on nanocrystalline EuS and bulk lead europium chalcognides ($Pb_{1-x}Eu_xS$) is presented. Review of magnetic interactions in solids, and a general discussion of magnetic and dilute magnetic semiconductors are included. Electronic structure of EuX, in particular EuS is reviewed. To understand the origin of magnetism in europium chalcogenides, different exchange mechanisms are discussed.

Chapter II describes the solid state thermolysis technique that was used to synthesize EuS nanocrystals of different sizes. The results of structural, optical and magnetic characterization of EuS nanocrystals are presented. Results of the Mössbauer absorption spectra of EuS nanocrystals at different temperatures are discussed.

Chapter III discusses about the development of a one-step solvothermal technique to produce colloidally stable, monodisperse EuS nanocrystals. Results of structural characterization of these nanocrystals are described. Effect of synthetic parameters on the size of nanocrystals is also explored.

Chapter IV investigates the role of particle size on the optical and magnetic properties of EuS nanocrystals. The absorption and temperature dependent photoluminescence characteristics of these nanocrystals are described. The effect of

particle size on the ferromagnetic ordering temperature in EuS nanocrystals is discussed. In addition, we review the effect of surface oxidation on the optical and magnetic characteristics of smaller EuS nanocrystals.

Chapter V presents the first report on the development of nanocrystalline alloyed lead europium sulfide, a dilute magnetic semiconductor. It includes the result of structural and magnetic characterization of EuS, PbS and Pb_xEu_yS nanocrystals. Exchange mechanisms in bulk dilute magnetic semiconductors are reviewed. Concentration dependence of the exchange interaction in Pb_xEu_yS nanocrystals is also discussed.

Chapter VI summarizes the research findings discussed in this dissertation.

1.2 Magnetic behavior of solids (General theory)

1.2.1 Origin of magnetism

The magnetic behaviour of atoms, molecules, ions and solids is related to the magnetic moments associated with individual electrons. The magnetic moments of each electron in an atom consists of two contributions. First is the orbital angular momenta of the electrons circulating the nucleus. In addition, each electron has an extra contribution to its magnetic moment arising from its spin. The magnetic moment associated with the orbital motion of electrons around the nucleus,which is directed along its axis of rotation is schematically illustrated in figure 1.1(a).

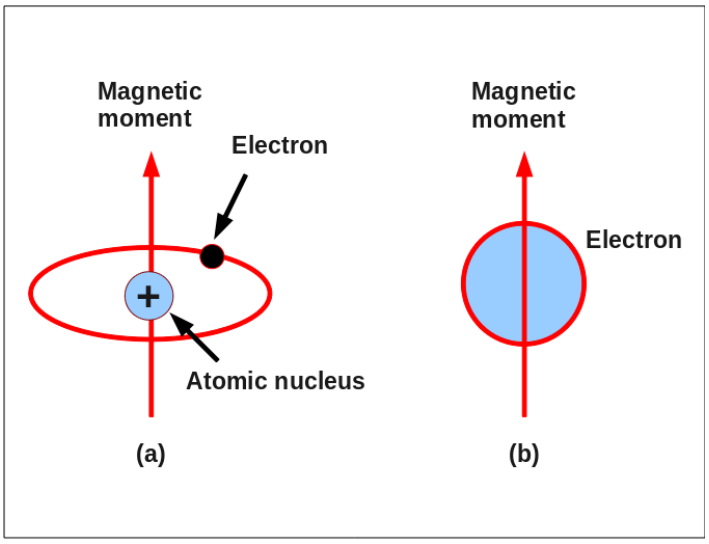

Figure 1.1: Schematic illustration of the magnetic moment associated with (a) an orbiting electron (b) a spinning electron.[40]

The electron behaves as if it were spinning about its own axis, and the magnetic moment originates from this electron spin, which is directed along the spin axis as shown in figure 1.1(b). Thus, each electron in an atom can be considered as a small magnet having permanent orbital and spin magnetic moments. The most fundamental magnetic moment is the Bohr magneton which is defined as $\mu_B = \frac{e\hbar}{2m}$ (e-electron charge, $\hbar$-reduced Planck constant, m- electron rest mass).[41]

The spin magnetic moment of an electron is given by,

$$\mu_s = -g_s \mu_B \frac{\vec{S}}{\hbar} \tag{1.1}$$

The orbital magnetic moment of an electron is given by,

$$\mu_l = -g_l \mu_B \frac{\vec{L}}{\hbar} \tag{1.2}$$

The total magnetic dipole moment resulting from both spin and orbital angular momenta of an electron is related to the total angular momentum $\vec{J} = \vec{L} + \vec{S}$ by:

$$\mu_j = -g_j \mu_B \frac{\vec{J}}{\hbar} \tag{1.3}$$

where g_s, g_l and g_j represents the spin g-factor, electron orbital g-factor, and Lande g-factor.

Magnetization and Field: When a material medium is subjected to an applied field ($\vec{H}$), the medium is magnetized and this magnetization is described by the magnetization vector $\vec{M}$, the dipole moment per unit volume. The magnetic induction or magnetic flux density $\vec{B}$ inside the material medium is given by

$$\vec{B} = \mu_0 (\vec{H} + \vec{M}) \tag{1.4}$$

μ_0 is the permeability of free space.

One of the most important properties of magnetic materials is its susceptibility (χ), which is defined as the magnetic moment induced by a magnetic field per unit volume.

The magnetic susceptibility χ is given by,[42]

$$\chi = \frac{\vec{M}}{\vec{H}} \tag{1.5}$$

1.2.2 Classification of magnetic materials

Diamagnetic substances are composed of atoms or molecules that possess completely closed atomic shells, meaning that all their electrons are paired, and have no net magnetic moments. With the application of an external field, a net dipole moment, opposing the field, is induced in the atoms or molecules in accordance with Lenz's law (figure 1.2). According to Langevin theory[42], the induced moment is given by,

$$\mu = -\frac{e^2 BZ}{6m}\left\langle r^2 \right\rangle \tag{1.6}$$

The diamagnetic susceptibility per unit volume is described by,

$$\chi = -\frac{NZe^2}{6m}\left\langle r^2 \right\rangle \tag{1.7}$$

where e is the charge of electron, B is the magnetic field intensity, Z is the atomic number , m is the mass of electron , N is the number of atoms per unit volume , and $\left\langle r^2 \right\rangle$ is the mean square distance of the electron from the nucleus. Since the induced magnetic moment always opposes the applied field, the diamagnetic susceptibility is negative. One of the characteristic behavior of diamagnetic materials is that the susceptibility is temperature independent (figure 1.3a).

All materials exhibit some degree of diamagnetism, a weak negative magnetic susceptibility. In some substances, however, other magnetic properties such as paramagnetism or ferromagnetism may mask its diamagnetic properties.

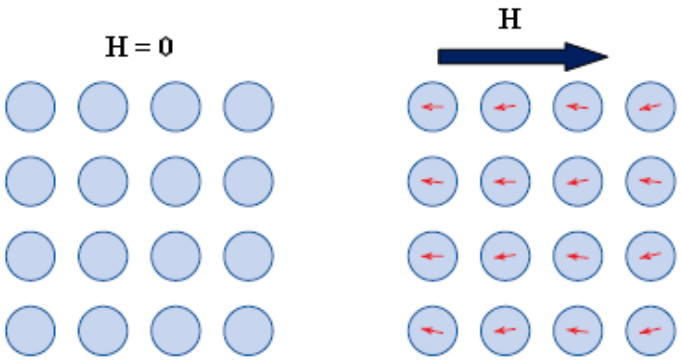

Figure 1.2 : Schematic representation of the atomic dipole configuration with and without the field for a diamagnetic material.[40]

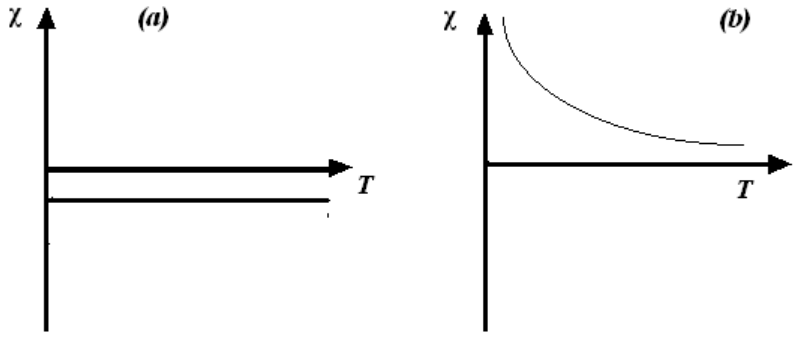

Figure 1.3: Schematic demonstration of the susceptibility versus temperature (χ-T) plot of (a) diamagnetic and (b) paramagnetic material.[43, 44]

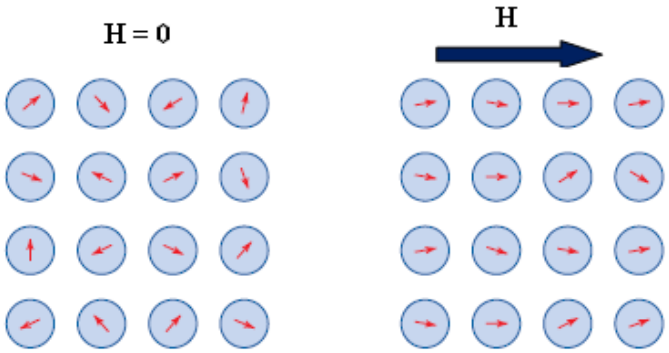

Figure 1.4: Atomic dipole configuration of a paramagnetic material with and without the field.[40]

Paramagntism generally occurs in atoms or molecules that do have a non-zero magnetic moment because of the unpaired electrons. In the absence of applied field, these atomic moments point at random because the magnetic moments on neighbouring atoms interact only very weakly with each other and can be assumed to be independent. When a field is applied,the magnetic moments have a tendancy to turn towards the direction of field. If no opposing force acts,complete alignment of the atomic moments will be produced,resulting in a very large magnetization in the direction of field. However, an increase in temperature will randomize the alignment of atomic moments. The result is only partial alignment of atomic moments in the field direction (figure 1.4). This produces a weak magnetization and a small suceptibility. In many paramagnets, the magnetic susceptibility is inversely proportional to the temperature (figure 1.3b) . This dependence is known as Curie's law [41]

$$\chi = \frac{C}{T} \qquad (1.8)$$

where T is the temperature in Kelvin, and C is the Curie constant.

According to The Langevin theory of paramagnetism [45], paramagnetic susceptibility

$$\chi = \frac{N\mu^2}{3k_B T} \tag{1.9}$$

where N is the number of magnetic moments (μ) per unit volume, k_B is the Boltzmann's constant. Langevin theory, which leads to Curie law, is based on the assumption that the individual carriers of magnetic moments do not interact with one another, but are acted on only by the applied field and thermal agitation.[41] It was found that the susceptibilities of a number of paramagnetic materials do not obey Curie law; instead the materials obey a modified law known as Curie-Weiss law. The law is based on the assumption individual magnetic moments interact with one another .[41]

According to Curie-Weiss law,

$$\chi = \frac{C}{T - \theta} \tag{1.10}$$

where θ is called Curie-Weiss constant, which is a measure of the strength of the interaction between the magnetic moments. For substances that obey Curie's law, $\theta = 0$. Materials that undergo a paramagnetic to ferromagnetic transition, $\theta > 0$ and for materials that undergo a paramagnetic to antiferromagnetic transition $\theta < 0$.

According to the quantum theory of paramagnetism [45], an atom with multiple electrons, has $2J+1$ energy levels. The expression for magnetization is

$$M = NgJ\mu_B B_J\left(\frac{gJ\mu_B H}{k_B T}\right) \tag{1.11}$$

$B_J(x)$ is the Brillouin function, which is defined as

$$B_J(x) = \left(\frac{(2J+1)}{2J}\right)\coth\left(\frac{(2J+1)x}{2J}\right) - \left(\frac{1}{2J}\right)\coth\left(\frac{x}{2J}\right) \tag{1.12}$$

where N is the number of magnetic moments per unit volume, g is the g factor or the spectroscopic splitting factor, J is the total angular momentum quantum number ($J = L + S$), where L and S are the orbital and spin quantum numbers of the dipole, μ_B is the Bohr magneton and H is the applied magnetic field.

For strong fields and low temperatures ($x >> 1$), the function $B_J(x) \approx 1$ for all J, which corresponds to a state of magnetic saturation.

$$M = NgJ\mu_B \tag{1.13}$$

For high temperatures and weak fields ($x << 1$),

$$M = \frac{Ng^2\mu_B{}^2 J(J+1)H}{3k_B T} \tag{1.14}$$

$$\chi = \frac{M}{H} = \frac{Ng^2\mu_B{}^2 J(J+1)}{3k_B T} = \frac{C}{T} \tag{1.15}$$

which again is the Curie law with

$$C = \frac{Ng^2 \mu_B{}^2 J(J+1)}{3k_B}. \tag{1.16}$$

The electron spins interact with one another through an energetically favorable exchange mechanism. Ferromagnetism and antiferromagnetism are the two common forms of magnetic ordering that result through these exchange interactions. The mechanism of exchange interaction between two localized spins was first investigated by Heisenberg and led to the famous Heisenberg -type interaction given by [46],

$$H_{exchange} = -\sum_{i,j} J_{ij} \vec{S}_i \cdot \vec{S}_j \tag{1.17}$$

J_{ij} is the exchange constant between the i^{th} and j^{th} ion site, S_i is the spin of the i^{th} ion and S_j is the spin of the j^{th} ion. A positive exchange constant corresponds to parallel (ferromagnetic) alignment of the magnetic moments and a negative exchange constant corresponds to antiparallel (antiferromagnetic) alignment. Exchange mechanisms can be divided into two categories: direct exchange and indirect exchange. A direct exchange interaction occurs between magnetic moments that are close enough to have sufficient overlap of their wave functions. An indirect exchange interaction acts through the conduction electrons, or itinerant electrons, causes both ferro- and antiferromagnetic alignment. The main indirect exchange mechanisms include Ruderman, Kittel, Kasuya and Yoshida (RKKY) interactions, super exchange and double exchange. RKKY interaction is the most dominant of the exchange interactions in rare earth metals and

alloys.[46] The exchange mechanisms in rare earth will be decribed in more detail later (see section 1.4.2).

Ferromagnetic materials have unpaired electrons and have a net magnetic moment. The coupling interaction causes net spin magnetic moments of adjacent atoms to align with one another, even in the absence of an external field (figure 1.5a). The mutual spin alignment exists over a relatively large region of the crystal called domains. Even though the coupling interactions in ferromagnetic material are large, the atomic thermal motions eventually overcome the coupling interaction between the adjacent atomic dipole moments, producing a randomizing effect. This occurs at a particular temperature called the Curie temperature (T_c). Below the Curie temperature,the ferromagnet is in the ordered state and above T_c the ferromagnet is in the disordered state. Above T_c, the material becomes paramagnetic with the susceptibility obeying Curie-Weiss law. The temperature dependence of susceptibility of a ferromagnetic material is shown in figure 1.5b. A sketch of the magnetization versus magnetic field strength (M-H) graph of a dia, para and ferromagnetic material is shown in figure 1.5c.

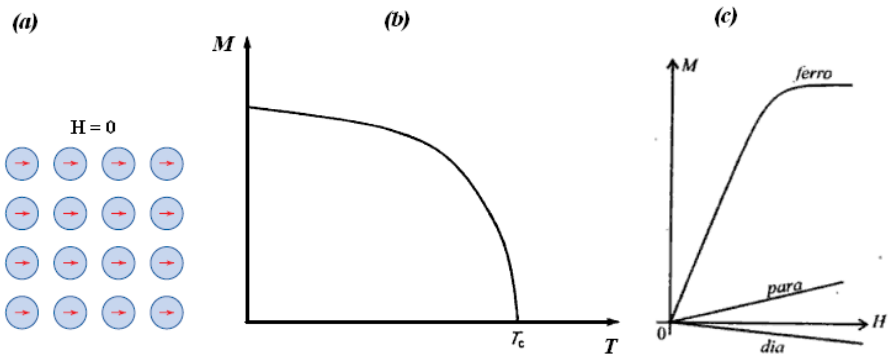

Figure 1.5: Schematics of the (a) mutual alignment of atomic dipoles of a ferromagnetic material, which will exist even in the absence of an external magneticfield, (b) magnetization versus temperature (M-T) graph of a ferromagnetic material, and (c) magnetization versus magnetic field strength (M-H) graph of a diamagnetic, paramagnetic, and ferromagnetic material.[40, 47]

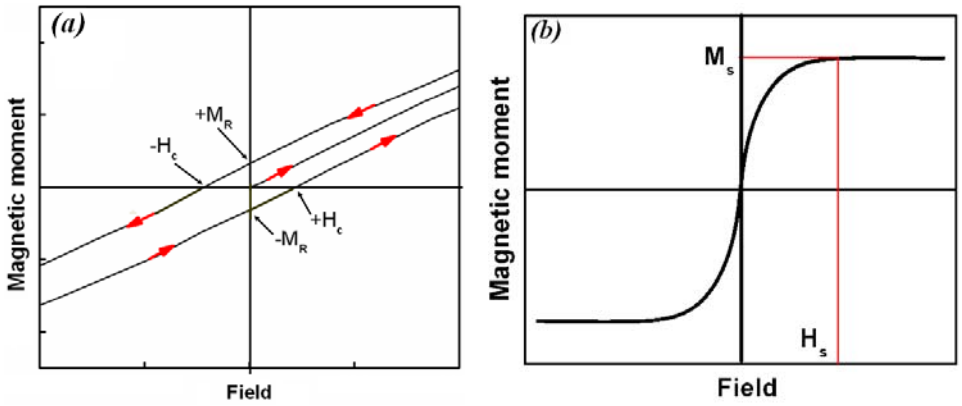

Figure 1.6: (a) Magnetization versus magnetic field strength (M-H) graph for a ferromagnetic material that is subjected to forward and reverse saturations. (b) M-H curve showing saturation magnetization and saturation field.

When a ferromagnetic material is magnetized by an increasing applied field and then the field is decreased, the magnetization does not follow the initial magnetization

curve obtained during the increase. This irreversibility is called hysteresis. A typical hysteresis arises from measuring the magnetization of the material as a function of magnetic field applied in positive and negative directions is shown in figure 1.6.a. The response of the material follows two distinct paths on magnetization and demagnetization. At large fields, the magnetization approaches the maximum value called saturation magnetization (M_s) which is schematically shown in 1.6.b. Magnetic material in a ferromagnetic state have a residual magnetization at zero external fields called remanent magnetization (M_r). Coercivity (H_c) characterizes the reverse –field strength needed to reduce magnetization to zero.

In an antiferromagnetic material, the negative exchange interaction causes the molecular or exchange field to orient in a way that it is favorable for nearest neighbor magnetic moments to lie antiparallel to one another.[43] The ordered moments lie on two interpenetrating sub-lattices within each of which the moments are all parallel. The spins on one sub-lattice being antiparallel to those on the other sub-lattice.[48] The antiparallel alignment occurs below a transition temperature called Neel temperature,T_N. Above T_N the thermal energy dominates the exchange energy, resulting in a paramagnetic state with the susceptibility obeying Curie-Weiss law.[41] As the temperature decreases below T_N, the tendency for antiparallel alignment becomes stronger. Hence an antiferromagnetic material has no net spontaneous moment and can acquire a moment only when a strong field is applied.

Ferrimagnetism is a particular case of antiferromagnetism in which the magnetic moments on the two sub-lattices are pointing in opposite direction, but have different

magnitudes. As a result, below the ordering temperature a spontaneous magnetization appears in this material. The magnetic properties of ferromagnets and ferrimagnets are generally similar. They both exhibit hysteresis, saturation and their magnetization is much greater than other classes of magnetic materials.[42]

1.2.3 Superparamagnetism

If ferromagnetic particles are small enough, the energy necessary to form multiple domains within single nanoparticles is higher than the energy needed to remain as a single magnetic domain. This is because when the particle size decreases, surface energies such as the domain wall energies, become more in comparison with volume energies, such as demagnetizing energy. Thus, a critical dimension exists below which it is energetically favorable for domain walls to disappear so that the particle become single-domain. For spherical nanoparticles, the critical radius is given by,

$$r \approx \frac{36\sqrt{AK}}{M_s^{\,2}} \tag{1.18}$$

where A is the exchange stiffness constant, K is the anisotropy constant and M_s is the saturation magnetization. The magnetization process of a single-domain particle involves the rotation of magnetic moment. The first assumption of superparamagnetic theory is to consider that all the magnetic moments within the particle rotate coherently, i.e. the net magnetic moment can be represented by a single classical vector, with magnitude $\mu = \mu_{atm} N$,where μ_{atm} represents the atomic magnetic moment and N is the number of magnetic atoms that compose each particle.[49] Spherical nanoparticles are generally

considered as having uniaxial anisotropy, which is characterized by a single easy axis. The rotation of magnetization direction in a single-domain particle with uniaxial anisotropy is decribed by [48, 49]

$$E = KV \sin^2 \theta \tag{1.19}$$

where θ is the angle between the easy axis of magnetization and the magnetization vector, K is the effective magnetic anisotropy constant and V is the particle volume. A schematic illustration of the energy of a single-domian particle with uniaxial anisotropy in dependence on the magnetization orientation is shown in figure 1.7. The energy barrier $E_B = KV$ separates the two minima at $\theta = 0$ and $\theta = \pi$ when the particle magnetization is parallel or antiparallel to the easy axis. When the thermal energy becomes comparable to the potential energy barrier E_B, the magnetization fluctuates between the two energy minima which is called the superparamagnetic relaxation. The superparamagnetic relaxation time τ, a function of energy barrier and temperature, is described by Neel-Brown expression,[49]

$$\tau = \tau_0 \exp\left(\frac{KV}{k_B T}\right) \tag{1.20}$$

where k_B is Boltzman constant and τ_0 is typically 10^{-9}s.[43] The observed magnetic behavior strongly depends on the measuring time t of the particular laboratory experimental technique with respect to the relaxation time τ, associated with the energy barrier. The measuring time varies from large values, as in magnetization measurements using VSM (vibration sample magnetometry) or SQUID (superconducting quantum

interference device) magnetometry (typically $t \approx 100\,\text{sec}$) to small values, like in Mossbauer spectroscopy (10^{-7}-10^{-11}sec). If $t >> \tau$, the system relaxation is faster than the magnetization orientation observed in this time window and the nanoparticles are said to be in the superparamagnetic regime. If $\tau >> t$, the system relaxation proceeds very slowly, and the nanoparticle appears to be locked into one of its two minima, which corresponds to the blocked regime.[49] The temperature at which the thermal energy induces a transition from the blocked state to the superparamagnetic state is defined as the blocking temperature, T_B. T_B depends on the characteristic measuring time t (defined by $t = \tau$).

$$T_B = \frac{KV}{k_B \ln\left(\frac{\tau}{\tau_0}\right)} \tag{1.21}$$

For VSM or SQUID magnetometry, the measuring time τ is usually 100s. Using this value for τ, the blocking temperature reduces to

$$T_B = \frac{KV}{25k_B} \tag{1.22}$$

From Eq.1.22 the blocking temperature is directly proportional to the volume of nanoparticles and its uniaxial anisotropy constant.

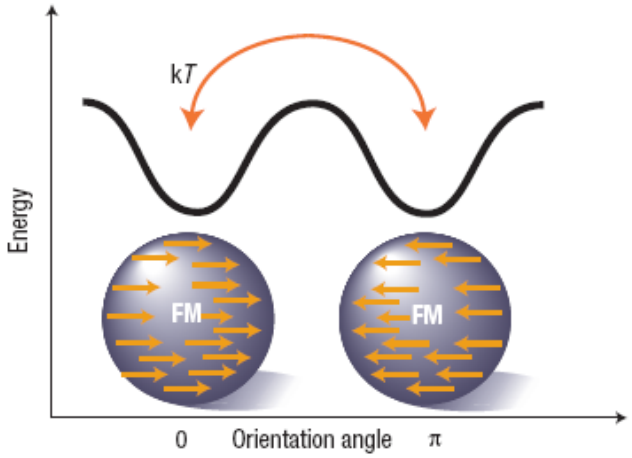

Figure 1.7: Schematic illustration of the energy of a single-domain particle in dependence on the magnetization orientation (from reference [50]).

The behavior of an assembly of single-domain nanoparticles in the superparamagnetic regime is analogous to an ensemble of paramagnetic atoms. The temperature dependence of the magnetization of an assembly of nanoparticles in the superparamagnetic regime can be modeled using Langevin function for $T > T_B$. In an applied magnetic field, the magnetization of superparamagnetic particles follow a Langevin behavior given by [49, 51]

$$M = M_s L\left(\frac{\mu H}{k_B T}\right) \tag{1.23}$$

μ is the single particle magnetic moment, M_s is the saturation magnetization due to N particles with magnetic moment μ, H is the applied field, k_B is the Boltzmann's constant, T is the temperature, and L is the Langevin function defined by

$$L(x) = \coth(x) - \frac{1}{x} \tag{1.24}$$

The Langevin function is a classical analogue of the Brillouin function that describes paramagnetism. For low magnetic fields or high temperatures, the particle magnetization is given by

$$M(H,T) = \frac{N\mu^2 H}{3k_B T} \tag{1.25}$$

The susceptibility of a superparamagnetic particle

$$\chi_{sp} = \frac{N\mu^2}{3k_B T} \tag{1.26}$$

which is the Curie's law.

Single-domain nanoparticles in the blocked state exhibit hysteresis in an applied magnetic field. Hence a remanent magnetization M_r and coercivity H_c exist in this ensemble of nanoparticles. The coercive field H_c is given by

$$H_c = \frac{2K}{M_s} \tag{1.27}$$

where K is the anisotropy constant, and M_s is the saturation magnetization.

1.3 Dilute Magnetic Semiconductors

Study of magnetic semiconductors started in late 1960s, with the aim of realizing a new functionality by combining semiconductivity (charge) and magnetism (spin).[52] Early studies of Cr spinels, rock-salt Eu chalcogenides and Mn-based chalcogenides led to the observation of a number of interesting phenomena associated with the interplay between ferromagnetic and semiconducting properties.[53] Among those, EuO, EuS and $CdCr_2S_4$ were the most extensively studied ferromagnetic semiconductors, in which the Curie temperature T_c does not exceed 100 K.[53, 54] The comparable low ordering temperatures, the poor semiconducting transport property, and the difficulty in growing these crystals limits the potential device application of these materials at room temperature.[26, 52-54] But EuS and EuO are of still scientific interest for their prototypical magnetic behavior, evident from the large number of magnetic studies in the last four decades (see section 1.1).

In early 1980s, studies on II-VI and III-V DMS material alloyed with Mn increased.[52, 54] The most thoroughly studied members of ternary $A^{II}_{1-x}Mn_xB^{IV}$ system include $Zn_{1-x}Mn_xTe$, $Cd_{1-x}Mn_xSe$ and $Cd_{1-x}Mn_xTe$.[26, 52] The magnetic properties of most of these materials are either paramagnetic, antiferromagnetic or spin glass behavior. These materials exhibit large Verdet constant that led to its application in optical isolators. Due to the much lower solubility of magnetic ions in $A^{III}_{1-x}Mn_xB^{V}$ DMS, little research was conducted on these materials until the late 1980s. However, the initial work by Munekata et al on molecular beam epitaxy grown InMnAs opened up III-V semiconductors as a potential host for DMS applications .[55] In 1996, Ohno et al reported

ferromagnetism in molecular beam epitaxy grown GaMnAs (T_c ~ 110 K).[56] The search for room temperature DMS received a great attention in 2000 after the prediction of Dietl et al that p-type ZnO doped with Mn would show ferromagnetism above room temperature.[57] Soon after Dietl's prediction, several groups reported the observation of room-temperature ferromagnetism in transition metal doped n-type ZnO systems.[58, 59] Mn doped group-III nitrides and phosphides were suggested as potential room temperature DMS. [27,60]

Another group of ternary system is IV-VI DMS with a fraction of the group IV element replaced by transition or rare earth metal ions. These materials have attracted attention because it allows us to study the effects of incorporation of magnetic ions with partially filled 3d or 4f states in a cubic structure. As compared to II-VI DMS, where the most commonly substituted magnetic ions are Mn, Fe and Co, the IV-VI DMS contain mainly Eu and Gd as the substituted magnetic ions. The most thoroughly investigated IV-VI DMS are lead chalcogenide based DMS. These materials are useful for various diode laser applications and for infrared detectors.[61] In $Pb_{1-x}Eu_xX$ (X= S, Se and Te), the Eu ions are incorporated into the cubic rock salt structure and are randomly distributed in the cation sites. The incorporation of a small amount of Eu into lead chalcogenide semiconductors produces changes in the energy band gap, lattice parameter and refractive index of the material. Another important feature of this material is that addition of Eu to the diamagnetic lead chalcogenides causes an antiferromagnetic exchange interaction, which is rather weak in comparison to $Pb_{1-x}Mn_xX$ DMS material. This is because the magnetic properties of rare earth ions depend on their f-shell electrons, which are

shielded and bound more closely to the nucleus than the d-shell electrons in Mn .[62] Since lead europium chalcogenides are promising materials for potential device applications, we decided to study the physical propereties of these materials in nanoscale.

1.4. Europium Chalogenides

Among the rare-earth monochalcogenides, Eu monochalcogenides (EuX, X=O, S, Se and Te) form a very interesting series due to their unique magnetic and electronic properties. For a number of years, EuX materials have been studied for their optical properties, their attractive magneto-optical response, and their robust ferromagnetic and antiferromagnetic properties.[1-7] These materials are called f-block compounds because of the dominant 4f electron orbital in the rare earth ion. These binary compounds crystallize in the rock salt structure. When they are pure, these materials are insulators. However, free carriers can be generated by suitable departure from stoichiometry.[12] The lattice parameters of these binary compounds continuously increase from 5.141 Å (EuO) to 6.598 Å (EuTe). At room temperature, the experimental electronic energy band gaps of EuO, EuS, EuSe and EuTe are 1.12, 1.65, 1.8 and 2.0 eV ,respectively.[10] The energy gap can be tuned over a wide range by alloying with lead chalcogenides.[63, 64]

Europium monochalcogenides display a very rich spectrum of magnetic properties, associated with the uncompensated $4f^7$ spin moments of Eu atom.[10, 11] EuO and EuS, whose Curie temperature (T_c) are 69.3 and 16.6 K, respectively, have been well known to be Heisenberg ferromagnets .[10, 12] EuSe is a metamagnetic semiconductor with a Neel Temperature T_N = 4.6 K. A mixed phase of ferrimagnetic and antiferromagnetic ordering appears in EuSe below 2.8 K. EuTe is an antiferromagnetic semiconductor with

Neel temperature T_N = 9.6 K. The physical properties of europium chalcogenides are summarized in Table 1.1. The electronic structure and the magnetic exchange interactions in europium chalcogenides will be discussed in the following section.

Table 1.1: Physical properties of bulk europium chalcogenides.

Material	a_0 (nm)	Magnetic Ordering	T_{Curie} (K)	Bandgap $_{T=300K}$
EuO	0.5141	Ferro	69.3	1.12eV/ 1.110 μm
EuS	0.5968	Ferro	16.6	1.65 eV/ 0.751 μm
EuSe	0.6195	Antiferro(II)/ Ferri/Antiferro (I)	1.8/2.8/4.6	1.80 eV / 0.689 μm
EuTe	0.6598	Antiferro(I)	9.6	2.00 eV / 0.620 μm

1.4.1 Electronic structure of europium chalcogenides

The relationship between electronic structure and optical properties in europium chalcogenides has been investigated experimentally and theoretically by several research groups.[3, 65, 66] Among the sixty three electrons of the europium atom, fifty four saturate the orbital giving the Xenon configuration; the nine remaining ones exist in the configuration $4f^7 5d^0 6s^2$. Due to the strong electron affinity of the chalcogens, the two 6s electrons of the Eu atoms are transferred to saturate the p orbitals of X in EuX compounds. In EuX compounds, the valence band is formed by the p states of the anion, and the conduction band is built up with 5d states at the lower edge and 6s state at the higher edge. The 4f levels in europium chalcogenides are situated between the p-valence

band of the anion and the 5d conduction band of Eu^{2+}. The crystal field effects split the 5d states of conduction band into two levels, the lower energy $5dt_{2g}$ states and the upper energy $5de_g$ states.[12, 65]

To interpret the absorption spectra of europium chalcogenides, Busch et al [65] established an energy level scheme, which provides useful information about the width of 5d-states and the crystal field splitting. The proposed energy level scheme of the four europium chalcogenides is shown in figure 1.8. The crystal field effects on the d states, split the 4f-5d transition in to $4f^7$-$4f^6$ $5dt_{2g}$ and $4f^7$-$4f^6$ $5de_g$. The absorption edge corresponds to $4f^7$-$4f^6$ (^7F_J)$5dt_{2g}$ transitions, where the final state is combined of one 5d-electron and six 4f electrons. The ^7F_J - multiplet (J = 0,1,2,3,4,5,6) of the six 4f electrons is superimposed on the $5dt_{2g}$ band and is illustrated in the ladder structure of the $5dt_{2g}$ band. The absorption edge E_g increases from EuO to EuS, EuSe and EuTe,and ranges from E_g=1.1eV in EuO up to 2 eV in EuTe (see table 1.1). This shift is due to the decrease of crystal field energy (shrinking of the splitting energy between the t_{2g} and e_g states) with increasing lattice constant. The width of $5dt_{2g}$–band varies from 1.1 eV for EuO, 0.7 eV for EuS and EuSe and 0.6 eV for EuTe. The reported values of crystal field splitting are 3.1 eV for EuO, 2.2 eV for EuS, 1.7eV for EuSe and 1.5 eV for EuTe.

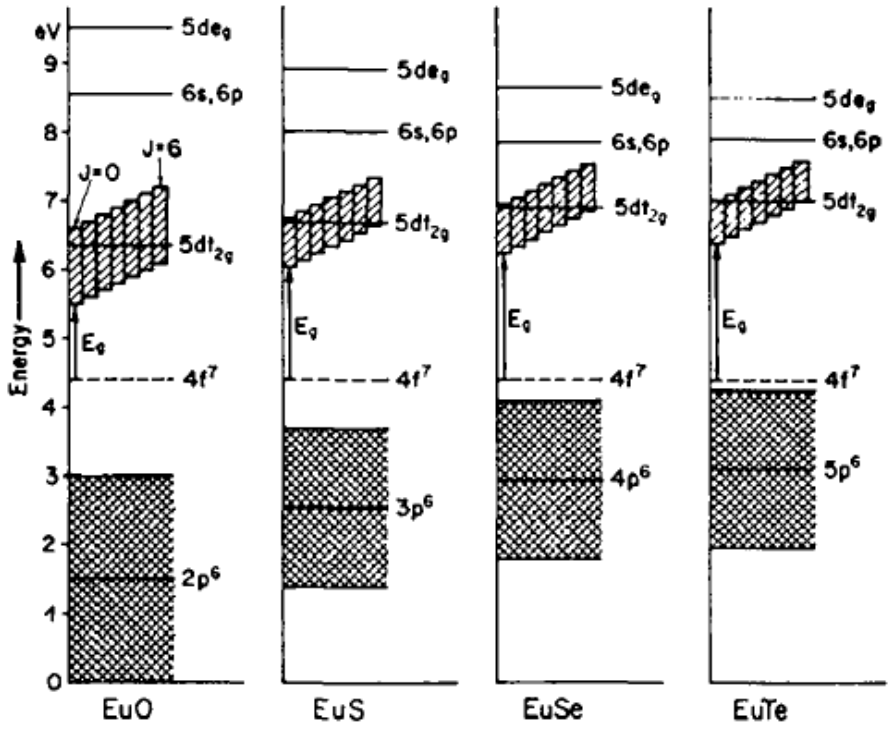

Figure 1.8: Energy level schemes of europium chalcogendes at room temperature (from reference [65]).

The energy level scheme of EuS at room temperature, proposed by Busch et.al [65] is shown in figure 1.9. In addition to the two main transitions, other possible transitions include 4f-(6s, 6p), charge transfer transition from the p^6-valence band of the anions into the (6 s, 6 p)-state and p^6-valence band into the $5dt_{2g}$ and $5de_g$ –states.

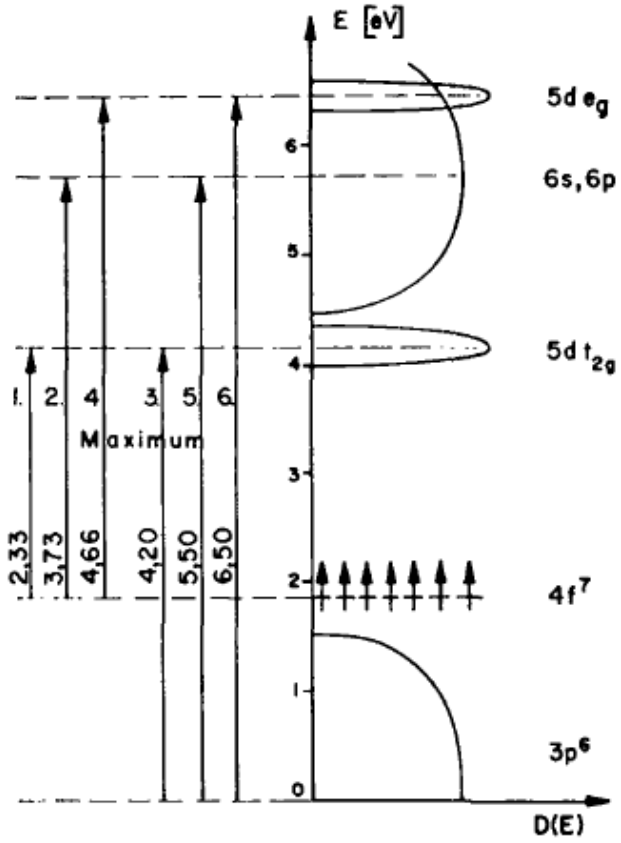

Figure 1.9: Energy level scheme of EuS at room temperature (from reference [65]).

1.4.2 Magnetic properties of europium chalcogenides

The magnetic properties of europium chalcogenides is caused by the half filled 4f shell of the Eu^{2+} cations. From Hund's rule [12,67] the seven 4f electrons have their spin parallel, and accordingly the lowest energy multiplet has S = 7/2, L=0 and J=7/2. The atomic energy levels are characterized by a term symbol of general form $^{2S+1}L_J$. Using the term symbol, the ground term of Eu^{2+} is $^8S_{7/2}$.

In rare earth compounds, the majority of 4f electrons lie well inside the 5s and 5p closed shells and, thus are well screened by them. As a result, the direct exchange interaction due to the 4f-4f overlap between nearest –neighbour sites is weak.[46] Hence, in contrast to the direct exchange coupling of the 3d electrons in nickel, iron or cobalt, only indirect coupling via conduction electrons (ferromagnetic indirect exchange) or via the ligands (antiferromagnetic super exchange) is possible in 4f ferromagnetic materials. This indirect exchange coupling is much weaker than the direct coupling, and in consequence, the Curie temperatures of the 4f ferromagnetic materials are lower than the Curie temperatures of the 3d ferromagnetic materials. This is why Fe and Co are more widely employed than EuS.

Since these materials show pure spin magnetism due to strongly localized electrons and almost negligible anisotropy, europium chalcogenides are considered to be models for Heisenberg magnets. The magnetic interaction can be written as [46]

$$H_{exchange} = -\sum_{i,j} J_{ij}\,\vec{S}_i \cdot \vec{S}_j = -\sum_{nn} \vec{J}_1 \vec{S}_0 \cdot \vec{S}_{nn} - \sum_{nnn} \vec{J}_2 \vec{S}_0 \cdot \vec{S}_{nnn}$$

J_{ij} is the exchange constant between the i^{th} and j^{th} ion site , S_i is the spin of the i^{th} ion and S_j is the spin of the j^{th} ion.

Indirect Exchange mechanism (J_1) : For the indirect exchange constant J_1, the cation wave functions have a more important role, and the anion p bands are relatively unimportant. Since the overlap among the cation wave functions is most significant between nearest neighbor (nn) cations, the principal contribution of this indirect exchange mechanism is to J_1. This indirect exchange consists of a virtual transfer of an electron

from the 4f shell to the empty 5d shell of the same Eu^{2+} ion ,then to another 5d shell of the neighboring Eu^{2+}ion .[12, 46, 68] The larger radius of the 5d shell provides sufficient overlap with the orbital of the neighbor atoms. The indirect exchange is supposed to increase rapidly as both the lattice constant decreases and the overlap of the 5d orbital increases.

Antiferromagnetic Super exchange mechanism (J_2): In this mechanism, the wave functions of the anion play an important role in exchange coupling between next nearest neighbors, because this may be mediated by the p electron of the anion. For the rock salt structure, the anion wave function connects the two nn cations, which are next nearest neighbor (nnn) to each other. Therefore the superexchange mechanism provides the principal contributions to J_2. The super exchange mechanism through the d-f exchange interaction is the main mechanism of J_2 in EuS,EuSe and EuTe.[12, 46]

In d-f exchange interaction, the anion p electron is transferred to a 5d state of the nearest cation and, then experiences the d-f exchange interaction. In principle, a transfer to the 6s state is possible, but the s-f exchange interaction is much weaker than the d-f one, so that the resulting contribution to J_2 is negligible. The d-f exchange interaction can be much stronger since the overlap between the p and d states is much larger .[12]

Summary: Review of magnetic interactions in solids, and a general discussion of magnetic and dilute magnetic semiconductors were described. Electronic structure of EuX, in particular EuS was reviewed. To understand the origin of magnetism in europium chalcogenides, different exchange mechanisms were discussed.

CHAPTER II

EUROPIUM SULFIDE NANOCRYSTALS: SOLID STATE THERMOLYSIS & CHARACTERIZATION

2.1 Introduction

In the mid 1990s, researchers began investigating nanocrystalline forms of europium chalcogenides, motivated by the possibility of their use in nanotechnology employing their magnetic, optical and magneto-optical properties.[15-17] Several groups have studied EuS nanoparticles in a variety of nanoscale size regimes and embedded in various media.[9, 21, 22] Enhancements in their physical properties have been observed as a function of the size of the nanocrystal.[8, 9, 13, 14, 21-25] These traits could prove to be useful for nanomaterial applications, which could supersede those based on bulk EuS or on other magnetic materials.[69-71] Due to the challenges in the synthesis processes, as well as the observed spontaneous surface oxidation of EuSe, EuTe and EuO nanoparticles,[72-74] we have opted to investigate the size-dependent variations in the magnetic, optical and magneto-optical properties of EuS materials. In studying size effects in the physical properties of nanoparticles, it is important to employ synthesis techniques that offer control over the size, size dispersion, shape, surface properties and produce materials with high crystallinity.[21]

Several approaches have been developed over the past decade for the synthesis of EuS nanocrystals (NCs). Nanocrystalline europium sulfide was first reported by Gambino in the early 1990s.[1, 2] Zeolite-assisted synthesis of EuS nanoclusters occurred

some years later .[22] The first liquid-phase synthesis of EuS was reported by Thongchant et.al, which involved the reaction of europium metal and H_2S in liquid ammonia.[18] Since then, other techniques have been developed to synthesize these materials, including white light-emitting diode (LED) and microwave irradiation of single-source precursor as well as employing thiourea as sulfur source .[14, 71, 75] The challenges in these techniques have been to produce monodispersed nanoparticles at the smallest sizes. Zhao and collaborators conducted a recent study that employed thermal decomposition of the single-source, molecular precursor to produce EuS NCs at a variety of sizes and narrow size distribution.[8, 9] Relatively successful approaches have involved low temperature solvothermal synthesis of a dithiocarbamate precursor in a solution of oleylamine and triphenylphosphine as well as a single precursor of a dithiocarbamate complex.[21, 23, 70] Since many organo-chalcogenide complexes of metals decompose thermally to metal chalcogenides, the solvent-free and controlled thermal decomposition of single-source molecular precursors has proven to be an effective method for synthesis of EuS nanocrystals.[76] Redigolo et.al reported the synthesis of the smallest EuS nanocrystals ($d_{NC} \sim 1.8$ nm) using a similar thermolysis procedure .[25] The nanocrystals in this size regime exhibit interesting optical, magnetic and magneto-optical properties.

In this chapter, the solid state synthesis technique of EuS nanoparticles using a single-source molecular precursor and characterization of the as-produced materials is discussed. The size and crystallinty of the EuS nanoparticles were characterized using Transmission Electron Microscopy (TEM) and powder X-ray Diffractometry (XRD). The optical properties of the materials were probed using absorption spectroscopy and

photoluminescence techniques. The magnetic susceptibility of our nanocrystals was studied as a function of temperature and field. Mossbauer absorption spectra of EuS nanocrystals at different temperatures were obtained and are discussed.

2.2 Experimental details

EuS nanocrystals were synthesized via a two-step technique involving precursor precipitation and synthesis through thermolysis [9, 69] First, single source Eu (II) precursor was prepared from commercially available chemicals. In the second stage, EuS nanocrystals were synthesized via the thermal decomposition of the single source precursor.

2.2.1 Precursor preparation

Single source precursor Eu diethyldithiocarbamate complex with 1, 10-phenanthroline (hereafter referred to as $Eu(ddtc)_2Phen$) was prepared as described by the authors elsewhere.[9, 13] All synthetic steps were conducted inside a dry glove box under nitrogen atmosphere and at room temperature using anhydrous solvents. 1, 10-phenanthroline (≥99%), methanol (anhydrous 99.8%), europium (II) chloride (99.99% trace metals basis), and diethyldithiocarbamic acid diethylammonium salt (97%) were purchased from Sigma Aldrich. All the chemicals were used as-received without further purification. Under a nitrogen atmosphere and with vigorous stirring, a 1mM methanolic solution of 1, 10 phenanthroline was added to a 1mM methanolic solution of europium (II) chloride followed by the addition of a methanolic solution of 2mM of diethyl ammonium diethyldithiocarbamate producing a lustrous, dark-grey precipitate. The EuS

precursor precipitate was isolated by centrifugation, washed three times with methanol, and dried under vacuum.

2.2.2 Solid state thermolysis

For the synthesis of EuS nanoparticles , the precursor was transferred to a porcelain boat and was inserted into a quartz tube in a horizontal tube furnace (Thermolyne #F21135, Barnstead International) for a time-sensitive mass reduction step under a stream of dry, ultra pure nitrogen for 1h at 700 ºC. Thereafter, the resultant solid was cooled gradually to room temperature. Adjustment to the thermolysis time, temperature, and precursor concentration yielded EuS nanocrystals of a variety of sizes, devoid of ligand molecules. Schematics of a conventional tube furnace used for thermolysis is shown in figure 2.1. The nanomaterials were dispersed in 2,2'-bipyridine to inhibit the spontaneous formation of a non-magnetic surface layer of Eu_2O_2S.[21]

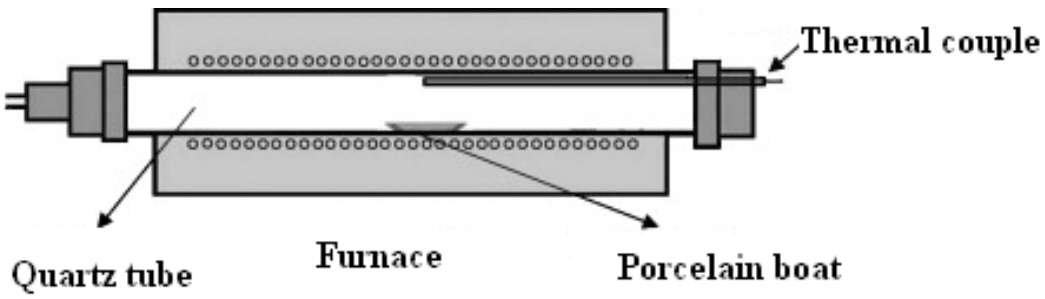

Figure 2.1: Schematics of a conventional tube furnace used for thermolysis. The precursor powder was poured onto the bottom of a porcelain boat and flattened. The boat was inserted into the center of the quartz tube, mounted inside the tube furnace and sealed on both ends with quartz caps (from reference [77]) .

2.2.3 Characterization techniques

A TGA-1000 (Scientific Systems Inc.) thermogravimetric analysis system was employed to determine the thermal decomposition of Eu $(ddtc)_2$Phen. A small amount (~ 10 mg) of the precursor was placed in a platinum weighing pan and was heated across a temperature range from 25 ºC up to 900 ºC at a heating rate of 10 ºC min^{-1} under nitrogen atmosphere. Fourier transform infrared spectroscopy (FT-IR) was used to investigate the molecular bondings of the precursor complexes. Infrared spectra of the precursor were measured in the range 500-4000cm^{-1} as pressed pellets in KBr on a Thermo-Nicolet 300 Fourier transform infrared (FT-IR) spectrometer. X-ray diffraction (XRD) measurements of our nanocrystals were obtained using a Scintag X1 system with a Cu $K_{\alpha 1}$ radiation (λ = 1.5406 Å). Thin films of the as-synthesized nanocrystals were dropcasted on a silicon plate <511> for XRD measurements. The nanocrystal size and size distribution were investigated using a Philips CM 20 transmission electron microscope (TEM) operating at 200 kV. Methanolic solutions of the EuS nanocrystals were dropcasted onto holey carbon films (a fine layer of carbon with holes of desired size in the carbon) mounted on TEM specimen grids (Ted-Pella). UV-VIS absorption spectra of EuS NCs solutions were measured at room temperature with a Cary 5000 UV-vis-NIR spectrometer (Varian). Photoluminescence (PL) experiments were performed using a Fluorolog 3 FL3-111 spectrophotometer, equipped with 450 W Xenon lamp and photomultiplier tube. Vibrating sample magnetometry (VSM) measurements were conducted with a Quantum Design Physical Property Measurement (PPMS) System. The system consists of a 17 Tesla superconducting magnet and a VSM linear motor. Control of the sample temperature is regulated with a combination of liquid nitrogen and liquid

helium. This allows measurements to be performed at temperatures ranging from 2 K to 300 K.

2.3 Results and discussion

2.3.1 Precursor characterization

To assess the suitability of the precursor, thermogravimetric analysis was performed across a temperature range from 25 ºC to 900 ºC at a heating rate of 10 ºC min^{-1} under nitrogen atmosphere. The thermogravimetric analysis (TGA) and the derivative thermogravimetric (DTG) curve, which characterize the thermal decomposition of $Eu(ddtc)_2Phen$, were presented in Figure 2.2. The TGA curve represents the variation of mass with temperature and DTG curve represents the rate of mass change per temperature interval. The starting precursor mass of the analysis was 7 mg. The EuS precursor decomposed in two steps. The majority of the mass loss, approximately 50 %, occurred in the 100 ºC to 350 ºC temperature range. This corresponds to pronounced peaks in the DTG curve at 200 ºC to 232 ºC ,which indicates the rapid, vigorous decomposition of the single source precursor and the initial nucleation and growth of the EuS nanoparticles. Another smaller transition in the TGA designated a second stage in the decomposition process. This occurred in the 500 ºC to 625 ºC temperature range. The corresponding DTG curve displayed the maximum decomposition rate at 588 ºC with a mass loss of 12.5 % during the transition. 12.5% change represented the decomposition of residual inorganic and organic compounds of the initial precursor material, yielding the final product at the end of decomposition.[25]

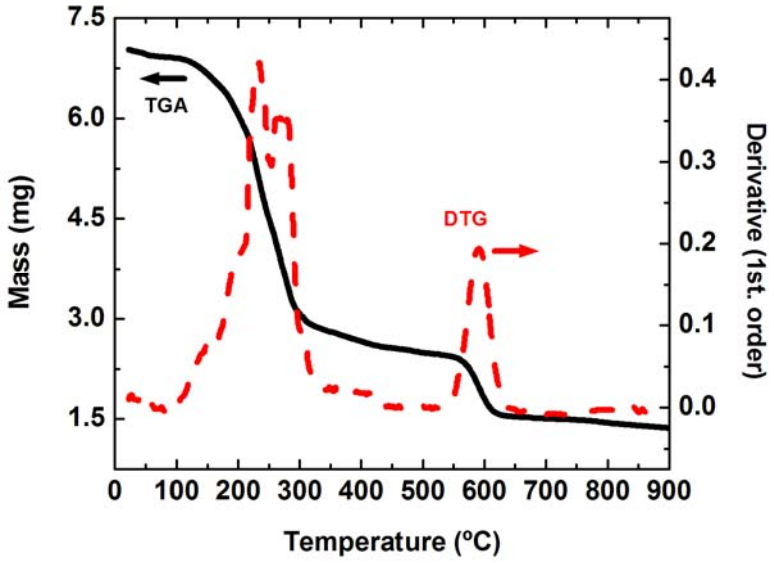

Figure 2.2: TGA and DTG analysis of $Eu(ddtc)_2Phen$ complex.[25]

Fourier transform infrared spectroscopy was used to investigate the molecular bondings of the precursor complex. FTIR spectra of the $Eu(ddtc)_2Phen$ complex , shown in Figure 2.3, displayed characteristic peaks from the 1,10-phenanthroline ligand at 1620,1589,1572 and 1516cm^{-1} attributed to the skeleton vibration mode of the benzene ring in addition to the peaks at 843 and 731cm^{-1}, which are assigned to the bend vibration mode of C-CH in the complex. The vibration mode at 1482 cm^{-1} was assigned to C-N stretching of the organic products. We observed vibration modes between 900-1100 cm^{-1} (C-S stretching). The observed features correspond to the ones previously reported.[9, 75]

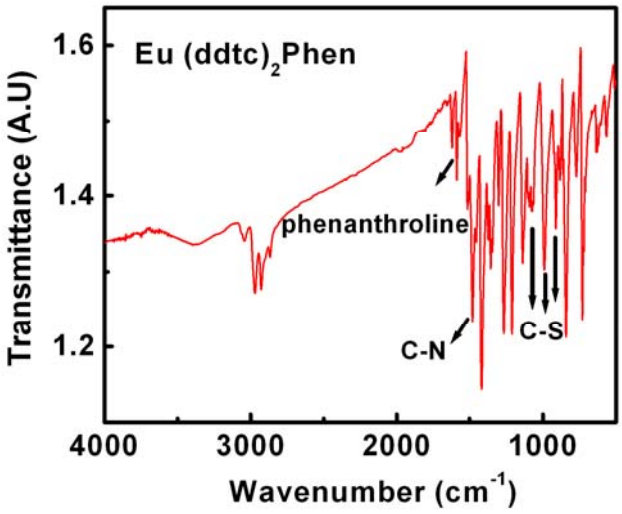

Figure 2.3: Fourier transforms infrared spectra of Eu $(ddtc)_2$ Phen complex.

2.3.2 Structural characterization

Our assessments of the structure of the EuS nanocrystals included X-ray diffraction (XRD) and transmission electron microscopy (TEM). XRD and TEM measurements assisted the indication of the atomic arrangement, that is, the crystallinity of the nanocrystals. An XRD analysis of the EuS nanocrystals (Figure 2.4) confirmed the high crystallinity of the nanomaterial by matching the primary diffraction peaks obtained with those of bulk EuS. The EuS compound was identified by major diffraction peaks at the 2θ angles of 30.0°, 42.8°, 50.7° and 53.4°,which match the Powder Diffraction File (JCPDS # 26-1419) for this material and correspond respectively to the (200),(220),(311), and (222) planes of fcc EuS. The average size of EuS nanocrystal can be calculated using Scherer equation;

$$L = \frac{K\lambda}{\beta \cos(\theta)} \; ; \qquad (2.1)$$

where K is the Scherer constant, λ is the wavelength of radiation, β is the full width at half maximum and θ is the Bragg angle. We attempted to identify the size of our nanocrystal with Scherrer analysis. The diameter of the nanocrystals determined from the analysis was ~ 19.6 nm, which was significantly different from the diameter (~ 20.5 nm) measured from the TEM images. No additional XRD peaks were observed due to impurities or surface oxidation.

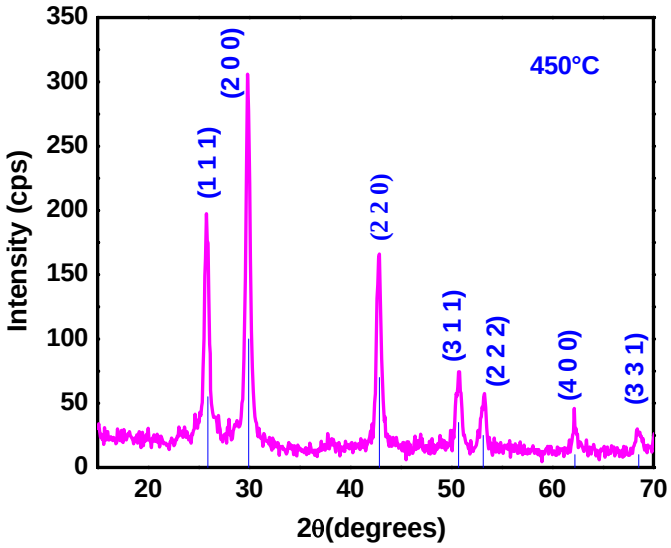

Figure 2.4: XRD spectrum of the EuS nanocrystals which were synthesized in the following thermolysis conditions (temp: 450°C, time: 1 hr and precursor mass: 100mg). [78]

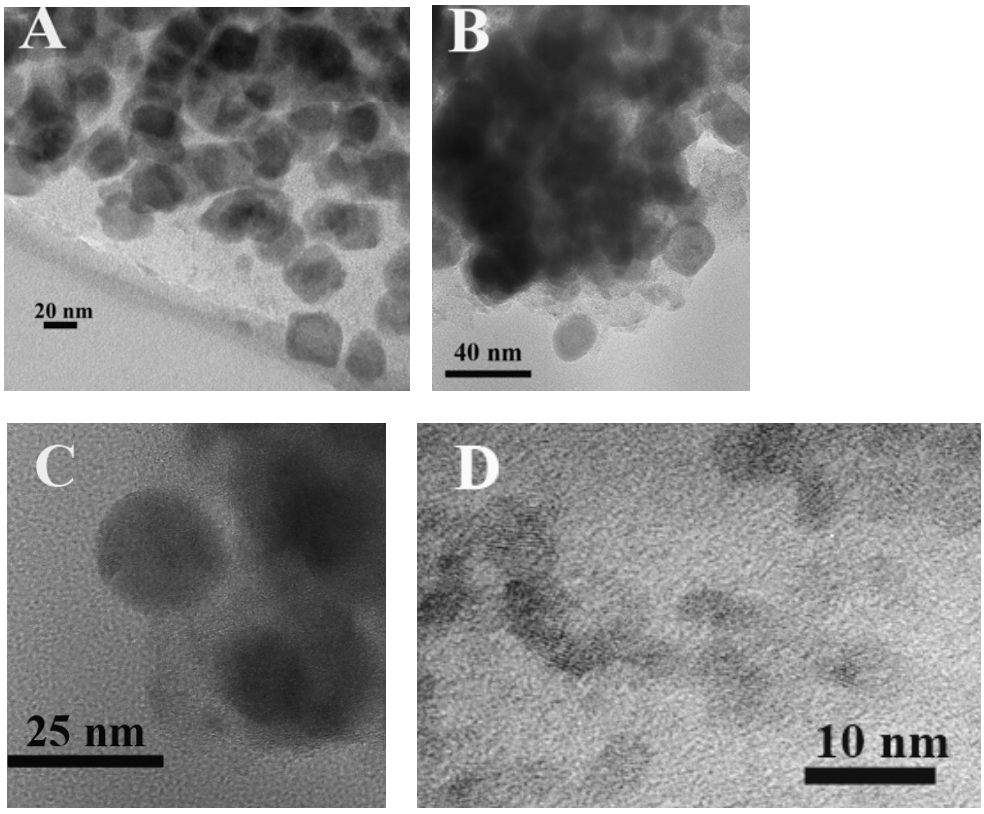

Figure 2.5: TEM images of EuS nanocrystals grown at different thermolysis conditions. (A) TEM images of ~ 30 nm, (B) &(C) ~ 20.5 nm and (d) ~ 4 nm (Image C from reference[78]).

Figure 2.5 displayed HRTEM images of the different EuS nanoparticles obtained from the thermolysis of a single molecular precursor. By varying the decomposition conditions of the europium precursor complex, nanocrystals of varying sizes and shapes could be obtained. The nature of decomposition depends on its chemical environment in addition to the thermal conditions. The sensitivity of the decomposition process of europium precursor complex leads to a variation in nucleation and growth kinetics,

resulting in the formation of nanocrystals with various shapes and sizes.[70]. The shape of the nanoparticle was predominantly cubic when the particles were larger than 30 nm (Figure 2.5 (A)) explained by the dependency on the surface energies of specific crystalline faces.[79, 80] Figure 2.5 (B&C) revealed a predominance of monodisperse spherically –shaped nanoparticles with sizes ~ 20.5 nm. The size of the particles can be controlled in a wide range with the smallest one down to 4 nm (Figure 2.5 D).

Redigolo et al reported the synthesis of quantum confined, sub-2.0 nm EuS nanocrystals, employing the thermolysis procedure of a single source EuS precursor.[13] Figure 2.6.a showed a group of quantum confined EuS nanocrystals with an average diameter of 2.0 nm. Selected area electron diffraction (SAED) patterns of the nanocrystals are presented in Figure 2.6.b. The measured ring diameters match the values for the (200), (222), and (311) planes of fcc EuS.

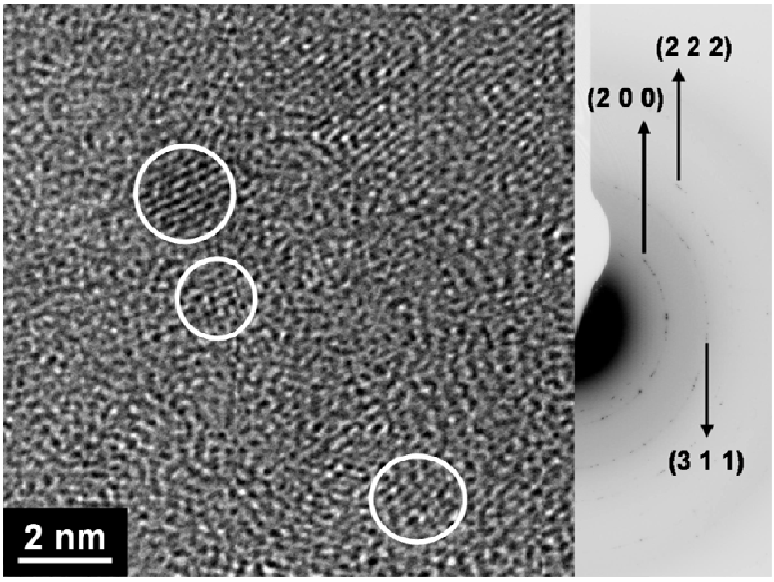

Figure 2.6: (a) TEM micrograph of sub-2.0 nm EuS nanocrystals (b) SAED pattern of the nanocrystals (from reference [13]).

2.3.3 Optical characterization

We characterized the optical properties of EuS NCs via UV-visible absorption and fluorescence spectroscopy as seen in Figure 2.7. The optical traits of europium chalcogenides arise from the 4f-5d dipole transitions of Eu^{2+} ion. This means that a localized f electron is excited into an itinerant conduction band, which is predominantly of rare earth d character. It was concluded that in bulk EuS, the fundamental absorption edge is due to the onset of Eu^{2+} 4f to 5d transitions of the type $4f^7(^8S_{7/2}) \rightarrow 4f^6(^7f_J)5d^1$; although, anion p-valence band to Eu conduction band transitions may be involved.[81] In bulk EuS, the broad emission band is attributed to the transition of $4f^6 5d^1$ to $4f^7$ of Eu^{2+}.[69] Compared to EuS bulk, we did not observe a clear size-dependent shift in the absorption and luminescence peak energy for 20 nm EuS NCs. To determine whether our nanocrystal diameter resided within the quantum confinement regime for excitons in EuS, we calculated the exciton Bohr radius, using an effective mass[82] of $0.3m_0$ and a dielectric constant [83] of 10.2. A lack of quantum confinement is expected, as the nanocrystals prepared in this study are much larger than the calculated EuS Bohr exciton radius of ~ 1.8 nm. Huxter et al also reported a bulk-like optical absorption spectra for 23 nm diameter EuS nanoparticle.[84] Redigolo et.al reported a blue shift in the emission spectra of sub-2 nm EuS NCs, which was attributed to the combination of surface strain phenomena and strong quantum confinement.[69]

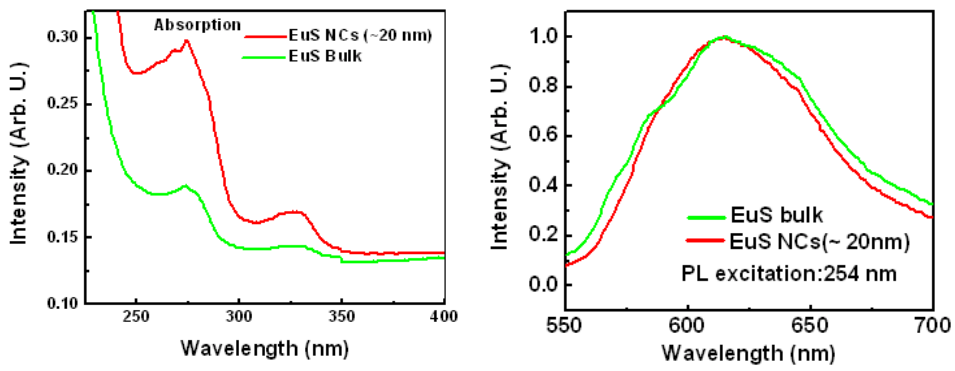

Figure 2.7: Absorption and luminescence spectra of EuS bulk and EuS nanocrystals of ~ 20 nm diameter.

2.3.4 Magnetic characterization

Vibrating sample magnetometry, conducted with a Quantum Design PPMS system, provided characterization of the magnetization as a function of temperature, m(T), and the magnetization as a function of applied field, m(H). Zero field cooled (ZFC) measurements of m(H) involve cooling the sample in zero field to a desired temperature and then cycling the applied field. Field –cooled (FC) measurements of m(H) were conducted in a similar manner; however, the sample is cooled in the presence of a non-zero applied field. In ZFC measurements of m(T), the sample is cooled under zero applied magnetic fields to a temperature well below its Curie temperature and its blocking temperature (T_B). The system is then warmed up, and the magnetization is measured as a function of temperature by applying a relatively low external magnetic field. Field cooled (FC) measurements of m(T) were conducted in a similar manner; however, the sample is cooled in the presence of a non-zero applied field.

In Figure 2.8 we present the ZFC-FC results of ~ 14 nm diameter EuS NCs measured in the field of 100 Oe. As the NCs are cooled in zero applied field, the direction of the total magnetic moment of each particle is frozen in random arrangement and the collection of particles will have a very low or zero net magnetization. When a magnetic field is applied and the magnetization is measured as a function of temperature, some fraction of the particles will begin to align with the field, and the magnetization will increase with increasing temperature. The magnetization continues to increase until a peak in the ZFC data is observed. The position of the peak locates the blocking temperature at which the nanoparticles make a transition from the blocked state to the superparamagnetic state.[85-87] Above the transition temperature, the NCs are superparamagnetic, as evidenced by the decay in the magnetization. For the 14 nm sample, the blocking temperature was found to be ~ 12 K. The Curie transition temperature of this nanoparticle is around 17 K. As a typical blocking behavior of superparamagnetic nanoparticles, the EuS nanoparticles show a different magnetization process in the FC curve. When the sample is cooled under a magnetic field, the direction of the magnetic moment of each nanoparticle is frozen to the field direction as the temperature decreases below the blocking temperature. As a result, the field cooled sample shows the highest susceptibility at 7 K and it decreases steadily with increasing temperature. After the temperature rises above the blocking temperature, the FC plot overlaps with the ZFC plot.

The magnetic anisotropy constant K of the as-prepared sample can be calculated by the followed formula [9]:

$$K = 25 k_B T_B V^{-1} \quad (2.2)$$

where k_B is the Boltzman constant, T_B is the blocking temperature of the samples, and V is the volume of the particles, where the samples are presumed to be spherical. The calculated magnetic anisotropy constant K of our samples is around 3.6x 10^3 ergs/cm^3, which is slightly larger than that of the K values reported for 14 nm EuS (~ 2.5x 10^3 ergs/cm^3). [9] Zhao et.al reported an increase in K with decrease in particle size.[9]

Figure 2.9 illustrates the magnetization hysteresis curves of EuS sample (d_{NC} ~ 14 nm) for a cycling field of ±16 T. We surveyed the magnetization response across a temperature range from 2 to 25 K, which includes the Curie temperature (~ 17 K) for bulk EuS. A pronounced saturation magnetization was observed for sample at 2 K. Saturation magnetization was calculated by extrapolating the magnetization versus the inverse of the field (1/H) curve to 1/H = 0.[86] The saturation magnetization of the sample at 2 K was estimated as 131 emu/gm, which is in agreement with the previous reports.[9, 19]

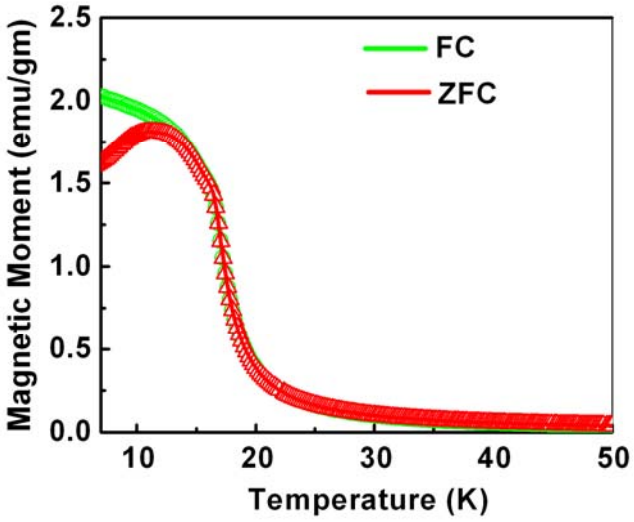

Figure 2.8: ZFC and FC data of m(T) for the EuS sample (d_{NC} ~ 14 nm) for applied field strengths of 100 Oe.

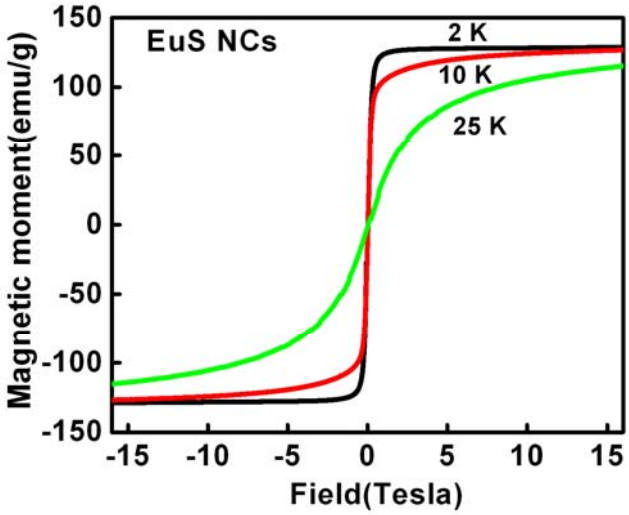

Figure 2.9: High field magnetization hysteresis graphs for the EuS sample (d_{NC} ~ 14 nm) measured at 2 K, 10 K and 25 K.

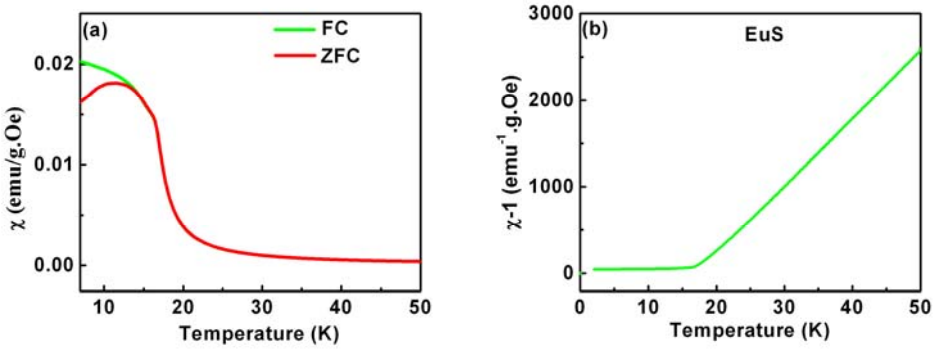

Figure 2.10: (a) ZFC-FC measurements of the magnetic susceptibility χ as a function of temperature. (b) Inverse magnetic susceptibility χ^{-1} as a function of temperature (FC condition).

The temperature variation of magnetic susceptibility χ and the inverse susceptibility χ^{-1} of EuS sample ($d_{NC} \sim 14$ nm) for the ZFC-FC case measured at a field of 100 Oe are shown in Figure 2.10. In the χ^{-1} plot, the magnetic data above 25 K can be well fitted to the Curie-Weiss law with Weiss temperature (θ) = 17.45. We calculated the effective number of Bohr magneton of Eu^{II}, $\mu_{eff} \approx 4.3$, using the Weiss constant. The theoretical effective number of Bohr magneton for Eu^{II}, $\mu_{eff} = g[J(J+1)]^{1/2}$: total angular momentum J =7/2, gyromagnetic ratio g ≈ 2 was calculated to be 7.94. This discrepancy may be from the contribution of Eu^{III} ions on the surface, as a free ion has a non-magnetic ground state (total angular momemtum J=0). Mossbauer spectroscopy studies (see section 2.3.5) showed that the Eu^{II} ions on the surface could be partially oxidized to Eu^{III} ions while exposing in air. Incongruities in the estimations obtained for the Bohr magneton for Eu^{II} in EuS NCs may be due to the presence of remnant organics in the sample and surface oxidation.

The temperature dependence of χT for EuS nanocrystal (d_{NC} ~ 14 nm) was shown in Figure 2.11. The rapid rise in χT as the temperature is cooled below ~20 K is indicative of ferromagnetic interactions. The value of χT reaches a maximum and then rapidly decreases below T_c as a result of moment saturation.[23] Zhao et.al reported a quasi-ferrimagnetic behavior due to surface oxidation (anomalous magnetic phenomenon of slight increase of χT at high temperatures) for 14 nm EuS NCs, which was not observed in our case.[9]

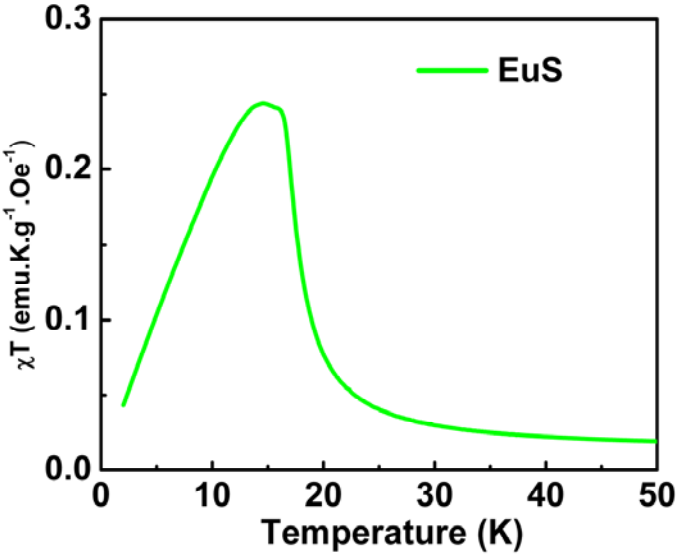

Figure 2.11: Temperature dependence of χT of EuS nanocrystals (FC condition).

2.3.5 Mössbauer spectroscopy

Mössbauer spectroscopy is a versatile technique that can be used to provide information about the crystal structure, electronic valence, and magnetic states of atom in a solid. The Mössbauer spectra obtained from the resonant and recoil -free emission and absorption of gamma rays by nuclei are described by three parameters. The chemical

isomer-shift of the nuclear energy levels arises from the difference in electron densities at the nuclear sites between the emitting and absorbing atoms, and is useful for determining the electronic valence state. Quadrupole splitting arises from the asymmetry in the electric field gradient at the nucleus of the chemically bonded atom. It is a crystal structure sensitive component and usually appears as a doublet in the spectrum.[88] The magnetic hyperfine splitting is caused by the magnetic dipole interaction between the nuclear spin moment and the magnetic field. The effective magnetic field experienced by the nucleus is a combination of the applied field and the hyperfine field. The major component of the hyperfine field arises from unpaired spins of partially filled electron in the d or f orbital of the atom which in turn causes a slight imbalance in the s electron spin density at the nucleus. This is usually called the Fermi contact field.

We probed the magnetic hyperfine splitting in bulk EuS and EuS nanocrystals (d_{NC}~20nm) using Mössbauer spectroscopy. A brief review of superparamagnetic relaxation is necessary to describe the hyperfine splitting associated with the magnetic nanoparticles (see section 1.2.3 for a more detailed discussion). Spherical nanoparticles are generally considered as having uniaxial anisotropy, which is characterized by a single easy axis. The rotation of magnetization direction in a single-domain particle with uniaxial anisotropy is described by [49]

$$E = KV\sin^2\theta \tag{2.3}$$

where θ is the angle between the easy axis of magnetization and the magnetization vector, K is the effective magnetic anisotropy constant and V is the particle volume. The energy barrier $E_B = KV$ separates the two minima at $\theta = 0$ and

$\theta = \pi$ when the particle magnetization is parallel or antiparallel to the easy axis. When the thermal energy becomes comparable to the potential barrier E_B, the magnetization fluctuates between the two energy minima giving rise to the superparamagnetic relaxation. The superparamagnetic relaxation time τ is a function of the energy barrier and temperature and is described by the Neel-Brown expression[49],

$$\tau = \tau_0 \exp\left(\frac{KV}{k_B T}\right) \qquad (2.4)$$

where k_B is Boltzman's constant and τ_0 is typically 10^{-9}s .

In order to observe the magnetic behavior it is necessary to select the appropriate time window for the measurement. The time window (t) for Mössbauer spectroscopy is approximately 10^{-7} to 10^{-11} sec. If $t >> \tau$, the superparamagnetic relaxation between the nanoparticles is faster than the magnetic relaxation within each nanoparticle and the nanoparticles are said to be in the superparamagnetic regime. If $\tau >> t$, the superparamagnetic relaxation proceeds very slowly, and the nanoparticle appears to be locked into one of its two minima, which corresponds to the blocked regime. The temperature at which the thermal energy induces a transition from the blocked state to the superparamagnetic state is defined as the blocking temperature.

Mössbauer measurements and data analysis of EuS samples were performed at Argonne National Laboratory by Dr. Dennis Brown (Northern Illinois University) and Dr. Charles Johnson (University of Tennessee Space Institute). Mössbauer ^{151}Eu measurements were made on EuS samples over a temperature range of 5 K to 480 K

using a Janis SVT-400 cryostat, where the temperature was stabilized to within 0.1 K. The measurements were performed in transmission geometry with a $^{151}Sm_2O_3$ source kept at room temperature and a Canberra GL0515R/S Germanium detector. The samples consisted of about 16 mg of EuS (approximating 4 mg/cm^2 of Eu), and, for good thermal homogeneity across the samples during measurements, they were placed on 25 micron aluminum foil. The calibration of the Mössbauer spectra was done using a ^{57}Co (in Rh matrix) source and a 6 micron Fe foil as the absorber.

Mössbauer spectra of bulk EuS sample in powder form was recorded at different temperatures (295 K, 16 K, 15 K and 5 K) were shown in figure 2.12. In the paramagnetic region of the divalent compound EuS (295 K), the internal magnetic field at the nucleus is averaged out giving rise to a singlet in the Mössbauer pattern. The isomer shift of -12.0 mm/sec corresponds to Eu^{2+} confirming the divalent nature of EuS. The singlet split continuously to hyperfine levels as the sample temperature decreased below the blocking temperature [89]. At 5 K, a typical well resolved hyperfine spectrum was observed. For ^{151}Eu nuclei, the excited state is a spin I_e=7/2 state and the ground state has spin I_g=5/2. Under the influence of a magnetic field, the excited state splits into eight hyperfine levels and ground state into six hyperfine levels. Using the magnetic dipole selection rule $\Delta m_I = 0,\pm 1$, 18 hyperfine transitions are possible between the excited and ground states[89]. Since a number of hyperfine transitions are so close in energy, the actual observed spectrum consists of a symmetric eight line pattern. In Figure 2.12, the two outer most lines are not resolvable, and two lines on the left beyond -30 mm/sec were not measured because the velocity window was set from -30 mm/sec to

+30 mm/sec. The spectra were analysed and least-square fitted by varying the isomer shift and the internal magnetic hyperfine field. The electric quadrupole shift was set equal to zero for all fits. During the fitting procedure the relative intensities of the 18 Lorentzian lines (while constraining their linewidths to be the same) resulting from transitions between the excited and ground states were constrained to the ratio of the squares of the Clebsch-Gordan coefficients describing their transition probabilities. The fit yielded a hyperfine field value of 299.7 kGauss. Ehnholm et al reported a hyperfine field value of 317± 3 kOe at 4.2 K for bulk EuS .[89]

Figure 2.13 showed the Mössbauer absorption spectrum of EuS nanocrystals (d_{NC}~ 20 nm) recorded at different temperatures. The spectrum was recorded after seven days of exposure of the sample to the air. A partial oxidation of Eu^{2}+ to Eu^{3+} is evident from the singlet centered on 0.190 mm/sec at 90 K. As compared to the absorption spectra of bulk at 15 K, a partially collapsed hyperfine spectrum with broad lines was seen in EuS nanocrystals. This is an indication of the superparamagnetic relaxation associated with smaller nanoparticles. The low value of the hyperfine field measured at 5 K (291.4 kGauss) is also an indication of the effect of superparamagnetic relaxation. A systematic size dependent Mössbauer study is required to understand more about the superparamagnetic relaxation associated with these single domain magnetic nanoparticles.

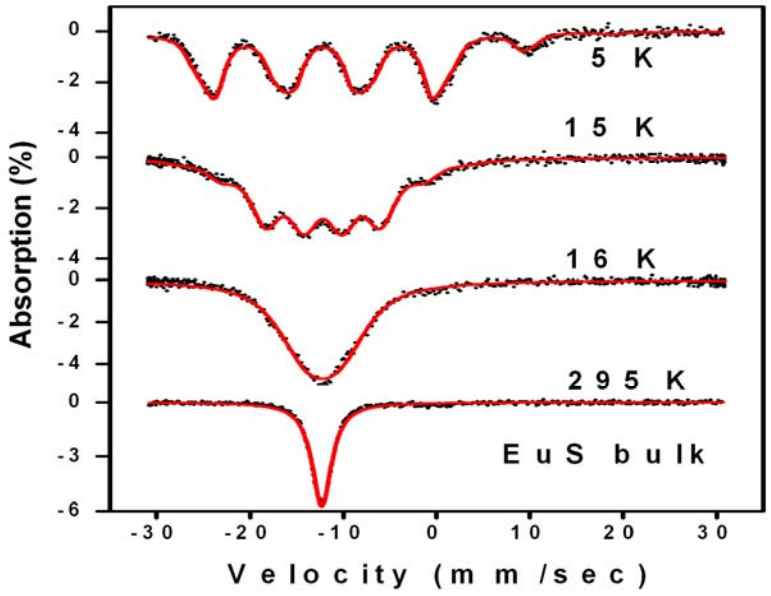

Figure 2.12: The Mössbauer absorption spectra of bulk EuS at different temperatures.

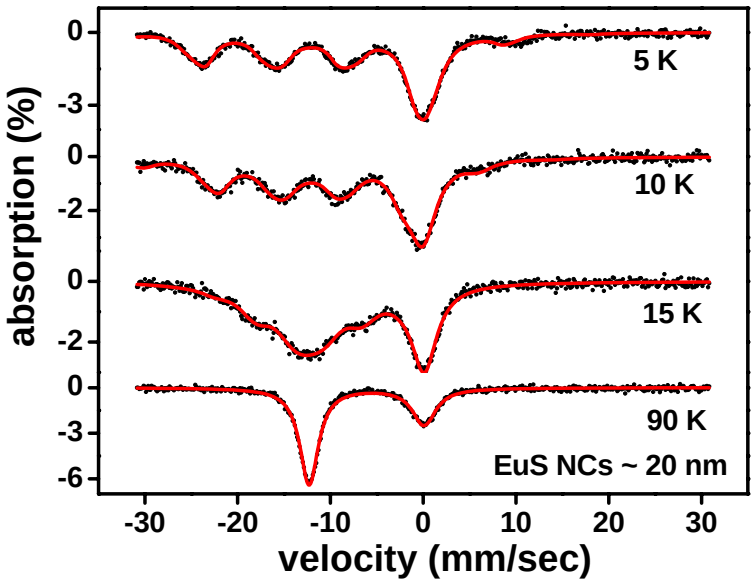

Figure 2.13: Mössbauer absorption spectra of EuS NCs (~ 20 nm) at different temperatures.

2.4 Summary

Europium sulfide NCs have been successfully synthesized by the thermolysis of a single-source precursor, europium diethyldithiocarbamate complex with 1,10-phenanthroline. This versatile technique produced EuS NCs in a wide range from 30 nm to sub-2 nm, which could be controlled by varying the temperature and time of decomposition and by selecting proper concentration of the precursor. Favourable synthetic conditions of the EuS nanomaterials were studied by TGA and DTA analysis. Particle size and crystallinity were characterized by XRD and TEM. We have demonstrated that EuS nanocrystals of ~ 20 nm exhibit optical absorption and emission spectra similar to the corresponding bulk materials. Our magnetic analysis suggested that EuS nanoparticles (d_{NC}~14 nm) undergoes a transition from the blocked state to the superparamagnetic state around 12 K. As compared to the Mössbauer absorption spectra of bulk EuS at 15 K, partially collapsed hyperfine spectra with broad lines were seen in EuS (d_{Nc}~ 20 nm) nanocrystals. This is an indication of the superparamagnetic relaxation associated with smaller nanoparticles. The surface oxidation of EuS NCs under mild conditions has been examined by Mössbauer spectroscopy. Our results showed that Eu^{2+} is partially converted to Eu^{3+} after exposure to air for seven days. Mössbauer spectroscopy proved useful in identifying variance in elemental composition. In identifying Eu^{3+} on the surface of the NCs, we were compelled to pursue another synthesis route that provided better surface passivation to reduce the surface oxidation previously observed in samples produced using the thermolysis technique.

CHAPTER III

SOLUTION-PHASE THERMOLYSIS AND STRUCTURAL CHARACTERIZATION OF COLLOIDALLY STABLE EUROPIUM SULFIDE NANOCRYSTALS

3.1 Introduction

The synthetic technique used to produce EuS nanoparticles directly influences the size, shape and surface properties of the materials, which, in turn, affects the observed optical and magnetic properties.[23, 90, 91] In the previous chapter, we discussed the synthesis of nanoscale EuS employing a technique using solvent-free, thermal decomposition of single molecular precursors. One of the primary disadvantages of these thermolysis routes is the lack of surface passivation of the NCs, which prevents rapid, spontaneous surface oxidation of the materials.[79] Among other synthetic routes, solution-phase thermolysis is the most commonly used. This technique introduces molecular precursors together with the associated surfactant molecules and liquid medium inside the reactor. By controlling the thermal conditions and chemical reactions, high quality, monodisperse nanocrystals with tunable properties, stabilized by a surface capping agent, can be produced.[79, 92] The thermal decomposition of molecular precursor in a suitable coordinating solvent is one of the most popular approaches for the production of capped nanoparticles of EuS. [9, 70] This solution thermolysis approach involves the fabrication of a single-source precursor molecule with the composition of the target material that decomposes at a relatively low temperature.[23] The majority of recent reported solution

phase thermolysis technique for EuS NC fabrication use air-stable and moisture-stable single source precursor, Eu (III) dithiocarbamate complexes.

In this chapter, we discussed the development of a one-step solvothermal technique to produce colloidally stable, monodisperse EuS NCs. The synthetic parameters, such as reaction temperature, heating time and the concentration of both precursor and surfactant, provide control over the nanocrystal sizes. The formation of single crystalline, monodisperse EuS NCs with sizes finely controlled by synthetic conditions was confirmed by high resolution transmission Electron Microscopy (HR-TEM) and powder X-ray Diffraction (XRD). Energy dispersive x-ray spectroscopy (EDS) provided elemental identification of EuS nanocrystals.

3.2 Experimental details

A two-step procedure was used to synthesize stable, highly crystalline, monodisperse europium sulfide (EuS) nanocrystals. First, europium oleate was prepared from commercially available chemicals. In the second step, the nanocrystals were synthesized by a direct liquid phase thermolysis of europium oleate and diethyldithiocarbamate in the presence of dodecanethiol and phenanthroline. This synthesis technique was developed by Dr.Dmitry Koktysh, Vanderbilt Institute of Nanoscale research.

3.2.1 Synthesis of EuS nanocrystals

Europium (III) chloride hexahydrate (99.99%), oleylamine (70%), chloroform, acetone, diethylammonium diethyldithiocarbamate (98%), 1-dodecanethiol (98%), phenanthroline (99%) were purchased from Sigma-Aldrich. Sodium Oleate (95%) was

purchased from TCI America. All chemicals were used without purification. Europium oleate was synthesized according to the previously reported procedure.[93] 2mmol of Eu (III) chloride hexahydrate, 6 mmol of sodium oleate,- 4ml ethanol,-3 ml DI water, and 7 ml hexane were mixed in a round bottom flask. A water- cooled condenser was connected to the flask to condense vapors of ethanol and hexane during the reaction. The mixture was rigorously stirred under heat at 60 °C for 4 hours. A top hexane layer containing the europium oleate was isolated by separatory funnel and washed with DI water three times. The Eu oleate complex, suspended in hexane, was a colorless, transparent, viscous solution.

Synthesis of EuS nanocrystals were carried out in a Schlenk line. Eu oleate (0.2 mmol) was mixed with diethylammonium diethyldithiocarbamate (0.6 mmol), phenanthroline (0.2 mmol), 1-dodecanethiol (1 ml) and oleylamine (6 mL) in a 25 mL three-neck, round-bottom flask. The mixture was heated to and maintained at 80 °C for 45 minutes under vacuum (degassing), purged by argon, and subsequently heated to 320 °C under constant stirring. At this temperature, nucleation of EuS NCs was initiated as evidenced by the rapid color change of the solution from yellowish to purple. The solution was held at 320 °C for a period of time that depended on the desired size of NCs; thereafter, the solution was removed from the reaction vessel with a glass syringe.[79] A sequential precipitation and centrifugation process was employed to remove the unreacted precursor from the EuS nanocrystals. 10 mL of acetone was carefully added dropwise to a hot solution of EuS NCs. The flocculated nanoparticles were isolated by centrifugation, and after removing the supernatant, were redissolved in a small amount

(~ 1 ml) of chloroform. The above purification steps were repeated twice using acetone to precipitate the EuS NCs. [79]

3.2.2 Characterization techniques

A Link ISIS Series 300 microanalysis system (Oxford Instruments) connected to a Hitachi S-4200 scanning electron microscope (SEM) was used to conduct elemental analysis of the EuS nanocrystals with X-ray energy dispersive spectroscopy (EDS). X-ray diffraction (XRD) measurements of our nanocrystals were obtained using a Scintag X1 system with a Cu $K_{\alpha 1}$ radiation (λ = 1.5406 Å). High resolution transmission electron microscopy (HR-TEM) and selected area electron diffraction (SAED) pattern images were obtained using a Philips CM20 TEM operating at 200 kV. The samples for HR-TEM investigation were prepared by dropcasting the solution of washed EuS NCs onto carbon coated copper grids and wiping off the excess liquid.

3.3 Results and discussion

To verify the elemental composition of the as-prepared nanocrystals, we performed EDS analysis of our NCs dropcasted onto a silicon substrate. The EDS measurement indicates the presence of elements Eu and S (figure 3.1). The origination of silicon peak in the EDS spectrum was due to the use of silicon substrate.

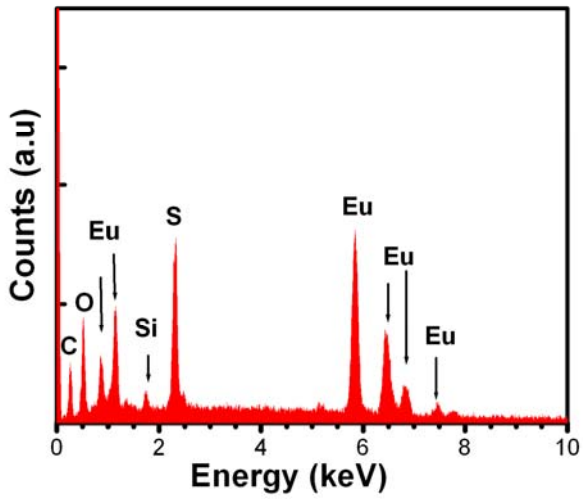

Figure 3.1: Energy dispersive spectrum of (EDS) of EuS nanocrystals showing europium and sulphur signature.

We have used both TEM and XRD to determine the size and structure of the EuS NCs. The typical X-ray diffraction patterns of the nanoparticles were shown in Figure 3.2. The diffraction peaks were indexed and juxtaposed with the JCPDS file for bulk EuS (JCPDS, pdf file 26-1419). EuS possesses rock salt crystallinity with a lattice constant of 0.5968 nm. The intense broadening of the XRD peaks was caused by the small particle sizes. The average size of EuS nanocrystal can be calculated using Scherer equation;

$$L = \frac{K\lambda}{\beta \cos(\theta)} \; ; \qquad (3.1)$$

where K is the Scherer constant, λ is the wavelength of radiation, β is the full width at half maximum and θ is the Bragg angle. We attempted to identify the size of

our nanocrystal with Scherrer analysis. The Scherrer analysis yielded sizes of ~ 6.2 nm, ~11.9 nm and ~ 27.4 nm, which correspond to 5 nm, 10 nm and 25 nm, as defined by TEM. No additional XRD peaks were observed due to impurities or surface oxidation.

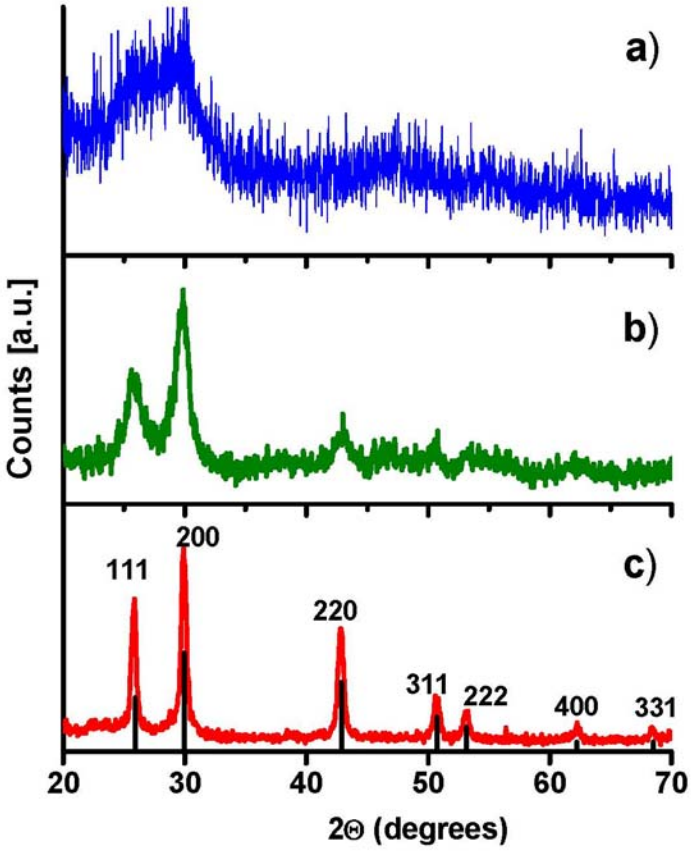

Figure 3.2: Powder X-ray diffraction pattern of EuS nanocrystals (a) d_{NC} ~ 5 nm (b) ~ 10 nm, and (c) ~ 25 nm. Bragg diffraction peaks from bulk EuS (JCPDS 26-1419) are presented for comparison.[79]

Selected area electron diffraction (SAED) patterns of EuS NCs (d_{NC} ~ 20 nm) are presented in (Figure 3.3.(a)). The measured ring diameters match the values for the lattice planes of fcc EuS. The high crystallinity of the samples was further confirmed by

the clear lattice fringes in the HR-TEM image (Figure. 3.3 (b)). The measured lattice parameter 0.295 nm can be assigned to a lattice spacing (200) for EuS.

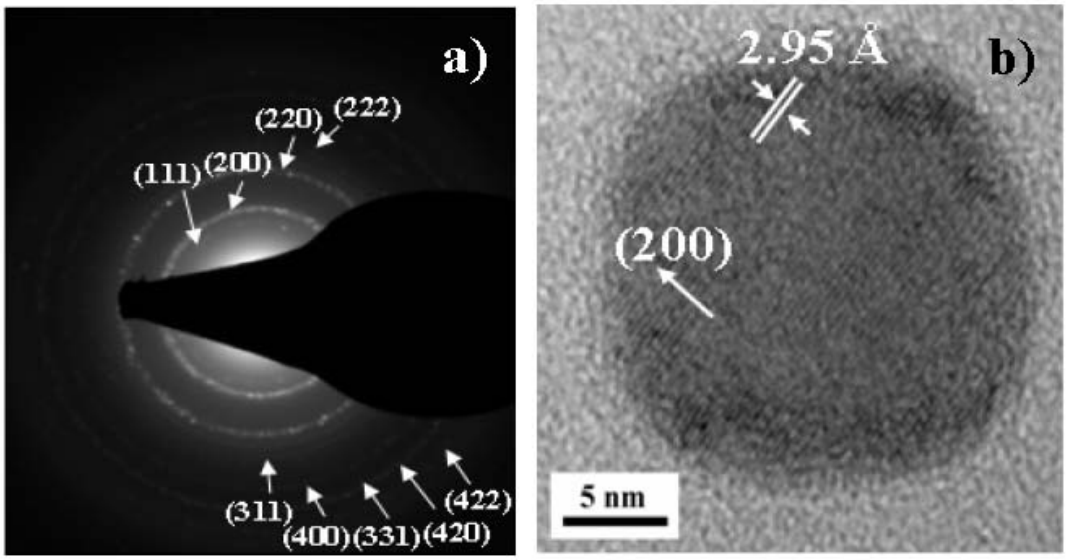

Figure 3.3: (a) Selected area electron diffraction pattern and (b) HR-TEM image showing diffraction fringes corresponding to the (2 0 0) atomic planes of EuS nanocrystals (d_{NC}~20 nm).[79]

Figure 3.4 & 3.5 displayed the HRTEM images of colloidally stable, monodisperse EuS NCs obtained from the solvothermal synthesis. The HR-TEM revealed a predominance of monodisperse spherically-shaped nanoparticles with sizes below 20 nm (Figure 3.4 (a-d) and Figure 3.5 a). The shape of particles was predominantly rectangular when the particles were larger than 25 nm (Figure 3.5 (b)).[79, 80] The particle's sizes can be controlled in a wide range with the smallest one down to 2.5 nm. The corresponding size histograms are given in insets of Figure 3.4.[79]

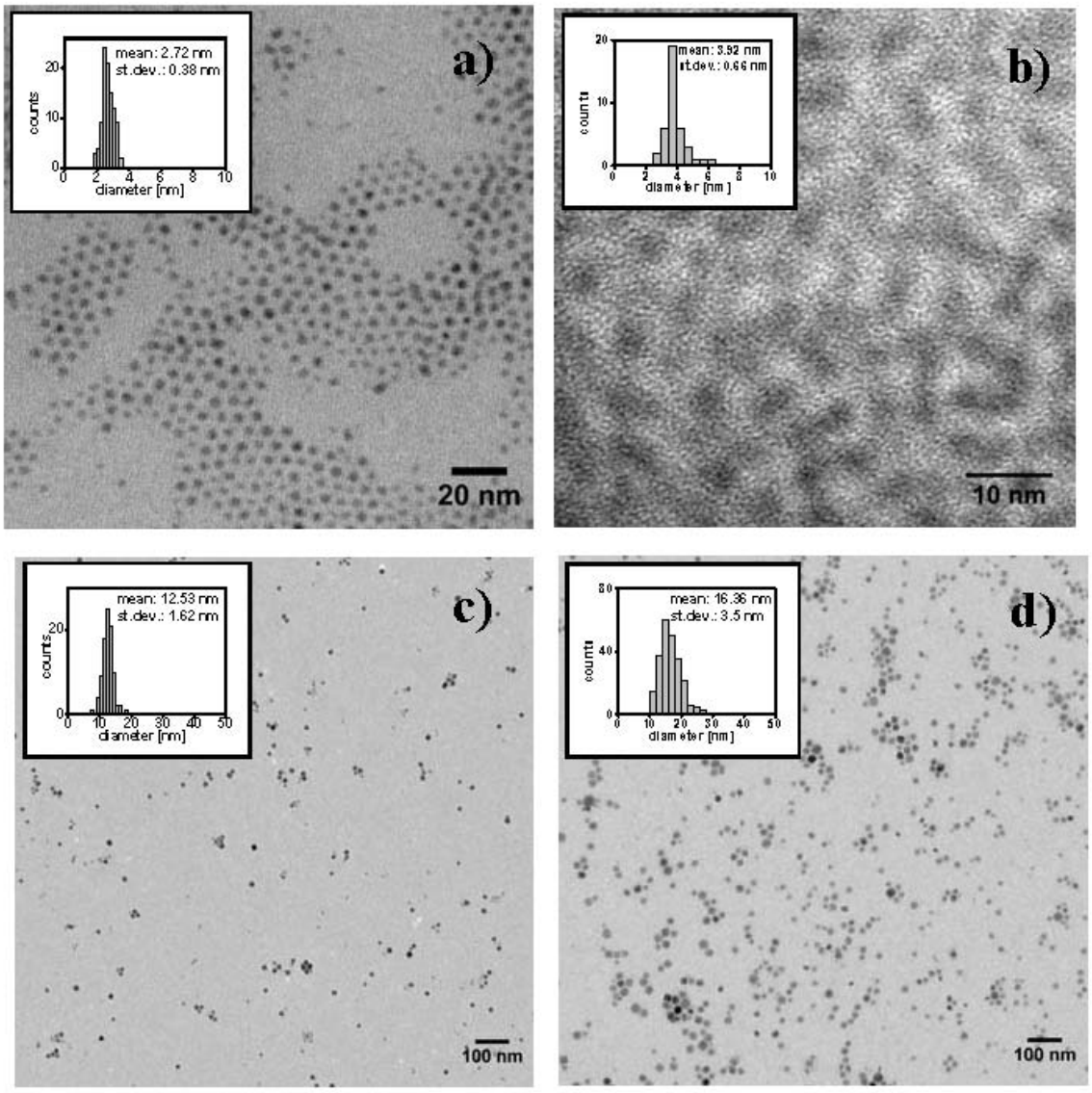

Figure 3.4: HR-TEM images of EuS nanocrystals (a) d_{NC} ~ 2.72 nm (b) d_{NC} ~ 3.92 nm (c) d_{NC} ~12.53 nm and (d) d_{NC} ~ 16.36 nm, grown at different synthetic conditions. Insets: EuS particle size histograms.[79]

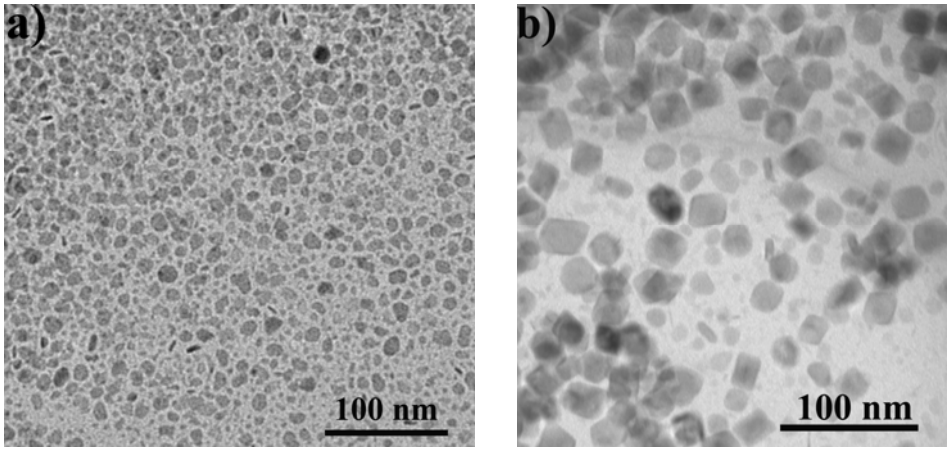

Figure 3.5: TEM image of (a) ~ 10.6 nm EuS nanocrystals and (b) rectangular shaped EuS nanocrystals. [79]

Eu(II)S NCs were formed from Eu(III) oleate and diethylammonium diethyldithiocarbamate through the accelerated reduction of Eu(III) by diethyldithiocarbamate and the subsequent nucleation of EuS crystallites from a single source precursor.[8, 75, 94] The size tuning of EuS NCs was achieved by high degree of control over nucleation and growth stages and low degree of Ostwald ripening. This precise control of particle size was carried out by use of different growth times and different concentrations of phenanthroline and dodecanethiol. Increasing the reaction time prior to quenching, decreasing the concentration of dodecanethiol, and increasing of the concentration of phenanthroline facilitated the growth of larger NCs. Changing the molar ratio of europium oleate: phenanthroline from 1:0 to 1:1 led to the formation of 2.7 nm and 12.5 nm EuS NCs respectively (Figure 3.4 (a,c)). Europium oleate: phenanthroline ratio of 1:2 produced 16.4 EuS NCs (Figure 3.4.d)). Changing the concentration of dodecanethiol from 1 mL to 0.2 mL led to the formation of 2.7 nm and

4 nm size EuS NCs, correspondently (Figure 3.4 (a,b)). Dodecanethiol served as the capping agent to suppress oxidation of EuS NCs.[79]

3.4 Summary

A novel one-step solvothermal synthesis technique to produce colloidally stable, monodisperse europium sulfide NCs was reported. EuS NCs were synthesized by the direct liquid phase thermolysis of europium oleate and diethyldithiocarbamate in the presence of dodecanethiol and phenanthroline. Dodecanethiol was used as surfactant to prevent nanoparticle agglomeration, stabilize particle growth and also served as the capping agent to prevent EuS NCs from oxidation. By varying the synthetic parameters such as reaction temperature, reaction time and the concentration of both precursor and surfactant, EuS nanoparticles of different sizes (d_{NC}~ 2.5 to 25 nm) were obtained. Particle size and crystallinity were characterized by XRD and TEM. Elemental analysis of EuS NCs by EDS suggested the high purity of EuS nanocrystals. It is expected that the size controlled and surface protected EuS NCs would be a promising material for optical isolators, optical switches and optical memories.

CHAPTER IV

SIZE-DEPENDENT OPTICAL & MAGNETIC PROPERTIES OF EUROPIUM SULFIDE NANOCRYSTALS

4.1 Introduction

The ability to tune synthetically the materials properties in terms of size, shape, and composition of europium sulfide nanocrystals allows for better control in enhancing the optical, magnetic, and magneto-optical properties when compared to their bulk counterparts.[8, 23] Such novel properties provide a wide range of potential applications for these materials as ferromagnetic semiconductors, bioimaging reagents, magneto-optic and luminescent materials [9, 13, 18]. Exploring EuS nanomaterials, whose bulk form can be described by a classic Heisenberg ferromagnetic model, can also allow us to understand the influence of particle size on the magnetic exchange mechanisms and magneto-optical coupling mechanisms.[20] A blue shift in the optical absorption spectrum, size dependent luminescence, enhanced Verdet constant, and decreased ferromagnetic ordering temperature have been observed with decreasing particle size.[22-24] The change in the properties of nanocrystals is mainly driven by two factors: the increase in the surface to volume ratio and change in the electronic structure of the material due to quantum confinement effects. Currently, researchers are investigating the magnetic and luminescent properties of EuS nanocrystals with changes in particle size.[9, 13, 23] However, literature on the preparation of single domain EuS nanocrystals and a systematic study on magnetism in EuS NCs, so far, is limited.[9, 23] Also, it is worth noting that there are no

reports on the temperature dependent luminescence study of EuS nanocrystals using the aforementioned synthesis techniques.[22]

In this chapter, we investigated the role of particle size on the optical and magnetic properties of EuS nanocrystals. Absorption and temperature dependent photoluminescence characteristics of these nanocrystals are described. Quantum confinement behavior in EuS NCs is observed with continuous blue-shifts in the absorption and luminescence spectra as the crystal size is reduced. The effect of particle size on the ferromagnetic ordering temperature in EuS nanocrystals is also discussed. In addition, we review the effect of surface oxidation on the optical and magnetic characteristics of smaller EuS nanocrystals.

4.2 Experimental details

4.2.1 Materials and methods

The colloidally stable, monodisperse EuS nanocrystals (d_{NC}~ 2.5 nm to 25 nm), capped with dodecanethiol, were synthesized via the synthesis technique described in chapter III (section 3.2.1). The nanocrystals were cleaned in acetone using a typical precipitation-centrifugation procedure, described in Chapter III (Section 3.2.1). The EuS NCs were suspended in chloroform for our optical absorption study. The NCs solutions, suspended in hexane were drop casted onto a barium fluoride pellet for luminescence measurement. Powdered EuS NCs of ~ 10 mg were placed inside a polypropylene powder holder (capsule) for magnetic measurements.

4.2.2 Characterization techniques

UV-Vis-NIR absorption spectra of EuS Nanocrystal solutions in chloroform were measured at room temperature with a Cary 5000 UV-Vis-NIR spectrometer (Varian). The photoluminescence measurements were performed at various temperatures (from 6 K-300 K) using HeCd laser (40 mw at 325 nm) as the excitation source. Magnetic measurements were performed on a Vibrating sample magnetometer (VSM). The system consist of a 17 Tesla superconducting magnet and a VSM linear motor. Control of the sample temperature is regulated with a combination of liquid nitrogen and liquid helium. Measurements of magnetization as a function of temperature were performed for field-cooled samples, then increasing the temperature from 2 K to 300 K in a field of 1000 Oe. Hysteresis curves were measured at various temperatures from 2 K-30 K.

4.3 Results and discussion

4.3.1 Absorption and luminescence

The relationship between particle size and electronic properties (band gap energy) in semiconductor nanocrystals has been extensively studied by several research groups.[95, 96] Particles whose size becomes comparable to the bulk exciton radius, a_B, are observed to exhibit quantum confinement effects.[23] Researchers have defined three size regimes for nanocrystals, a strong confinement regime, in which nanocrystals have radii of less than a_B ($r << a_B$), an intermediate regime ($r \sim a_B$) and a weak confinement regime, in which nanocrystals have radii of greater than a_B ($r >> a_B$).

The bulk exciton Bohr radius is given by,

$$a_B = \frac{m_0 \varepsilon a_0}{\mu} \tag{4.1}$$

where m_0 is the free electron mass, a_0 is the hydrogen atom Bohr radius (~ 0.53Å), ε is the dielectric constant of the material and μ is the reduced mass of exciton.[97]

$$\mu = \frac{m_e^* m_h^*}{m_e^* + m_h^*} \tag{4.2}$$

where m_e^* and m_h^* are the effective mass of electron and hole respectively. [23]

Using eq. 4.1 and assuming the hole effective mass much larger than the electron effective mass [23], we calculated the exciton Bohr radius for EuS (effective mass of $0.3m_0$ [82] and a dielectric constant [83] of 10.2). The calculated EuS Bohr exciton radius was ~ 1.8 nm. Our result, 1.8 nm, suggests that our smallest nanoparticle (d_{NC} ~ 2.5 nm) falls in the strong confinement regime, d_{NC} ~ 5 nm falls in the intermediate regime, and EuS nanoparticles (d_{NC} ~ 12 nm) falls in the weak confinement regime.

According to Brus equation, an analytical approximation for the first excited electronic state is given by[96, 98]

$$E = E_g + \frac{\hbar^2 \pi^2}{2\mu r^2} - \frac{1.8e^2}{4\pi\varepsilon\varepsilon_0 r} + \text{polarization energy} \tag{4.3}$$

In this equation E_g is the band gap energy of the bulk semiconductor, ħ is the reduced Planck constant, e is the elementary charge and ε_0 is the vacuum permittivity. The second term describes the energy due to quantum localization and the third term describes the energy due to Coulomb attraction between electron and hole. As the

polarization term is small compared to the energy due to quantum localization and Coulomb energies, a good understanding of the lowest-energy excitonic state may be made by omitting this term. The Coulomb term shifts E to lower energy as 1/r, while the quantum localization term shift E to higher energy as $1/r^2$.

In europium chalcogenide, there are two major peaks corresponding to different types of electronics transitions. The low-energy absorption peak corresponds to a $4f^7(^8S_{7/2}) \rightarrow 4f^6(^7f_J)5d(t_{2g})$ transition whereas the high-energy absorption region is governed by an electronic charge transfer from anion to cation, and by transitions from the 4f levels to the $5d(e_g)$ states.[3] Detailed explanation of the energy level scheme of europium chalcogenide is provided in section 1.4.1. Guntherodt et al.[3] performed transmission measurements on EuS thin films at 300 K and the corresponding spectra were shown in figure 4.1. The lowest absorption peak is centered at 2.4 eV (~ 517 nm) and the high-energy peak is around 4.6 eV (~ 270 nm). The onset of the first absorption peak is at 1.65 eV, which corresponds to the band gap energy of bulk EuS.[3, 23]

We measured the room temperature optical absorption spectra of EuS NCs solutions, suspended in chloroform (figure 4.2& 4.3). The absorption spectra of EuS nanoparticles of ~ 25 nm diameter showed two major peaks , the first peak centered at ~ 2.42 eV (~510 nm) and the second peak around 4.51 eV (~ 274 nm).

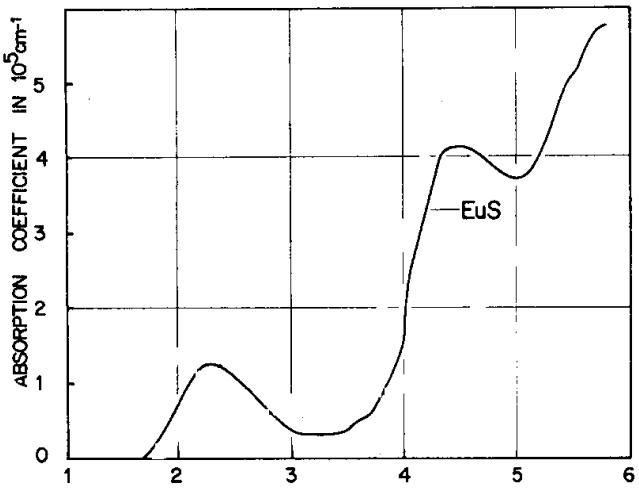

Figure 4.1: UV-Visible spectra for EuS bulk (after reference[3]).

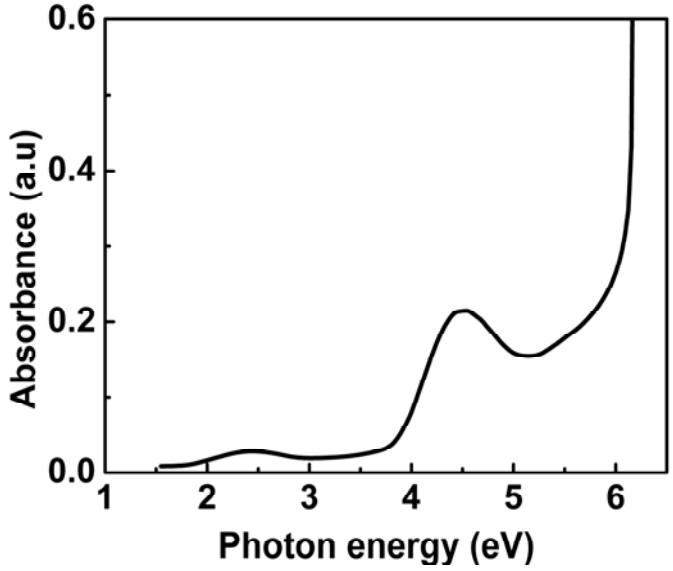

Figure 4.2: UV-Visible spectra for EuS nanoparticles of ~ 25 nm

Kataoka et.al [14] reported a shift in the absorption peak wavelength from 540 nm to 515 nm for nanoparticles ranging in size from 14 nm to 7 nm, and identified this as the $4f^7(^8S_{7/2}) \rightarrow 4f^6(^7f_J)5d(t_{2g})$ transition. A similar blue shift of the absorption bands

accompanied by the decrease of particle size was reported by Regulacio et.al.[23] We have also observed a shift from 510 nm for 25 nm EuS NCs to 490 nm for 2.5 nm EuS NCs, which can be explained by weak and strong quantum confinement effects.

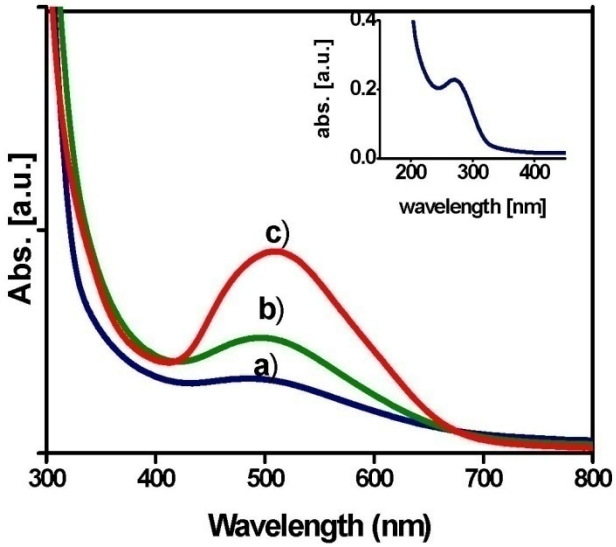

Figure 4.3: Optical absorption spectra of (a) 2.5 nm, (b) 5 nm, and (c) 12 nm EuS nanocrystals in chloroform. Inset: high energy absorption peak of 2.5 nm EuS NCs.[79]

The luminescence spectra of EuS nanocrystals (d_{NC} ~ 4 nm and 12 nm) were measured at 300 K, 100 K, 50 K, 10 K and 6 K, respectively. Figure 4.4 showed the room temperature photoluminescence spectra of 4nm and 12 nm EuS nanocrystals. The emission band is attributed to the transition of $4f^6(^7f_J)5d^1(t_{2g}) - 4f^7$ of Eu^{2+}.[3, 22] A blue shift in the luminescence peak energy corresponding to the decrease of EuS NCs size was observed. This shift is likely due to a combination of surface strain and quantum confinement effects on the *f* to *d* transitions of Eu^{2+}.[13]

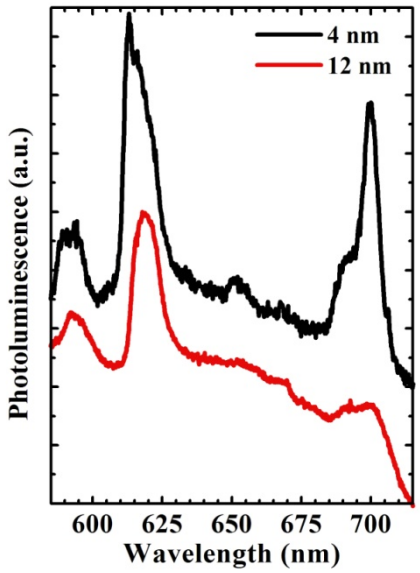

Figure 4.4: Room temperature photoluminescence spectra of 4 nm (a) and 12 nm (b) EuS nanocrystals.[79]

Figures 4.5 and 4.6 showed the temperature dependent photoluminescence spectra of ~ 12 nm and ~ 4 nm EuS nanocrystals. For both particle sizes, we observed increases in emission intensity with a decrease in temperature. The photoluminescence spectra of 4 nm EuS nanocrystals exhibit pronounced fine structures in the low temperature luminescence spectra, which were not observed in the 12 nm EuS spectra. This is likely due to the increase in surface to volume ratio which allows for more dominant effects from the oxidative surface states.

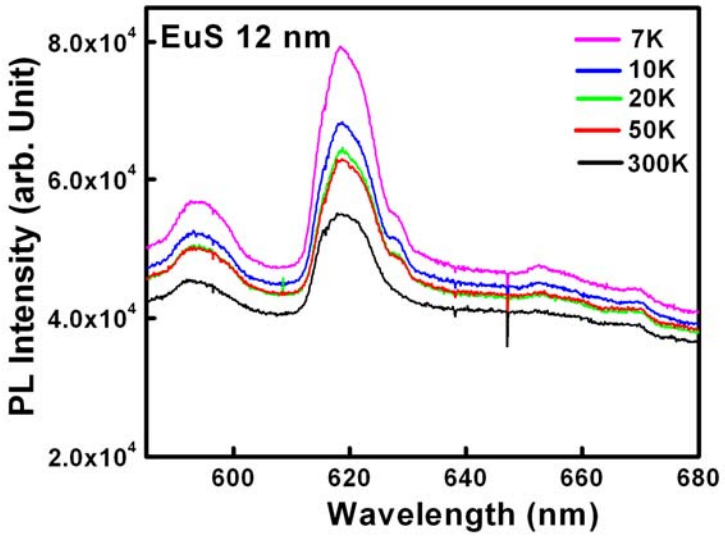

Figure 4.5: Temperature dependent photoluminescence spectra of ~ 12 nm EuS nanocrystals.

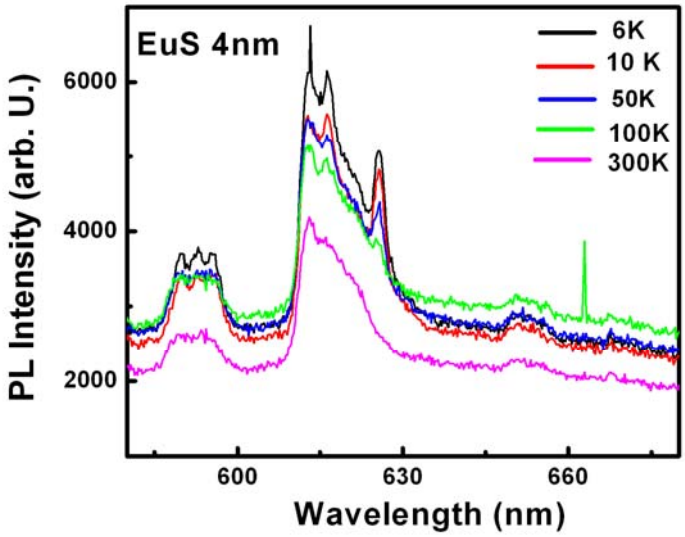

Figure 4.6. Temperature dependent photoluminescence spectra of ~ 4 nm EuS nanocrystals.

4.3.2 Size-dependent Magnetic properties

Since europium chalcogenides are classical Heisenberg magnets, the theory to explain the exchange mechanisms is well defined. For europium chalcogenides, the approximate relationship between Curie temperature T_c and exchange integrals J_1 (ferromagnetic coupling) and J_2 (antiferromagnetic coupling) is given by the equation [21, 23, 68],

$$k_B T_c = \frac{2}{3} S(S+1)\left[Z_1 J_1 + Z_2 J_2\right] \tag{4.4}$$

where Z_1 is the number of nearest neighbors, Z_2 is the number of next-nearest neighbors, and S is the total spin quantum number. Also, the exchange parameter J_1 is related to the electronic band gap [99],

$$J_1 = \frac{Ab^2}{E_g^2} \tag{4.5}$$

A is a measure of the extent of delocalization of f electrons in the conduction band, b is a measure of the orbital overlap, and E_g is the band gap between the f and d levels. The size dependent effect on the magnetic properties of europium chalcogenides can be interpreted using Equation 4.4 and 4.5.

Several researchers are investigating the magnetic properties of EuS nanocrystals as a function of particle size.[9, 23] The relationship between particle size and Curie temperature of EuS NCs between 7.2 nm and 4.9 nm was studied by Regulacio et al [23]. In my research investigation, we reported the magnetic studies of EuS nanocrystals

(d_{NC} ~ 4 nm, 10.6 nm and 18 nm), synthesized using the aforementioned synthesis technique (section 3.2.1).

Magnetic measurements of EuS nanocrystals were performed using a Vibration sample magnetometer. The magnetization measurements were conducted at a constant field of 1000 Oe with temperatures ranging from 2 K to 30 K. To get a better understanding of the magnetic interactions, we calculated the magnetic susceptibility per EuS nanocrystal mass. The temperature dependent magnetic susceptibility of EuS NCs under field cooled condition is shown in figure 4.7. For the 18 nm and 10.6 nm EuS samples, the magnetic susceptibility shows a sharp increase at low temperatures, near T_c ,similar to that observed for bulk EuS (~ 17 K).[18] Also evident from the magnetic susceptibility curve, the ferromagnetic ordering temperature associated with 4 nm EuS NCs was substantially lower than that of 10.6 nm NCs. Our estimated Bohr exciton radius (~1.8 nm, see section 4.3.1) suggests that the 4 nm EuS nanocrystals resides in the intermediate confinement regime. The reduced ferromagnetic ordering temperature of 4 nm EuS sample was expected to be due the quantum confinement effect. As compared to the 18 nm EuS sample, a high susceptibility per EuS NCs mass was observed for our 14 nm sample. We expect this to be due the inaccuracy in the mass measurement.

The temperature dependence of χT for EuS nanocrystal (d_{NC} ~ 4 nm, 10.6 nm and 18 nm) is shown in Figure 4.7. For all samples, a rapid rise in χT as the temperature dropped below ~25 K was observed, which indicated the ferromagnetic interactions between Eu^{2+} ions. The value of χT reaches a maximum and then rapidly decreased below T_c as a result of saturation of the magnetic moments. The temperature at which

moment saturation occurs continuously decreased from ~14.9 K (d_{NC} ~18 nm) to ~ 5.9 K (d_{NC} ~ 4 nm). Zhao et.al [9] reported a quasi-ferrimagnetic behavior due to surface oxidation (anomalous magnetic phenomenon of slight increase of χT at high temperatures) for EuS NCs ($d_{NC} \leq 14$ nm). A similar phenomenon was observed for our 4 nm EuS anocrystals.

Figure 4.9 illustrates the magnetization hysteresis curves of EuS sample (d_{NC} ~ 4 nm, 10.6 nm and 18 nm) at 2 K for a cycling field of ±3 T. A pronounced saturation magnetization was observed for the 18nm and 10.6 nm EuS samples. As noted earlier, a direct comparison of the saturation magnetization of 18 nm and 10.6 nm EuS nanocrystals was hampered by inaccuracies in mass. However, for 4nm EuS NCs, moment saturation was not observed at fields up to 3 Tesla.

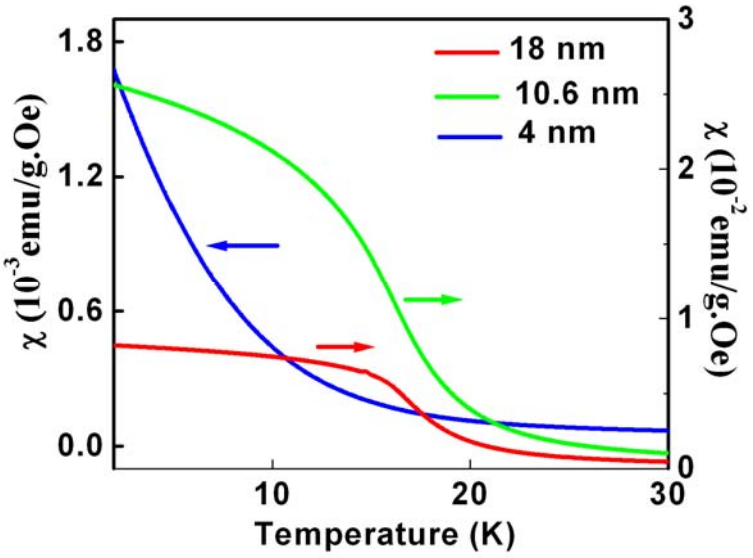

Figure 4.7: Temperature dependence of magnetic susceptibility (χ) measured after field cooled magnetization using 1000 Oe.

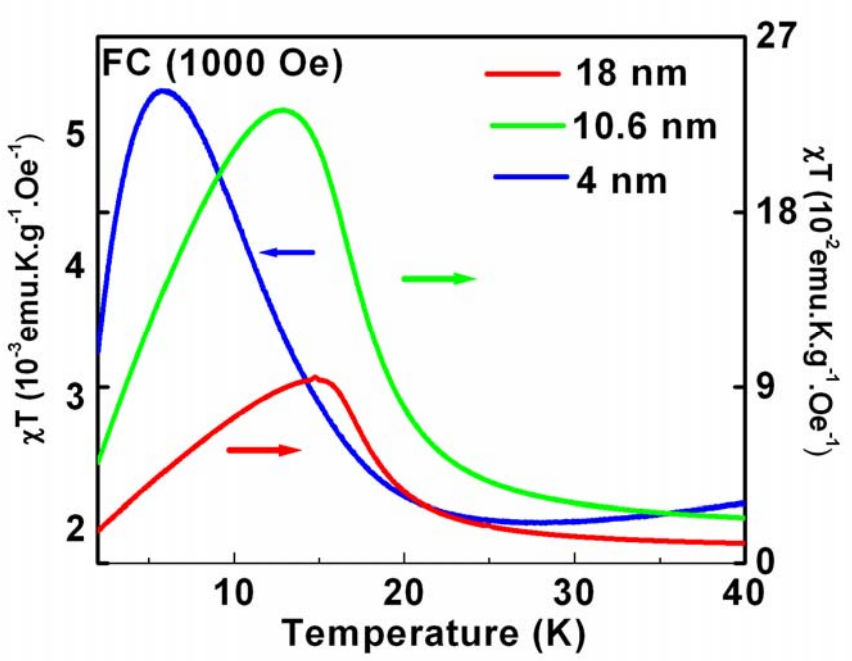

Figure 4.8: Temperature dependence of χT of EuS nanocrystals

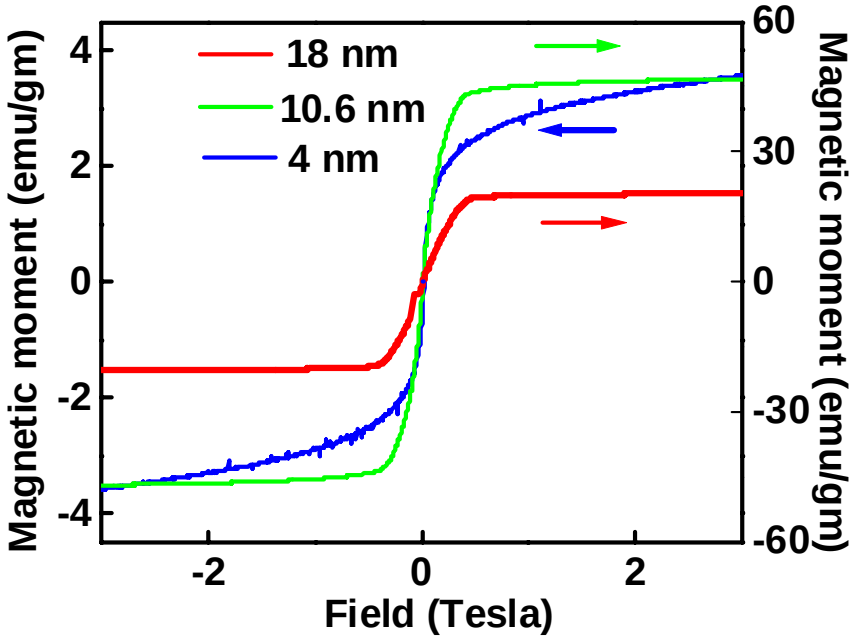

Figure4.9:Field dependence of magnetization (M) measured at 2 K for Eu nanocrystals.

4.4 Summary

The effects of particle size on the optical and magnetic properties of EuS nanocrystals were investigated. Quantum confinement behavior in EuS NCs was observed with continuous blue-shifts in the absorption and luminescence spectra as the crystal size is reduced. The ferromagnetic ordering temperature was observed to be strongly dependent on the size of EuS nanocrystals.

CHAPTER V

STRUCTURAL & MAGNETIC ANALYSIS OF NANOCRYSTALLINE LEAD EUROPIUM SULFIDE, A DILUTE MAGNETIC SEMICONDUCTOR

5.1 Introduction

Lead-based dilute magnetic semiconducting (DMS) materials, alloyed with rare earths, have been investigated for a variety of optical, magnetic, and electronic applications.[28, 29] For example, increased europium content in lead based DMS alloys changes the energy band gap of the material and produces variations in the lattice constant and refractive index of the material. Such characteristics make these materials suitable for use in thin film Bragg mirrors, lasers, wavelength converters, and photodiodes for the IR range.[30-33] The magnetic properties of lead-based DMS materials containing europium ions have been investigated over the past two decades, though not as widely as those of the transition-metal-doped II-VI and IV-VI DMS [7-13].[100-102] Recently, there has been considerable interest in these materials because of their possible application in spintronics.[34, 103, 104] Braunstein et al measured the magnetization and magnetic susceptibility of molecular-beam-epitaxy grown $Pb_{1-x}Eu_xTe$ and observed a weak antiferromagnetic coupling among the Eu ions.[102] The detailed investigation of the magnetic properties of Bridgman-grown $Pb_{1-x}Mn_xTe$ and $Pb_{1-x}Eu_xTe$ samples by Gorska et al indicated a small ($\frac{J}{k_B} < 1\,\mathrm{K}$) antiferromagnetic exchange interaction among the magnetic ions. The absolute value of the exchange constant of $Pb_{1-x}Eu_xTe$, was

approximately three times smaller than that of $Pb_{1-x}Mn_xTe$ and decreased with the increasing Eu content .[62, 101, 105] These results were well explained by the model of superexchange interaction between the nearest neighbors (NN) via an anion.[34, 101] Bindilatti et al performed magnetization measurements on Bridgman grown $Pb_{1-x}Eu_xS$ single crystals ($x < 0.06$) at mK temperatures and found a value of $\frac{J}{k_B}$ = -0.228 ± 0.007 K for the dominant antiferromagnetic exchange constant.[35] Computer simulations identify this J as the nearest neighbor exchange constant J_1. The exchange constant in the corresponding Eu chalcogenide (EuS) is very different. For EuS, the dominant ferromagnetic indirect exchange is J_1 while J_2 is antiferromagnetic. The mechanism of exchange interaction among europium ions in lead based DMSs is still not well understood.

Among the lead europium chalcogenide compounds [$Pb_{1-x}Eu_xX$ (X= S, Se, Te)], lead europium sulfide ($Pb_{1-x}Eu_xS$) have been discovered to form a completely miscible alloy system.[36] Lead sulfide (PbS) and europium sulfide (EuS) both crystallize in the rock-salt crystal structure with only a 0.5% lattice mismatch between the two materials. Further, $Pb_{1-x}Eu_xS$ has exhibited energy band gaps tunable over a wide range. Bulk, epitaxial films of $Pb_{1-x}Eu_xS$ were prepared for the first time by Ishida et al using hot wall epitaxy.[36] Subsequent investigations of single crystal $Pb_{1-x}Eu_xS$ employed other fabrication approaches, such as the Bridgman technique and molecular beam epitaxy.[31, 106] Since the initial work of Ishida [33, 36] however, nanocrystalline forms of $Pb_{1-x}Eu_xS$ materials have yet to be reported.

Generally, ternary nanocrystals are synthesized via solid-state reactions, solution-phase thermolysis, or hot-injection techniques[69, 107].[108] The thermal decomposition of single molecular precursors has been proven to be an effective method to synthesize nanoscale metal alloys and metallic chalcogenides.[69, 107] Although the use of a single precursor source is convenient, this method is limited for alloys because of the availability of workable precursors and the associated laborious synthesis procedures.[108] To synthesize Pb_xEu_yS nanocrystals, we used a facile thermolysis technique that employed mixed precursors of Pb(II) diethyldithiocarbamate complex with 1,10-phenanthroline (hereafter referred to as $Pb(ddtc)_2Phen$) and Eu-diethyldithiocarbamate complex with 1,10-phenanthroline (hereafter referred to as $Eu(ddtc)_2Phen$).

In this chapter, we report the first synthesis and characterization of nanocrystalline alloyed lead europium sulfide, a potentially important dilute magnetic semiconductor. The thermolysis of mixed precursors has been adapted for the formation of homogeneous alloyed nanocrystals. Energy dispersive spectroscopy provided the atomic composition for Pb_xEu_yS nanocrystals, which we juxtaposed with the ratio of the starting precursors. Unlike previous research on its bulk forms, we discovered both that nanocrystalline lead europium sulfide alloy astochiometrically and that this phenomenon changes as europium content increases. Thus, we assign the stochiometry to be represented as Pb_xEu_yS. X-ray diffraction and magnetization measurements of the ternary nanocrystals provided convincing evidence that no phase separation occurs for europium concentrations of up to $y = 0.15$. Concentration dependence of the exchange interaction in Pb_xEu_yS nanocrystals was investigated. We observed that the exchange

constant $\frac{J}{k_B}$ is negative and its magnitude decreases with increasing Eu content(y), but the pair exchange constant $\frac{J_p}{k_B}$ was weakly dependent of y.

5.2 Experimental details

Mixed precursors of a [Eu(ddtc)$_2$Phen] and [Pb(ddtc)$_2$Phen] have been used in a facile thermolysis technique to produce lead europium sulfide (Pb_xEu_yS) nanocrystals.

5.2.1 Precursor preparation

1,10-phenanthroline (≥99%), methanol (anhydrous 99.8%), europium (II) chloride (99.99% trace metals basis), and diethyldithiocarbamic acid diethylammonium salt (97%) were purchased from Sigma Aldrich. Lead (II) acetate trihydrate (Puratronic®, 99.995% metals basis) was purchased from Alfa Aesar. Methyl sulfoxide (99.7+%) was purchased from Fisher Scientific. All the chemicals were used as-received without further purification.

Pb(ddtc)$_2$Phen was prepared from lead acetate in a way similar to a recently reported procedure.[109] All synthetic steps were conducted at room temperature using anhydrous solvents. A 1 mM methanolic solution of 1, 10-phenanthroline was added under vigorous stirring to a 1 mM methanolic solution of lead acetate. Thereafter, 1 mM of diethylammonium diethyldithiocarbamate were added into the reaction mixture, producing a pale yellow precipitate. The resulting precipitate was isolated by centrifugation, washed three times with methanol, and dried under vacuum.

The single molecular precursor $Eu(ddtc)_2Phen$ was prepared using the following method.[69, 70] All synthetic steps were conducted inside a dry glove box under nitrogen atmosphere and at room temperature using anhydrous solvents. Under a nitrogen atmosphere and with vigorous stirring, a 1mM methanolic solution of 1, 10 phenanthroline was added to a 1mM methanolic solution of europium (II) chloride followed by the addition of a methanolic solution of 2mM of diethyl ammonium diethyldithiocarbamate producing a lustrous, dark-grey precipitate. The EuS precursor precipitate was isolated by centrifugation, washed three times with methanol and dried under vacuum.

A certain molar ratio of lead and europium sulfide precursors were dissolved in dimethyl sulfoxide (DMSO), under vigorous stirring. The resulting precursor for ternary NCs was dried initially using a rotary evaporator and then an applied vacuum.

5.2.2 Solid state thermolysis

For the synthesis of Pb_xEu_yS nanocrystals, the mixed precursor was transferred to a porcelain boat and was inserted into a quartz tube in a horizontal tube furnace (Thermolyne #F21135, Barnstead International) for a time-sensitive mass reduction step under a stream of dry, ultra pure nitrogen for 1h at 700 ºC. Thereafter, the resultant solid was cooled gradually to room temperature. Adjustment to the thermolysis time, temperature, and precursor concentration yielded Pb_xEu_yS nanocrystals of a variety of sizes, all of which were devoid of surface ligand molecules. The [Pb]/ [Eu] composition in the alloyed material can be adjusted according to the ratio of precursor used. In this study, we synthesized Pb_xEu_yS nanocrystals with the following Pb/ Eu molar ratios:

10:0.5, 10:1 and 10:2. The resultant Pb_xEu_yS nanocrystals were washed three times by methanol to remove any unreacted precursor. We synthesized PbS and EuS nanocrystals from their respective precursor complexes such as $[Pb(ddtc)_2Phen]$ and $[Eu(ddtc)_2Phen]$ using the above solid state thermolysis technique.

5.2.3 Characterization techniques

A TGA-1000 (Scientific Systems Inc.) thermogravimetric analysis (TGA) system was employed to determine the thermal decomposition of the precursor complexes. A small amount (~ 10 mg) of the precursor was placed in a platinum weighing pan and was heated across a temperature range from 25 ºC up to 800 ºC at a heating rate of 20 ºC min^{-1} under nitrogen atmosphere. Fourier transform infrared (FT-IR) spectroscopy was used to investigate the molecular bondings of the precursor complexes. Infrared spectra of the precursors were measured in the range 500-4000cm^{-1} as pressed pellets in KBr on a Thermo-Nicolet 300 FT-IR spectrometer. Energy dispersive spectroscopy (EDS) measurements were performed by Dr.Saad Hasan (former graduate student,Dickerson group) using a Hitachi S-4200 Scanning Electron Microscope operating at 20 kV with a Link ISIS Series 300 microanalysis system (Oxford Instruments). Quantitative analysis using the INCA software yielded the atomic percentages in each sample. These values were used to determine the stoichiometry of the different binary and ternary compositions. The binary PbS, EuS and the ternary Pb_xEu_yS samples were washed five times intensively by methanol to remove any unreacted precursor. Methanolic solutions of the binary and ternary nanocrystals were spun cast on a Cu substrate at 400 rpm for 60 sec for EDS analysis. X-ray diffraction **(**XRD) measurements of our nanocrystals were

obtained using a Scintag X1 system with a Cu K_α X-ray source. Thin films of the as-synthesized nanocrystals were dropcasted on a silicon plate <511> for XRD measurements. The size and size distribution of the nanocrystals were investigated using a Philips CM 20 transmission electron microscope (TEM) operating at 200 KV. The TEM samples were prepared by adding a drop of cleaned nanocrystals, dispersed in methanol, onto a holey carbon films mounted on TEM specimen grids (Ted-Pella). Vibrating sample magnetometry (VSM), conducted with a Quantum Design PPMS system, provided characterization of the magnetization as a function of temperature, m(T), and the magnetization as a function of applied field, m(H).

5.3 Results and discussion

5.3.1 Precursor characterization

Fourier transform infrared spectroscopy (FT-IR) was used to investigate the molecular bondings of the precursor complexes (Figure 5.1). The IR spectra of $Eu(ddtc)_2Phen$ complex displayed characteristic peaks from the 1,10-phenanthroline ligand at 1620 cm^{-1},1589 cm^{-1},1572 cm^{-1} and 1516cm^{-1} attributed to the skeleton vibration mode of the benzene ring in addition to the peaks at 843 cm^{-1} and 731cm^{-1}, which are assigned to the bend vibration mode of C-CH in the complex. The vibration mode at 1482 cm^{-1} was assigned to C-N stretching of the organic products. We observed vibration modes between 900-1100 cm^{-1} (C-S stretching). The observed features correspond to the ones previously reported.[9] The selected frequencies used for identification of $Pb(ddtc)_2Phen$ complex were: ν_{C-N} = 1482 cm^{-1} ; ν_{C-S} = 900-1100 cm^{-1}; ν_{C-H} = 2920-2970 cm^{-1}; ν_{Phen} = 840 cm^{-1},770 cm^{-1}. Similarly for the mixed precursor, the

measured frequencies were: ν_{C-N} = 1482 cm^{-1}; ν_{C-S} = 982 cm^{-1}, 1075 cm^{-1}; ν_{C-H} = 2930-2970 cm^{-1}; ν_{Phen} = 840 cm^{-1},775 cm^{-1}.

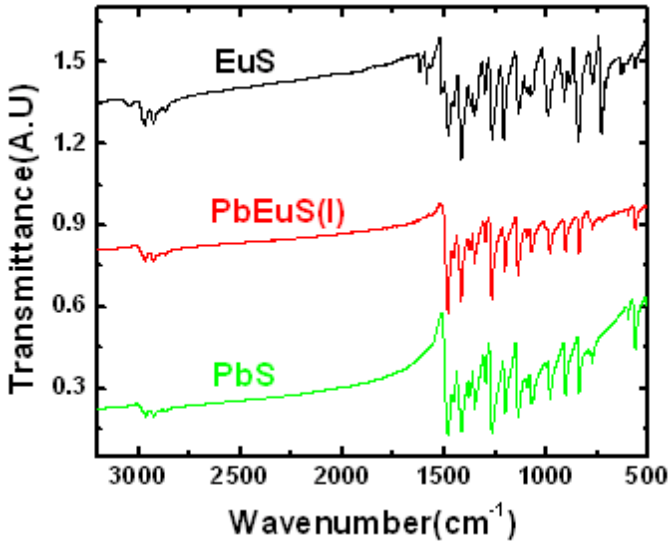

Figure 5.1: Fourier transforms infrared spectra of Eu $(ddtc)_2$Phen, Pb$(ddtc)_2$Phen, and its mixed precursor (Pb/Eu molar ratio: 10: 0.5).

To investigate the thermal decomposition of precursor complexes, thermogravimetric analyses were conducted. TGA monitors the weight of the sample as a function of temperature. Figure 5.2 A shows the TGA thermographs of PbS, PbEuS (Pb/Eu molar ratios, 10:0.5, 10:1 and 10:2), and EuS precursors, respectively. Pb/Eu molar ratios, 10:0.5, 10:1 and 10:2 were marked as PbEuS-I, PbEuS-II, and PbEuS-III respectively in the TGA curve. In all TGA curves, no significant mass loss was observed at temperatures at or below 100 ºC, which was a strong indicator of the absence of water and organic solvents that were used during the synthesis and cleaning. For the PbS precursor, a precipitous decomposition transition occurred between 280 ºC and 365 ºC,

which accounted for a relative mass loss of 80%. This corresponded to the loss of the organic moiety from the total mass of the precursor. The EuS precursor decomposed in two steps. The majority of the mass loss, approximately 60%, occurred in the 100 ºC to 415 ºC temperature range. This indicated the rapid, vigorous decomposition of the single source precursor and the initial nucleation and growth of the EuS nanoparticles. Another smaller transition in the TGA designated a second stage in the decomposition process. This occurred in the 590 ºC to 675 ºC temperature range with a mass loss of 10% during the transition. The 10% mass loss represented the decomposition of residual inorganic and organic compounds of the initial precursor material, yielding the final product at the end of decomposition. The PbEuS-I precursor showed characteristics similar to the binary PbS precursor; a complete decomposition occurred above 380 ºC. For PbEuS-II, a steady loss was observed from around 150 ºC-300 ºC with a weight percentage loss of nearly 10%. A second steep decomposition occurred between 300 ºC and 375 ºC accounting for a mass loss of 65%. Similarly for PbEuS-III, a steady mass loss was observed between 100 ºC-280 ºC with a mass percentage loss of approximately 10%, and a second steep decomposition was observed between 300 ºC and 375 ºC. All TGA curves exhibited small fluctuations within the TGA data, attributed to the instrument, which did not obfuscate the results or influence our conclusions.

5.3.2 Structural characterization of Nanocrystals

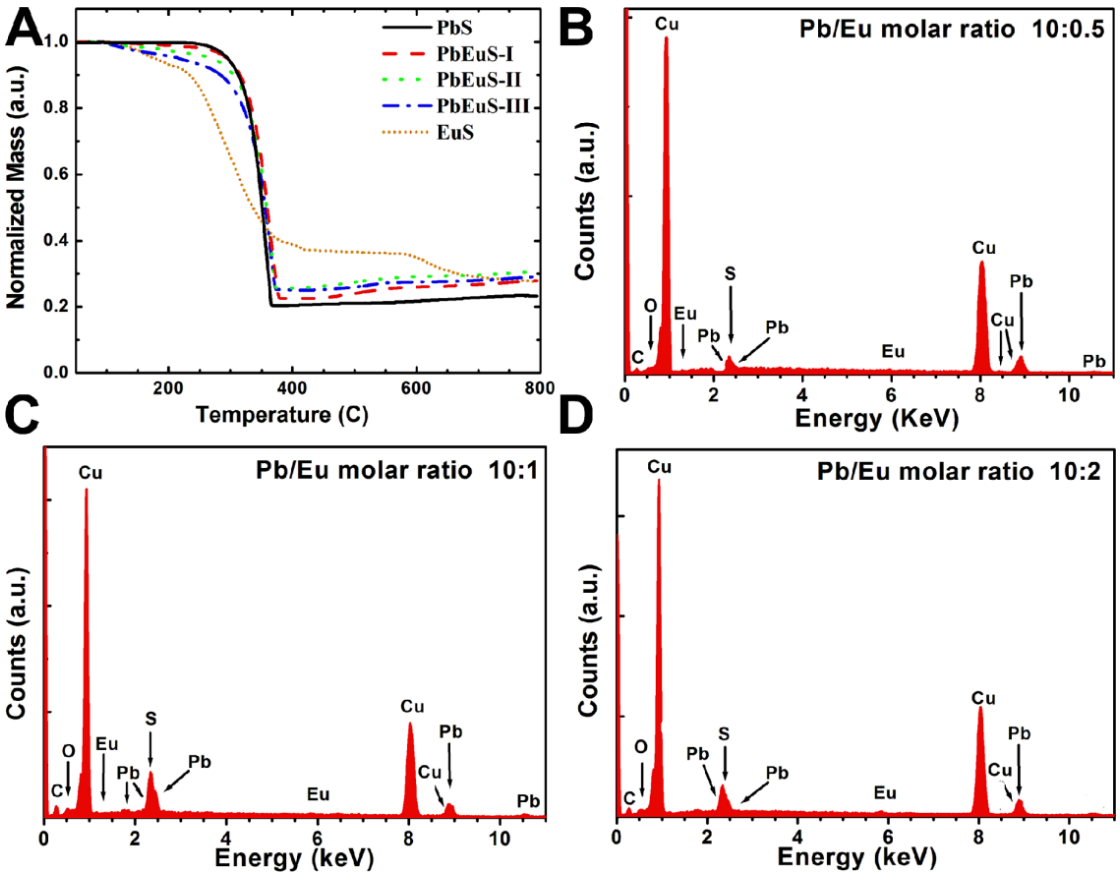

Figure 5.2: A) Thermogravimetric analysis curves of PbS, PbEuS I, II, III (Pb/Eu molar ratios, 10:0.5, 10:1, and 10:2), and EuS precursors. B), C), and D) show the EDS spectrum of Pb_xEu_yS nanocrystals (Pb/Eu molar ratios: 10:0.5, 10:1, and 10:2) on Cu substrate which reveals the presence of Pb, Eu and S.

Energy dispersive x-ray spectroscopy (EDS) provided elemental identification and a qualitative comparison of the amount of europium in the PbEuS precursor and the amount of europium in the PbEuS nanocrystals. Figure 5.2 B, C and D show the typical EDS spectrum of PbEuS nanocrystals of Pb/Eu molar ratios: 10:0.5, 10:1 and 10:2 respectively, obtained at 20 kV, along with peak assignments for Pb, Eu and elements.

Table 5.1 shows the results obtained for the stoichiometry ratios of the nanocrystals, as determined through EDS. For the two binary compositions (PbS and EuS), the cation:anion ratios were approximately 1:1 (0.93:1 and 1.05:1, respectively) as anticipated. In the ternary compositions, the fraction of Eu among the cations scales with the fraction of Eu precursor used for the nanocrystal syntheses. We believe that Eu is present in the nanocrystals at higher fractions than the stated precursor fractions would predict because of its earlier decomposition during heating, per the TGA data. It is likely that Eu is already incorporated into the "seed material" from which the nanocrystals grow as the Pb precursor decomposes.

In some of the nanocrystal samples prepared from Pb:Eu precursor ratio 10:0.5, we did not detect Eu, while in other samples, we detected Eu at a fraction significantly greater than the mean value of 6.1%. This variation contributed to the notably larger standard deviation value in the cation:anion ratio reported for 10:0.5 nanocrystals than for the other two ternaries. The variation in this measurement is attributed to the fact that there is no active mixing during the reaction. Inevitably, some regions of the reaction vessel will not contain Eu precursor, and by logical extension, some regions will contain more than the stated fraction of Eu precursor.

One unexpected observation from the composition measurements is that the cation:anion ratio decreases as the Eu content increases. Two mechanisms for this decrease, which may be concomitant, are plausible: (1) the lattice mismatch between PbS and EuS may lead to an increase in vacancy defect sites that lead to an overall cation reduction in the nanocrystal as Eu content rises; (2) the difference in the decomposition behavior of the Pb and Eu precursors may lead to different rates of cation incorporation

in the nanocrystals.

Table 5.1. Stoichiometric information for PbS, EuS and Pb_xEu_yS nanocrystals determined by EDS.

Precursor Composition	Atomic Composition Determined by EDS measurements				
Relative amount of Eu in the precursor [Eu/Eu+Pb] %	Relative amount of Eu in the nanocrystal [Eu/Eu+Pb] %	Pb:S ratio	Eu:S ratio	Cation:anion ratio	Chemical Formula Determined by EDS
0	0	0.93	0	0.93 ± 0.03	$Pb_{0.93}S$
100	100	0	1.05	1.05 ± 0.08	$Eu_{1.05}S$
4.76	6.1	0.84	0.05	0.89 ± 0.14	$Pb_{0.84}Eu_{0.05}S$
9.09	12.2	0.72	0.10	0.82 ± 0.04	$Pb_{0.72}Eu_{0.10}S$
16.6	18.7	0.64	0.15	0.79± 0.04	$Pb_{0.64}Eu_{0.15}S$

Figure 5.3A showed the X-ray diffraction patterns of PbS, $Pb_{0.84}Eu_{0.05}S$, $Pb_{0.72}Eu_{0.10}S$, and $Pb_{0.64}Eu_{0.15}S$ nanocrystals together with the indexing of three diffraction peaks. Since the lattice mismatch between PbS and EuS is very small, the shift in the XRD peak for Pb_xEu_yS nanocrystals with increasing Eu content, with respect to that for PbS nanocrystals, was more easily identified at higher order diffraction angles. Experimental data of $2\theta > 107°$ showed good agreement with the standard JCPDS data [JCPDS card file: 5-592 and 26-1419]. As the Eu content of the alloyed nanocrystals increased, the diffraction peaks in the XRD patterns gradually shifted toward smaller angles. The continuous shift of the peak of the alloyed nanocrystals ruled out phase separation of EuS and PbS and confirmed the formation of stable alloys of the Pb_xEu_yS ternary system. The lattice constant of Pb_xEu_yS nanocrystal was deduced from the average shift of the diffraction peaks relative to those of PbS. In doing this, we used data

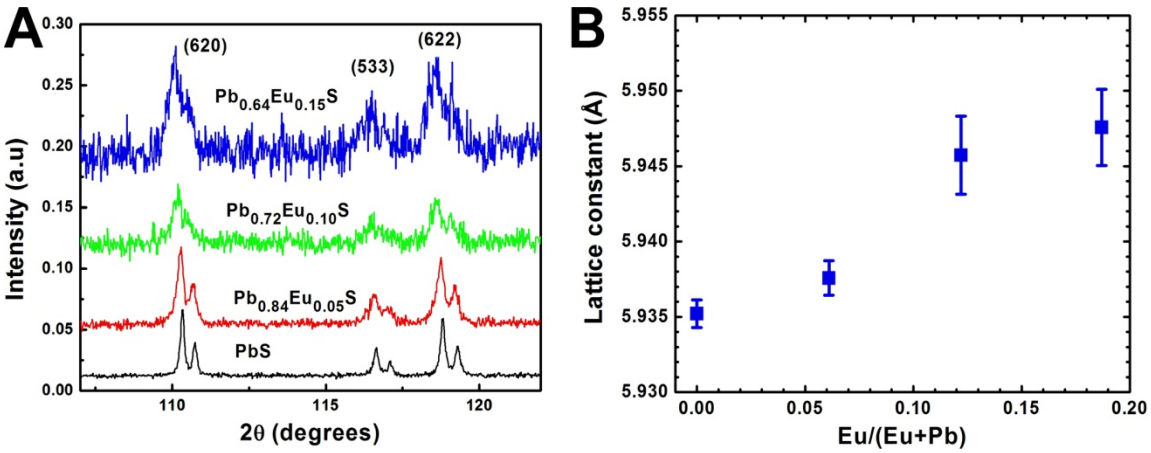

Figure 5.3**:** A**)** X-ray diffraction (XRD) spectra of PbS, $Pb_{0.84}Eu_{0.05}S$, $Pb_{0.72}Eu_{0.10}S$, and $Pb_{0.64}Eu_{0.15}S$ nanocrystals. B**)** Graph of the dependence of the lattice constants of Pb_xEu_yS nanocrystals on different Eu concentrations.

corresponding to ten higher angle diffraction planes beginning with (5 1 1) and ending with (6 4 0). The variation of lattice parameter with Eu atomic composition is shown in Figure 5.3B. A gradual increase in lattice parameter is observed as the Eu composition increases. The increase in degree of lattice deformation with Eu composition has also been observed in the XRD measurements for which the half-width of the X-ray peak becomes broader as a function of the Eu composition y.[33, 110]

To analyze the size and structure of nanomaterials, methanolic solutions of the Pb_xEu_yS nanocrystals were dropcasted onto holey carbon films mounted on TEM specimen grids (Ted-Pella). TEM images were obtained using a Philips CM 20 microscope operating at 200 KV. Figure 5.4 A shows the TEM image of $Pb_{0.84}Eu_{0.05}S$ nanocrystals synthesized at 700 ºC. A higher resolution TEM image (Figure 5.4 B) indicates that these nanoparticles are single crystalline. The value of the well-resolved lattice plane d-spacing, corresponding to (111) plane of $Pb_{0.72}Eu_{0.10}S$ nanocrystals, agrees

well with the values obtained from XRD. Figure 5.5 (A) shows the TEM images of ~ 4.3 nm $Pb_{0.72}Eu_{0.10}S$ nanocrystals and Figure 5.5 B represents the TEM images of ~ 4.5 nm $Pb_{0.64}Eu_{0.15}S$ nanocrystals.

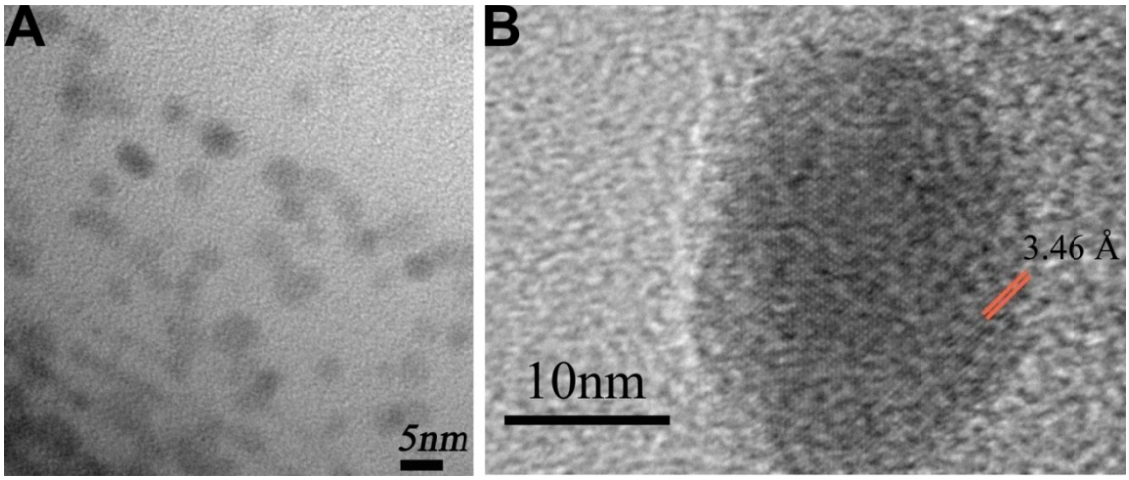

Figure 5.4**:** TEM images of the synthesized Pb_xEu_yS nanomaterials. (A).TEM image of ~5nm $Pb_{0.84}Eu_{0.05}S$ nanocrystals. (B) TEM image of the ~20 nm $Pb_{0.72}Eu_{0.10}S$ nanocrystals showing diffraction fringes corresponding to the (111) atomic planes.

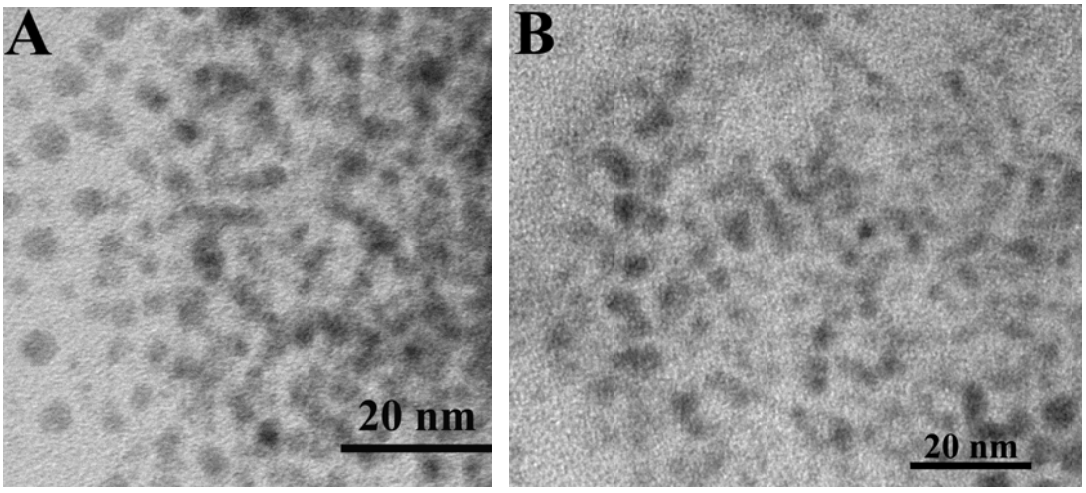

Figure 5.5: (A) TEM images of ~ 4.3 nm $Pb_{0.72}Eu_{0.10}S$ nanocrystals. (B) TEM images of ~ 4.5 nm $Pb_{0.64}Eu_{0.15}S$ nanocrystals.

5.3.3 Magnetic characterization of Nanocrystals

Vibrating sample magnetometry (VSM), conducted with a Quantum Design PPMS system, provided characterization of the magnetization as a function of temperature, m(T), and the magnetization as a function of applied field, m(H). Field-cooled (FC) measurements of m(T) were conducted on PbS, EuS, $Pb_{0.84}Eu_{0.05}S$, and a mixture of PbS and EuS nanocrystals (hereafter referred to as PbS+EuS) prepared under the same thermolysis conditions. The relative amount of europium in $Pb_{0.84}Eu_{0.05}S$ and PbS+EuS nanocrystals are the same. The temperature dependent magnetization data (Figure 5.6 A) were obtained at a constant field of 1000 Oe with temperatures ranging from 2 K to 30 K. For PbS nanocrystals, we found essentially no temperature dependence of the magnetization, characteristic of diamagnetic materials.[102, 111] We found that EuS and PbS+EuS nanocrystals ordered ferromagnetically at ~16.6 K, consistent with the Curie temperature of bulk EuS of 17 K.[18] The magnetization data for the $Pb_{0.84}Eu_{0.05}S$ samples as a function of temperature, taken at a constant magnetic field, produced no maxima for magnetization, indicating a paramagnetic behavior. m(H) experiments on PbS, EuS, $Pb_{0.84}Eu_{0.05}S$, and PbS+EuS nanocrystals were conducted at temperatures between 2 K and 25 K. Figure 5.6 B illustrates the magnetization hysteresis measurements of the materials at 2 K for a cycling field of ±16 T. Pure PbS nanocrystals were measured as a baseline and were found to be diamagnetic, as expected.[102, 111] A pronounced saturation magnetization was observed for EuS and PbS+EuS nanocrystals at 2 K, which is characteristic of a ferromagnet.[9, 13] For $Pb_{0.84}Eu_{0.05}S$ nanocrystals, m(H) dependencies at 2 K exhibited a saturation magnetization around 7 Tesla.

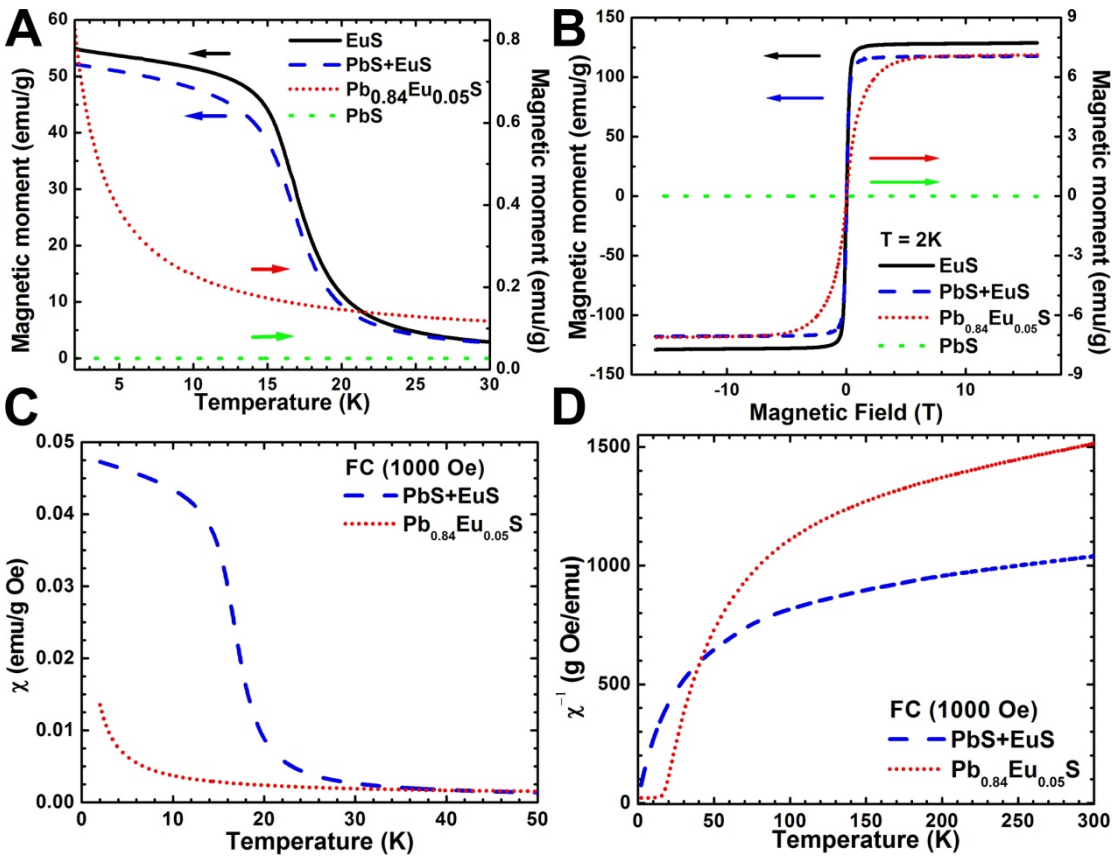

Figure 5.6**:** Magnetization measurements of PbS, EuS, $Pb_{0.84}Eu_{0.05}S$, and a mixture of PbS and EuS nanocrystals prepared under the same thermolysis conditions. A) FC measurements of the magnetization as a function of temperature. B) High field magnetization hysteresis graphs for the four samples measured at 2K. C) FC measurements of the magnetic susceptibility χ as a function of temperature. (D) Inverse magnetic susceptibility χ^{-1} as a function of temperature.

A closer analysis of the magnetization data provides information about the nature of magnetic interactions in $Pb_{0.84}Eu_{0.05}S$ nanocrystals. The dependence of magnetic susceptibility χ (defined as the ratio of the magnetization and the magnetic field) per Eu ion and the inverse susceptibility χ^{-1} per Eu ion on temperature are shown in Figure 5.6 C

and 5.6 D respectively. In the χ^{-1} versus temperature graph of $Pb_{0.84}Eu_{0.05}S$ nanocrystals, the magnetic data above 200 K fit well to the Curie-Weiss law with $\theta = -962.783$. The large negative Curie-Weiss temperature implies the dominance of antiferromagnetic interactions between the Eu atoms at low temperatures, which agrees with previous reports on bulk lead europium sulfide.[35] The inverse magnetic susceptibility data for our PbS+EuS nanocrystals are comparable to inverse susceptibility results, measured by SQUID magnetometry, that were previously reported for EuS nanocrystals of ≤ 10 nm.[9] The temperature dependence of χT for $Pb_{0.84}Eu_{0.05}S$ nanocrystals and the PbS+EuS mixture of nanocrystals are shown in Figure 5.7. A decrease in χT for decreasing in temperature is observed for $Pb_{0.84}Eu_{0.05}S$ nanocrystals, characteristic for an antiferromagnetic interaction. For PbS+EuS nanocrystals, a rapid rise in χT as the temperature dropped below ~25 K was indicative of ferromagnetic interactions between Eu^{2+} ions. Our magnetization measurements showed that $Pb_{0.84}Eu_{0.05}S$ NCs exhibited paramagnetic properties down to 2 K with the appearance of an antiferromagnetic interaction between Eu atoms at low temperatures. In contract, PbS NCs was diamagnetic, and EuS and PbS+EuS NCs were ferromagnetic at these temperatures. These results provide strong convincing evidence that no phase separation of $Pb_{0.84}Eu_{0.05}S$ into PbS and EuS existed. Thus, by tuning the europium content of the ternary, we can produce ferromagnetic NCs, paramagnetic NCs, and diamagnetic NCs.

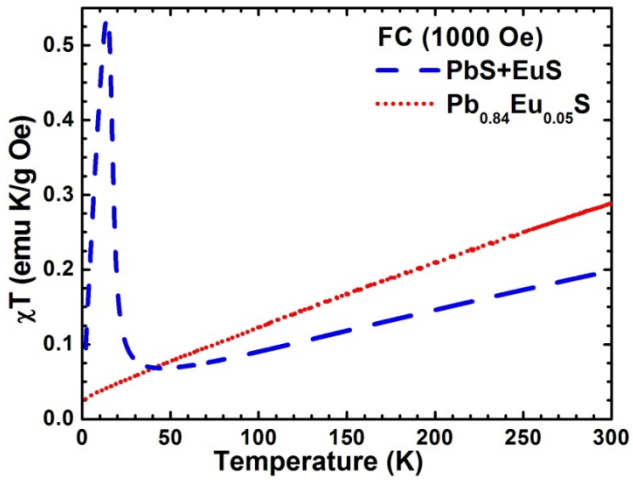

Figure 5.7: Temperature dependence of χT of $Pb_{0.84}Eu_{0.05}S$ and a mixture of PbS and EuS nanocrystals.

5.4 Concentration dependence of the exchange interaction of lead europium sulfide nanocrystals

5.4.1 Review of exchange mechanisms in bulk DMS

A brief review of the exchange mechanisms in bulk DMSs is necessary to describe the concentration dependent exchange interaction in lead europium sulfide nanocrystals. In DMS, if the density of magnetic ions is vanishingly small and the spins are noninteracting, the localized spins follow Maxwell-Boltzmann statistics, resulting in a magnetization M induced by an applied field H at temperature T, given by a Brillouin function of $\frac{H}{T}$:

$$M = xN_0 g\mu_B JB_J\left(\frac{Jg\mu_B H}{k_B T}\right) \tag{5.1}$$

where x is the proportion of cations substituted by magnetic ions, N_0 is the number of cation sites per gram, g is called the g factor , μ_B is the Bohr magneton, J is the total angular momentum quantum number and k_B is the Boltzmann constant.[112] For any non-vanishing concentration of magnetic ions, the standard Brillouin function is inadequate for describing the magnetization data because of the interaction between magnetic ions.[113] This interaction results in a reduction of magnetization and is quantitatively described by a "modified Brillouin function", for which x is replaced by the number of free spins $\bar{x}_1$ and the argument is $\frac{H}{T+T_0}$. T_0 represents an exchange interaction. The values of the two phenomenological parameters $\bar{x}_1$ and T_0 are experimentally well described in many of the usual DMSs such as $Cd_{1-x}Mn_xTe$, $Pb_{1-x}Gd_xTe$, $Pb_{1-x}Mn_xTe$ and $Pb_{1-x}Mn_xSe$.[114, 115] For example, Gaj et.al [114]reported that in $Cd_{1-x}Mn_xTe$, the modified Brillouin function fits the experimental data very well for Mn composition (x) up to 0.02.

The description provided by a modified Brillouin function has proven to be very effective at moderately low temperatures (1.5 K to 20 K), moderate fields (upto 5 T), and composition of magnetic ions up to ~ 0.02.[114] In this relevant temperature, field, and composition ranges, the number of free spins $\bar{x}_1$ closely matches the numbers of magnetic atoms that remain when the nearest-neighbor pairs have been deducted.[116] Also, at this range, T_0 represents primarily the pair exchange interaction.[116] Anderson et.al reported that in IV-VI compound DMSs materials, the modified Brillouin function approach is reasonably good at fields below 5 T, but do not adequately describe the magnetization up to high fields.[117] In order to describe properly the magnetization, a pair

interaction function was also included in the magnetization term. This approach showed reasonable results in IV-VI DMS, when the measurement were carried out at temperatures low enough and fields high enough, that the magnetization nearly saturates. However, this approach is not adequate for large amounts of magnetic ions because of the large contribution of clusters to the exchange mechanism.[101]

Before presenting our experimental data, it is worth noting to mention that if we use the Curie-Weiss temperature,θ (see section 1.2.1) or the modified Brillouin function parameter T_0 to determine the exchange parameter, we actually determine the average of all the exchange interactions between magnetic ions in the sample. But for a low concentration of magnetic ions, θ and T_0 would represent the nearest –neighbor exchange parameter.[62]

5.4.2 Results and discussion

To our knowledge, the magnetic properties of nanoscale IV−VI semiconductors containing Eu^{2+} in their matrixes have not been reported. Magnetic properties of these nanomaterials are expected to be influenced by the quantum confinement of the electronic states and, hence will differ from the electronic states of the bulk crystals. For the present magnetic study, we selected three ternary nanocrystals $Pb_{0.84}Eu_{0.05}S$, $Pb_{0.72}Eu_{0.10}S$ and $Pb_{0.64}Eu_{0.15}S$, synthesized under the same thermolysis conditions. Eventhough, our ternary nanoparticles were not entirely monodispersed, we expect a size dependent effect on the exchange interaction of these materials as compared to bulk.

To gain an insight into the effect of Eu concentration (y) on the exchange interaction in Pb_xEu_yS nanocrystals, we performed low-temperature high –field magnetization measurements on our samples using vibration sample magnetometry system. Fig.5.8 showed the high-field magnetization M versus magnetic field H at 2 K for the as-synthesized Pb_xEu_yS nanocrystals. As anticipated, the saturation magnetization was larger for larger values of Eu concentration. Since the Eu content in our ternary samples are not vanishingly small, the standard Brillouin function cannot be applied to fit our experimental data. Even though, the modified Brillouin function was not adequate for higher composition of magnetic ion, Anderson et.al estimated the exchange parameter for $Pb_{1-x}Gd_xTe$ (x~0.7) using the modified Brillouin function. The results were in reasonable agreement with the low-temperature susceptibility measurements.[115] To explore more about the exchange mechanisms at low temperatures and moderate fields, we decided to fit our experimental data first with the modified Brillouin function. Alex Krejci of Dickerson's group analysed the data using Mathematica and provided the fitting parameters.

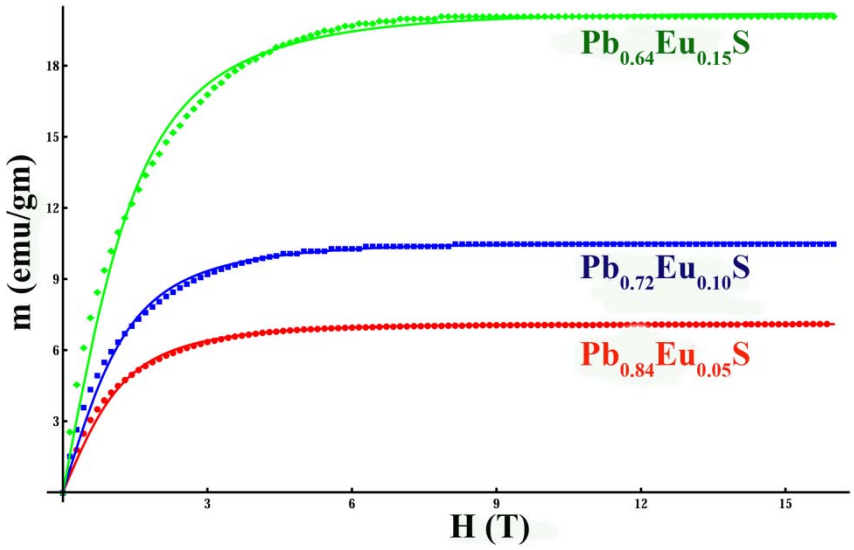

Fig.5.8: Magnetization versus field curves for Pb_xEu_yS nanocrystals (y= 0.05, 0.1 and 0.15) prepared under the same thermolysis condition, measured at 2 K. The solid curves were fitting to the experimental data using the modified Brillouin function.

To fit the experimental data, we used the modified Brillouin function in a way similar to that done for IV-VI DMS's [101, 102, 117, 118], expressing the magnetization as

$$M = M_s + \chi_0 H \tag{5.2}$$

where $M_s = g\mu_B N_0 S\bar{x}_1 B_s(\zeta)$ (5.3)

$B_s(\zeta)$ is the modified Brillouin function

$$B_s(\zeta) = \frac{2S+1}{2S}\coth\left(\frac{2S+1}{2S}\zeta\right) - \frac{1}{2S}\coth\left(\frac{\zeta}{2S}\right) \tag{5.4}$$

$$\zeta = \frac{Sg\mu_B H}{k_B(T+T_0)} \tag{5.5}$$

In the case of Eu^{2+}, there is no net orbital contribution to the moment, $L = 0$ and $J = S$. S is 7/2 for $Eu2^{+}$ ion, μ_B is the Bohr magneton , N_0 is the number of cation sites per gram, H is the magnetic field, and T is the temperature. g is called the g-factor , which is given by

$$g = 1 + \frac{J(J+1)+S(S+1)-L(L+1)}{2J(J+1)} \tag{5.6}$$

For Eu^{2+}, Eq.5.6 gives $g = 2$. The total magnetization M is given in emu/g,and the magnetization $\chi_0 H$ of the host matrix was taken from our previous magnetization measurement of PbS NCs. The squares in Figure 5.8 represent the experimental data, and the solid lines were given by Eq.5.2. The two fitting parameter were $\bar{x}_1$ and T_0. Here $\bar{x}_1$ represent the number of separate effective Eu^{2+} ions located in cation sites, and T_0 is a phenomenological parameter that represents the exchange interactions among Eu^{2+} ions. The fitting parameters were shown in Table 5.2.

In Figure 5.8, which showed the magnetization of our three ternary samples, Eq.5.2 does not fit well for our high Eu content (y > 0.05)) at 2K. Even for our lowest Eu content (y~0.05), the fit was not good below 1Tesla. Based on previous literatures on

DMSs[117], the two parameter fits were fairly good at moderate field (< 5 T). This anomalous observation below 1 Tesla may be due the high Eu composition in our ternary.

Using Curie-Weiss temperature, θ, Spalek et.al [119] estimated the dominant exchange integral between the nearest neighbors,

$$\frac{J}{k_B} = \frac{3\theta}{2\bar{x}zS(S+1)} \tag{5.7}$$

where $\bar{x}$ is the effective number of magnetic ion spins, z is the number of nearest neighbors on cation sites and S is the magnetic ion spin. Since the modified Brillouin function in the low-field limit has the same form as the Curie –Weiss law and T_0 represents primarily the pair exchange interaction, an estimation of the exchange parameter using T_0 is possible. Following a procedure similar to Ref.[119], Anderson et.al[115] estimated the exchange parameter $\frac{J}{k_B}$ by assuming

$$\frac{J}{k_B} = -\frac{3T_0}{2\bar{x}_1 zS(S+1)} \tag{5.8}$$

The minus sign represents an antiferromagnetic exchange. z = 12 is the number of nearest neighbors per cation site. Following the approach of Anderson et.al [115], we estimated the exchange parameter $\frac{J}{k_B}$ (see table 5.2) . The value of $\bar{x}_1$, within experimental error is less than y. The magnitude of $\frac{J}{k_B}$ decreases with increasing y.

Table 5.2: Results of the Modified Brillouin function (Two-parameter fit) fits to the magnetization measurements for the Pb_xEu_yS nanocrystals.					
Pb_xEu_yS NCs	Temperature (K)	y	$\bar{x}_1$	T_0 (K)	$\frac{J}{k_B}$ (K)
$Pb_{0.84}Eu_{0.05}S$	2	0.05	0.044±0.001	0.962±0.237	- 0.175±0.042
$Pb_{0.72}Eu_{0.10}S$	2	0.10	0.064±0.001	1.186±0.346	- 0.146±0.041
$Pb_{0.64}Eu_{0.15}S$	2	0.15	0.123±0.003	1.754±0.500	- 0.113±0.031

As we have pointed out earlier in this section, in order to describe properly the magnetization in DMSs, we should take into account the exchange contribution from pairs of closely spaced magnetic ion.[116] Anderson et.al [101, 115, 117] have used three fitting parameters in the two-spin cluster model of Bastard and Lewiner [120] to calculate the magnetization contributions due to isolated magnetic ions M_s and pair interactions M_p. In the three parameter fit, T_0 has been set to zero. This is because in this case, T_0 represents the exchange contribution from magnetic ions other than pairs. For small magnetic ion concentration the fit is not very sensitive to the value of T_0.

To fit our experimental data, we used the three parameter fit in a way similar to that reported by Anderson et.al [101, 115, 117], expressing the magnetization as

$$M = M_s + M_p + \chi_0 H \tag{5.9}$$

Where M_p is given as

$$M_p = \frac{1}{2} g\mu_B N_0 \bar{x}_2 \frac{\sum_{s=0}^{S\max} \exp\left[\frac{J_p}{k_B T} s(s+1)\right] \sinh\left[\frac{2s+1}{2s}\zeta_p\right] sB_s(\zeta_p)}{\sum_{s=0}^{S\max} \exp\left[\frac{J_p}{k_B T} s(s+1)\right] \sinh\left[\frac{2s+1}{2s}\zeta_p\right]} \qquad (5.10)$$

$\zeta_p = \frac{Sg\mu_B H}{k_B T}, S_{\max} = 2S$, $\bar{x}_2$ is the effective number of magnetic ions in pairs and J_p is the pair exchange parameter.

The results of the fits were shown as solid lines in Figure 5.9; it is clear that fairly good fits were obtained. The three fitting parameters, $\bar{x}_1$ in M_s , $\bar{x}_2$, and J_p in M_p were shown in table 5.3. Here $\bar{x}_1$ and $\bar{x}_2$ represent the number of individual Eu^{2+} ions and the number of Eu^{2+} ions in pairs, respectively. The sum of ($\bar{x}_1 + \bar{x}_2$), within the experimental error, is less than y. Since T_0 has been set equal to zero, $\frac{J_p}{k_B}$ represents the pair contribution to the exchange. The absolute values of $\frac{J_p}{k_B}$ from the three parameter fits, within the experimental error, are larger than the $\frac{J}{k_B}$ values obtained from the two parameter fitting and are weakly dependent of the europium content. This result seems to be due to the large contribution of clusters to the exchange mechanism at large values of europium content. A similar result was observed by Gorska et.al,[101] for the low temperature high field magnetization measurements on Bridgeman grown $Pb_{1-x}Eu_xTe$. As mentioned in section 5.1, magnetization measurements on Bridgman grown $Pb_{1-x}Eu_xS$ single crystals ($x < 0.06$) at mK temperatures, using magnetization-steps method, found

a value of $\frac{J}{k_B}$ = -0.228 ± 0.007 K for the dominant antiferromagnetic exchange constant.[35] Since the magnetization analysis using modified Brillouin function and pair interaction yielded a rough estimate of the dominant antiferromagnetic exchange constant J ,a comparison of our results with the results determined using magnetization-steps measurement is not possible. Magnetization-step measurements at mK temperatures with our ternary nanocrystals, for specific nanoparticle sizes, are required to understand the effect of size and europium concentration on the exchange mechanism.

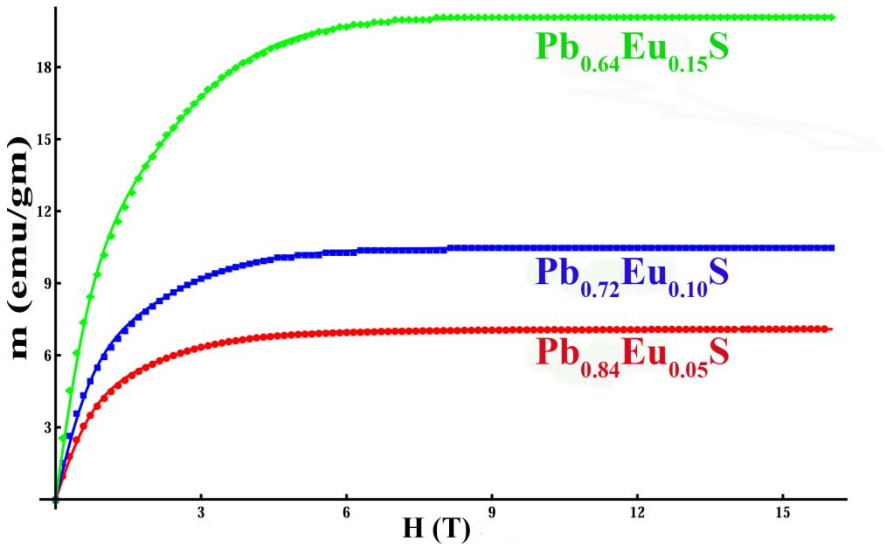

Fig.5.9: Magnetization versus field curves for Pb_xEu_yS nanocrystals (y= 0.05, 0.1 and 0.15) prepared under the same thermolysis condition, measured at 2 K. The solid curves were obtained from the three parameter fit.

Table 5.3: Results of the Modified Brillouin function plus pairs (three- parameter fit) fits to the magnetization measurements for the Pb_xEu_yS nanocrystals.

Pb_xEu_yS NCs	Temperature (K)	y	$\bar{x}_1$	$\bar{x}_2$	$\frac{J_p}{k_B}$(K)
$Pb_{0.84}Eu_{0.05}S$	2	0.05	0.035±0.001	0.009±0.001	-0.380±0.060
$Pb_{0.72}Eu_{0.10}S$	2	0.10	0.048±0.003	0.016±0.003	- 0.390±0.060
$Pb_{0.64}Eu_{0.15}S$	2	0.15	0.080±0.004	0.042±0.004	- 0.410±0.043

5.5 Summary

In summary, we have demonstrated the first synthesis and characterization of homogenously alloyed Pb_xEu_yS nanocrystals. Mixed precursors of a 1,10-phenanthroline, europium diethyldithiocarbamate complex $[Eu(ddtc)_2Phen]$ and a 1,10-phenanthroline, lead diethyldithiocarbamate complex $[Pb(ddtc)_2Phen]$ have been used in a facile thermolysis technique to produce Pb_xEu_yS nanocrystals. The alloy structure of Pb_xEu_yS nanocrystals was affirmed by X-ray diffraction, in which the diffraction peaks systematically shifted toward smaller angles as the Eu atomic concentration increased. The lattice parameter measured from XRD patterns increased linearly with the increase of Eu content. The alloy structure was also confirmed by the vibrating sample magnetometry measurements, in which $Pb_{0.84}Eu_{0.05}S$ nanocrystals exhibited paramagnetic properties down to 2K with the appearance of antiferromagnetic interactions between the Eu atoms at low temperatures. In contrast, PbS was diamagnetic, and EuS was ferromagnetic at these temperatures. From the high field

magnetization measurements at 2K, fitted to a modified Brillouin function, the exchange parameter $\frac{J}{k_B}$ of Pb_xEu_yS nanocystals was obtained for different values of y. The magnitude of $\frac{J}{k_B}$ decreased with increasing y. The pair exchange constant $\frac{J_p}{k_B}$ was obtained by fitting the high field magnetization to an expression containing both modified Brillouin function and a term representing the pair interaction. The value of $\frac{J_p}{k_B}$ was found to be weakly dependent on y. We believe that for high Eu concentration, the pair assumption in the three parameter fitting included not only true pairs but also triplets, quartets and large clusters. Hence the exchange $\frac{J_p}{k_B}$ will appear to be larger than it actually is. A systematic size dependent study is required to understand the influence of size on the exchange interaction of these nanomaterials. Synthesis of monodisperse, ternary Pb_xEu_yS nanocrystals opens up opportunities for fundamental studies of concentration and size dependent optical, electrical and magnetic properties and could lead to the development of nanoscale infrared and spintronics device.

CHAPTER VI

CONCLUSION

This dissertation explored the development, optical and magnetic studies of europium sulfide and lead europium sulfide nanocrystals. A summary of the research accomplishments and the proposed future studies are outlined here.

A novel one-step solvothermal synthesis technique was employed to produce stable, highly crystalline, monodisperse europium sulfide nanocrystals. We synthesized a range of nanoparticle sizes to investigate the role of particle size on the optical and magnetic properties of EuS nanocrystals. Quantum confinement behavior in EuS NCs was observed with continuous blue-shift in the absorption and luminescence spectra as the crystal size decreased. The ferromagnetic ordering temperature (T_c) was observed to be strongly dependent on the size of the EuS nanocrystals. The magnetic nanoparticles are promising materials for applications, such as bioimaging reagents, active material in magneto-optic devices.

We have demonstrated the first synthesis and characterization of nanocrystalline alloyed lead europium sulfide, a potentially important dilute magnetic semiconductor. Unlike previous research on bulk forms of the material, we observed that nanocrystalline lead europium sulfide alloy astochiometrically and that this phenomenon changes as the europium content increases. By tuning the europium content of the ternary alloys, we were able to produce ferromagnetic NCs, paramagnetic NCs and diamagnetic NCs.

Concentration dependence of the exchange interaction in Pb_xEu_yS nanocrystals was investigated. We observed that the exchange constant $\frac{J}{k_B}$ was negative and that its magnitude decreased with increasing Eu content(y). However, the pair exchange constant $\frac{J_p}{k_B}$ was weakly dependent on y. Since our ternary nanocrystals exhibited paramagnetic properties down to 2K with the appearance of antiferromagnetic interactions between the Eu atoms at low temperatures, a better understanding of the exchange mechanism is possible with magnetization measurements at very low temperatures.

The research on Pb_xEu_yS nanocrystals should be explored further. A new synthesis technique should be required to produce size controlled, surface protected Pb_xEu_yS nanocrystals. This technique must have a versatility to produce a wide range of particle sizes so that we can study the effect of size and europium concentration on the magnetic and optical properties of Pb_xEu_yS nanocrystals. This could lead to the development of nanoscale infrared and spintronics device.

Once this research is accomplished, study can be extended towards potential device application of these materials. For device application, it is necessary to assemble this nanocrytals into films and study their optical and magnetic properties. Among the various deposition techniques to produce nanocrystal films, electrophoretic deposition (EPD) provides a facile means of assembling nanoparticles into thin films with large – scale homogeneity. Thin films of electrophoretically deposited, uniformly distributed Eu

based nanomaterials may be a more viable opt ion for magneto-optical devices, such as optical switches, optical isolators, and optical memories.

REFERENCES

[1] Gambino, R. J.; Fumagalli, P. Ieee Transactions on Magnetics 1994, 30, 4461.

[2] Fumagalli, P.; Spaeth, C.; Rudiger, U.; Gambino, R. J. Ieee Transactions on Magnetics 1995, 31, (6), 3319-3324.

[3] Gunthero.G; Schoenes, J.; Wachter, P. Journal of Applied Physics 1970,41, (3), 1083.

[4] Schoenes, J.; Wachter, P. Ieee Transactions on Magnetics 1976, 12, (2), 81-85.

[5] Gambino, R. J.; Fumagalli, P.; Ruf, R. R.; Mcguire, T. R.; Bojarczuk, N.Ieee Transactions on Magnetics 1992, 28, (5), 2973-2975.

[6] Tu, K.; Ahn, K. Y.; Suits, J. C. Ieee Transactions on Magnetics 1972, 3, 651-653.

[7] Yanase, A.; Kasuya, T. Progress of Theoretical Physics 1970, 46, 388.

[8] Zhao, F.; Sun, H. L.; Gao, S.; Su, G. Journal of Materials Chemistry 2005, 15, (39), 4209-4214.

[9] Zhao, F.; Sun, H. L.; Su, G.; Gao, S. Small 2006, 2, (2), p.244-248.

[10] Ghosh, D. B.; De, M.; De, S. K. Physical Review B 2004, 70, (11), 115211-115217.

[11] Henriques, A. B.; Wierts, A.; Manfrini, M. A.; Springholz, G.; Rappl, P.H. O.; Abramof, E.; Ueta, A. Y. Physical Review B 2005, 72, (15), 155337-155341.

[12] Mauger, A.; Godart, C. Physics Reports (Review Section of Physics Letters) 1986, 141, (Nos.2&3), 51-176.

[13] Redigolo, M. L.; Koktysh, D. S.; Rosenthal, S. J.; Dickerson, J. H.; Gai,Z.; Gao, L.; Shen, J. Applied Physics Letters 2006, 89, (22), p.222501.

[14] Kataoka, T.; Tsukahara, Y.; Hasegawa, Y.; Wada, Y. Chemical Communications 2005, (48), 6038-6040.

[15] Sellmyer, D. J.; Yu, M.; Kirby, R. D. Nanostructured Materials 1999, 12,(5-8), 1021-1026.

[16] Sellmyer, D. J.; Yu, M.; Thomas, R. A.; Liu, Y.; Kirby, R. D. Physics of Low-Dimensional Structures 1998, 1-2, 155-165.

[17] Sun, S. H.; Murray, C. B. Journal of Applied Physics 1999, 85, (8), 4325-4330.

[18] Thongchant, S.; Hasegawa, Y.; Wada, Y.; Yanagida, S. Journal of Physical Chemistry B 2003, 107, (10), 2193-2196.

[19] Thongchant, S.; Hasegawa, Y.; Wada, Y.; Yanagida, S. Chemistry Letters 2003, 32, (8), 706-707.

[20] Murray, C. B.; Kagan, C. R.; Bawendi, M. G. Annual Review of Materials Science 2000, 30, 545-610.

[21] Regulacio, M. D.; Bussmann, K.; Lewis, B.; Stoll, S. L. Journal of the American Chemical Society 2006, 128, (34), 11173-11179.

[22] Chen, W.; Zhang, X. H.; Huang, Y. N. Applied Physics Letters 2000, 76, (17), 2328-2330.

[23] Regulacio, M. D.; Kar, S.; Zuniga, E.; Wang, G.; Dollahon, N. R.; Yee, G.T.; Stoll, S. L. Chemistry of Materials 2008, 20, (10), 3368-3376.

[24] Thongchant, S.; Hasegawa, Y.; Tanaka, K.; Fujita, K.; Hira, K.; Wada, Y.; Yanagida, S. Japanese Journal of Applied Physics Part 2-Letters 2003, 42, (7B), L876-L878.

[25] Redigolo, M. L.; Koktysh, D. S.; van Benthem, K.; Rosenthal, S. J.; Dickerson, J. H. Materials Chemistry and Physics 2009, 115, (2-3), 526-529.

[26] Furdyna, J. K. Journal of Applied Physics 1988, 64, (4), R29-R64.

[27] Snure, M.; Kumar, D.; Tiwari, A.; . JOM 2009, 61, (6), 72.

[28] Geist, F.; Herbst, W.; MejiaGarcia, C.; Pascher, H.; Rupprecht, R.; Ueta, Y.; Springholz, G.; Bauer, G.; Tacke, M. Physical Review B 1997, 56, (20), 13042-13053.

[29] Partin, D. L. Ieee Transactions on Electron Devices 1984, 31, (12), 1975.

[30] Schwarzl, T.; Springholz, G.; Borerl, M.; Kaufmann, E.; Roither, J.; Heiss,W.; Furst, J.; Pascher, H. Applied Physics Letters 2005, 86, (3), 031102-031104.

[31] Norton, P.; Tacke, M. Journal of Crystal Growth 1987, 81, (1-4), 405-410.

[32] Heiss, W.; Boberl, M.; Schwarzl, T.; Springholz, G.; Furst, J.; Pascher, H. Iee Proceedings-Optoelectronics 2003, 150, (4), 332-336.

[33] Ishida, A.; Sase, Y.; Okamura, T.; Nakahara, N.; Fujiyasu, H.; Nishizima, Y.; Shinohara, K. Superlattices and Microstructures 1989, 6, (1), 27-30.

[34] Gorska, M.; Lusakowski, A.; Jedrzejczak, A.; Golacki, Z.; Galaazka, R. R.; Anderson, J. R.; Balci, H. Physical Review B 2006, 73, (12), 125201-125210.

[35] Bindilatti, V.; ter Haar, E.; Oliveira, N. F.; Liu, M. T.; Shapira, Y.;Gratens, X.; Charar, S.; Isber, S.; Masri, P.; Averous, M.; Golacki, Z.;McNiff, E. J. Physical Review B 1998, 57, (13), 7854-7862.

[36] Ishida, A.; Nakahara, N.; Okamura, T.; Sase, Y.; Fujiyasu, H. Applied Physics Letters 1988, 53, (4), 274-275.

[37] Couino, G.; Gacoin, T.; Boilot, J. P. Solid State Communications 2000, 114, 547.

[38] Radovanovic, P. V.; Gamelin, D. R. Journal of the American Chemical Society 2001, 123, (49), 12207-12214.

[39] Hanif, K. M.; Meulenberg, R. W.; Strouse, G. F. Journal of the American Chemical Society 2002, 124, (38), 11495-11502.

[40] Callister Jr, W. D., Materials Science and Engineering, An Introduction. In V11 ed.; John Wiley & Sons,Inc.: 2007.

[41] Cullity, B. D., Introduction to Magnetic Materials. In Addison-Wesley Series in Metallurgy and Materials: 1972.

[42] Jiles, D., Introduction to Magnetism and Magnetic Materials. In Chapman & Hill: 1998.

[43] Blundell, S., Magnetism in Condensed Matter. In Oxford University Press: 2001.

[44] Lacheisserie, E. T.; Gignoux, D.; Schlenker, M., Magnetism:Fundamentals. In Springer: 2005.

[45] Pathria, R. K., Statistical Mechanics. In II ed.; Elsevier: 1996.

[46] Kasuya, T. Ibm Journal of Research and Development 1970, 14, (3), 214.

[47] Kachhava, C. M., Solid State Devices and Electronics. In New Age international Publishers: 2003.

[48] Liz-Marzan, L. M.; Giersig, M., Low-dimensional systems: Theory,preparation, and some applications. In Kluwer Academic Publishers:2003.

[49] Knobe, M.; Nunes, W. C.; Socolovsky, L. M.; De Biasi, E.; Vargas, J. M.; Denardin, J. C. Journal of Nanoscience and Nanotechnology 2008, 8, 2836-2857.

[50] Eisenmenger, J.; Schuller, I. K. Nature Materials 2003, 2, (7), 437-438.

[51] Fonseca, F. C.; Goya, G. F.; Jardim, R. F.; Muccillo, R.; Carreno, N. L. V.; Longo, E.; Leite, E. R. Physical Review B 2002, 66, (10), 104406-104410.

[52] Medvedkin, G. A.; Ishibashi, T.; Nishi, T.; Hayata, K.; Hasegawa, Y.; Sato, K. Japanese Journal of Applied Physics Part 2-Letters 2000, 39, (10A), L949-L951.

[53] Dietl, T. Semiconductor Science and Technology 2002, 17, (4), 377-392.

[54] Ohno, H.; Matsukura, F. Solid State Communications 2001, 117, (3), 179-186.

[55] Munekata, H.; Ohno, H.; Vonmolnar, S.; Segmuller, A.; Chang, L. L.;Esaki, L. Physical Review Letters 1989, 63, (17), 1849-1852.

[56] Ohno, H.; Shen, A.; Matsukura, F.; Oiwa, A.; Endo, A.; Katsumoto, S.; Iye, Y. Applied Physics Letters 1996, 69, (3), 363-365.

[57] Dietl, T.; Ohno, H.; Matsukura, F.; Cibert, J.; Ferrand, D. Science 2000, 287, (5455), 1019-1022.

[58] Venkatesan, M.; Fitzgerald, C. B.; Lunney, J. G.; Coey, J. M. D. Physical Review Letters 2004, 93, (17), 177206 -177209.

[59] Hong, N. H.; Brize, V.; Sakai, J. Applied Physics Letters 2005, 86, (8), 082505.

[60] Theodoropoulou, N.; Hebard, A. F.; Overberg, M. E.; Abernathy, C. R.; Pearton, S. J.; Chu, S. N. G.; Wilson, R. G. Physical Review Letters 2002, 89, (10),107203 -107206.

[61] Krost, A.; Harbecke, B.; Faymonville, R.; Schlegel, H.; Fantner, E. J.; Ambrosch, K. E.; Bauer, G. Journal of Physics C-Solid State Physics 1985, 18, (10), 2119-2143.

[62] Gorska, M.; Anderson, J. R.; Kido, G.; Golacki, Z. Solid State Communications 1990, 75, (4), 363-367.

[63] Krenn, H.; Herbst, W.; Pascher, H.; Ueta, Y.; Springholz, G.; Bauer, G. Physical Review B 1999, 60, (11), 8117-8128.

[64] Bartholomew, D. U.; Furdyna, J. K.; Ramdas, A. K. Physical Review B 1986, 34, (10), 6943-6950.

[65] Busch, G.; Guntherodt, G.; Wachter, P. Journal de physique 1971, 32, 928-929.

[66] Busch, G.; Junod, P.; Watcher, P. Physics letters 1964, 12, (1), 11-12.

[67] Kaltsoyannis, N.; Scott, P., The f elements. In Oxford University Press: 1999.

[68] Wachter, P., Europium Chalcogenides:EuO,EuS,EuSe and EuTe. In North-Holland :Amsterdam: 1979; Vol. 2.

[69] Redígolo, M. L.; Koktysh, D. S.; Rosenthal, S. J.; Dickerson, J. H. Physica Status Solidi (c) 2007, 4, No. 2, p.406.

[70] Mirkovic, T.; Hines, M. A.; Nair, P. S.; Scholes, G. D. Chemistry of Materials 2005, 17, (13), 3451-3456.

[71] Hasegawa, Y.; Afzaal, M.; O'Brien, P.; Wada, Y.; Yanagida, S. Chemical Communications 2005, (2), 242-243.

[72] Thongchant, S.; Hasegawa, Y.; Wada, Y.; Yanagida, S. Chemistry Letters 2001, 1274-1275.

[73] Hasegawa, Y.; Adachi, T. A.; Tanaka, A.; Afzaal, M.; O'Brien, P.; Doi, T.; Hinatsu, Y.; Fujita, K.; Tanaka, K.; Kawai, T. Journal of the American Chemical Society 2008, 130, (17), 5710-5715.

[74] He, W.; Somarajan, S.; koktysh, D.; Dickerson, J. H. Nanoscale 2010.

[75] Hasegawa, Y.; Okada, Y.; Kataoka, T.; Sakata, T.; Mori, H.; Wada, Y. Journal of Physical Chemistry B 2006, 110, (18), 9008-9011.

[76] Malik, M.; O'Brien, P.; Revaprasadu, Y. N. Phosphorus,Sulfur and Silicon and the Related Elements 2005, 180, 689-712.

[77] Chen, L. Y.; Xing, H.; Shen, Y. M.; Bai, J. F.; Jiang, G. Q. Journal of Solid State Chemistry 2009, 182, (6), 1387-1395.

[78] Somarajan, S.; Hasan, S. A.; Harrison, M. A.; Mahajan, S. V.; Adkins, C. T.; Harth, E.; Dickerson, J. H. Key Engineering Materials 2009, 412, 113-118.

[79] Koktysh, D. S.; Somarajan, S.; He, W.; Harrison, M. A.; McGill, S. A.; Dickerson, J. H. Nanotechnology 2010, 21, (41), 415601.

[80] Lee, S. M.; Cho, S. N.; Cheon. Journal of Advanced Materials 2003, 15, 441.

[81] Dimmock, J. O. Ibm Journal of Research and Development 1970, 14, (3), 301-308.

[82] Xavier, R. M. Physics Letters A 1967, A 25, (3), 244.

[83] Wachter, P. Physik der Kondensierten Materie 1968, 8, (1), 80-86.

[84] Huxter, V. M.; Mirkovic, T.; Nair, P. S.; Scholes, G. D. Advanced Materials 2008, 20, (12), 2439-2443.

[85] Chen, Q.; Zhang, Z. J. Applied Physics Letters 1998, 73, (21), 3156-3158.

[86] Jacob, J.; Khadar, M. A. Journal of Magnetism and Magnetic Materials 2010, 322, (6), 614-621.

[87] Li, X. H.; Xu, C. L.; Han, X. H.; Qiao, L.; Wang, T.; Li, F. S. Nanoscale Research Letters 2010, 5, (6), 1039-1044.

[88] Nath, B. K.; Chakrabarti, P. K.; Das, S.; Kumar, U.; Mukhopadhyay, P. K.; Das, D. Journal of surface science technology 2005, 21, 169-182.

[89] Ehnholm, G. J.; Katila, T. E.; Lounasmaa, O. V.; Reivari, P.; Kalvius, G. M.; Shenoy, G. K. Zeitschrift für Physik 1970, 235, (4), 289-307.

[90] Song, O.; Zhang, Z. J. Journal of the American Chemical Society 2004, 126, (19), 6164-6168.

[91] Iglesias, O.; Labarta, A. Physica B-Condensed Matter 2004, 343, (1-4), 286-292.

[92] Alivisatos, A. P. Science 1996, 271, (5251), 933-937.

[93] Mahajan, S. V.; Dickerson, J. H. Nanotechnology 2007, 18, 325605.

[94] Ivanov, R. A.; Korsakov, I. E.; Formanovskii, A. A.; Paramonov, S. E.; Kuz'mina, N. P.; Kaul, A. R. Russian Journal of Coordination Chemistry 2002, 28, (9), 670-672.

[95] Trindade, T.; O'Brien, P.; Pickett, N. L. Chemistry of Materials 2001, 13, (11), 3843-3858.

[96] Brus, L. E. Journal of Chemical Physics 1984, 80, (9), 4403-4409.

[97] Cardona, P. Y., In Fundamentals of Semiconductors, Springer: 1996.

[98] Brus, L. E. Journal of Chemical Physics 1983, 79, (11), 5566-5571.

[99] Goncharenko, I. N.; Mirebeau, I. Physical Review Letters 1998, 80, (5),1082-1085.

[100] terHaar, E.; Bindilatti, V.; Oliveira, N. F.; McCabe, G. H.; Shapira, Y.; Golacki, Z.; Charar, S.; Averous, M.; McNiff, E. J. Physical Review B 1997, 56, (14), 8912-8918.

[101] Gorska, M.; Anderson, J. R.; Peng, J. L.; Oka, Y.; Jen, J. Y.; Mogi, I.; Ravot, D.; Golacki, Z. Physical Review B 1997, 55, (7), 4400-4404.

[102] Braunstein, G.; Dresselhaus, G.; Heremans, J.; Partin, D. Physical Review B 1987, 35, (4), 1969-1972.

[103] Erwin, S. C.; Zu, L. J.; Haftel, M. I.; Efros, A. L.; Kennedy, T. A.; Norris, D. J. Nature 2005, 436, (7047), 91-94.

[104] Biswas, K.; Sardar, K.; Rao, C. N. R. Applied Physics Letters 2006, 89, 132503.

[105] Gorska, M.; Anderson, J. R. Physical Review B 1988, 38, (13), 9120-9126.

[106] Shotov, A. P.; Selivanov, Y. G. Jetp Letters 1987, 45, (1), 3-7.

[107] Zhao, F.; Gao, S. Journal of Materials Chemistry 2008, 18, (9), 949-953.

[108] Pan, D.; An, L.; Sun, Z.; Hou, W.; Yang, Y.; Yang, Z.; Lu, Y.Journal of American Chemical Society 2008, 130, 5620-5621.

[109] Zubkowski, J. D.; Hall, T.; Valente, E. J.; Perry, D. L.; Feliu, L. A.;Garmon, J. Journal of Chemical Crystallography 1997, 27, (4), 251-255.

[110] Shen, W. Z.; Wu, H. Z.; Mccann, P. J. Journal of Applied Physics 2002, 91, (6), 3621-3625.

[111] Mikhail, H.; Mekkawy, I. Czechoslovak Journal of Physics 1978, 28, (2), 216-219.

[112] Dietl, T.; Awschalom, D. D.; Kaminska, M.; Ohno, H., Semiconductors and Semimetals. In Elsevier Inc.: 2008; Vol. 82.

[113] Chen, C. J.; Ma, Y.; Li, Y.; Wang, X. Z.; Borghesi, A.; Guizzetti, G.; Sassella, A.; Viticoli, S. Journal of Applied Physics 1993, 73, (10), 5736-5738.

[114] Gaj, J. A.; Planel, R.; Fishman, G. Solid State Communications 1979, 29, (5), 435-438.

[115] Anderson, J. R.; Kido, G.; Nishina, Y.; Gorska, M. Semiconductor Science Technology 1990, 5, 134-137.

[116] Dyakonov, M., Spin Physics in Semiconductors. In Springer: 2008.

[117] Anderson, J. R.; Kido, G.; Nishina, Y.; Gorska, M.; Kowalczyk, L.;Golacki, Z. Physical Review B 1990, 41, (2), 1014-1018.

[118] Furdyna, J. K. Journal of Applied Physics 1982, 53, (11), 7637-7643.

[119] Spalek, J.; Lewicki, A.; Tarnawski, Z.; Furdyna, J. K.; Galazka, R. R.; Obuszko, Z. Physical Review B 1986, 33, (5), 3407-3418.

[120] Bastard, G.; Lewiner, C. Journal of Physics C-Solid State Physics 1980,13, (8), 1469-1479.